UNIVERSITY OF OKLAHOMA

GRADUATE COLLEGE

EXPERIMENTAL INVESTIGATION OF PROPPED FRACTURE CONDUCTIVITY

A THESIS

SUBMITTED TO THE GRADUATE FACULTY

in partial fulfillment of the requirements for the

Degree of

MASTER OF SCIENCE

By

ABHINAV MITTAL
Norman, Oklahoma
2018

EXPERIMENTAL INVESTIGATION OF PROPPED FRACTURE CONDUCTIVITY

A THESIS APPROVED FOR THE
MEWBOURNE SCHOOL OF PETROLEUM AND GEOLOGICAL ENGINEERING

BY

_____
Dr. Chandra Rai, Chair

_____
Dr. Carl Sondergeld

_____
Dr. Deepak Devegowda

Acknowledgements

I would like to thank my family for supporting and believing in me throughout the pursuit of my education at OU.

I would like to express my gratitude for my advisors, Dr. Chandra Rai and Dr. Carl Sondergeld. Thank you for giving me the opportunity to learn under your guidance, and for your valuable suggestions towards my research direction. I am thankful to Dr. Richard Larese for his insightful suggestions and help with SEM. I would also like to thank the members of the Unconventional Shale Consortium for their support. I am thankful to Dr. Deepak Devegowda for his valuable suggestions.

I am grateful to Gary Stowe and Bruce Spears, for ensuring successful completion of my research. I would like to thank all the IC^3 colleagues for their assistance, brainstorming sessions, and making the lab an enjoyable workplace.

Table of Contents

List of Figures

Abstract

Hydraulic fractures act as conduits connecting a wellbore to nanodarcy permeability unconventional reservoirs. Proppants are responsible for enhancing the fracture conductivity and help in maintaining high production rates. Laboratory testing of proppants can help in the systematic evaluation of different factors that can affect proppant performance. Field studies fail to control variables to allow evaluation of proppant performance. This study is focused on the measurement of long-term conductivity of proppant-packs at simulated reservoir temperature and pressure conditions. Various conductivity impairment mechanisms such as proppant crushing, fines migration, embedment, and diagenesis are investigated.

Testing was done using a conductivity cell, which allows simultaneous measurement of fracture compaction and permeability. The proppant-pack performance during compression between metal and shale platens was compared. The proppant filled fracture (concentration: 0.75-3 lb/ft^2) is subjected to axial load (5000 psi) to simulate closure stress. Brine (3% NaCl + 0.5% KCl) is flowed through the pack at a constant rate (3 ml/min) at 250°F over an extended duration of time (10-60 days). In this study, Ottawa sand proppant was used between platen faces fabricated from Vaca Muerta and Eagle Ford shales.

In this study, effect of proppant size, time, rock mineralogy, fluid chemistry on proppant performance is evaluated. An attempt is made to decipher the contribution of different damage mechanisms in affecting proppant performance.

Testing between metal platens indicated the reduction in permeability with 20/40 mesh Ottawa sand (~30% over 12 days) was less than that of 60/100 mesh Ottawa sand which suffered a 99% reduction in only 4 days.

Measurements with 20/40 mesh Ottawa sand between shale platens were conducted at 1.5 lb/ft^2. Over a duration of 10 days, the Eagle Ford platens proppant-pack exhibits a greater reduction in permeability, in comparison to Vaca Muerta platens. The normalized compaction for Eagle Ford shale platens is 20% more than Vaca Muerta platens, owing to greater proppant embedment. Particle size analysis and SEM images verify proppant crushing, fines migration and embedment as dominant damage mechanisms. These factors are observed to be dependent on the shale being tested. The results suggest a substantial degradation of permeability during the initial 5 days of testing, after which the permeability appears to stabilize. Crushed proppant and dislodged shale surface particles contribute to the fines generated; a greater concentration of fines is observed downstream.

Fracturing jobs involve maintaining a basic pH environment for optimal performance of fluid additives for better proppant placement via control on viscosity. Second study was conducted to compare performance on similar Eagle Ford shale by altering the fluid chemistry (pH: 10.5) to understand the impact on permeability and compaction over time.

Over a duration of 20 days, the permeability dropped from 120 darcy to 200 md. After 8 days, the pH: 10 brine permeability was 10 times lower than pH: 7 brine permeability. After 18 days, the fracture width reduced by 90%, indicating a creep behavior. High silica content (>20 ppm) was observed in the outlet brine. The proppant and rock surface were studied under SEM to investigate the role of secondary mineral growth in the drastic reduction of permeability.

Chapter 1: Introduction

1.1. Synopsis

This thesis is divided into four chapters. Chapter 1 provides a background of hydraulic fracturing in unconventional shale reservoirs, mechanisms affecting proppant conductivity, developments in proppant testing, and objectives of this research. Chapter 2 discusses the experimental setup, procedure, and calibration. Chapter 3 provides a discussion and summarizes the results. Chapter 4 presents the conclusions and findings from this study.

1.2. Unconventional shale reservoirs

A conventional petroleum system typically consists of source rock, reservoir rock, and seal. Ideal conditions of pressure, temperature and time are imperative for the cycle of oil generation, migration and accumulation. Limited access to economic production of oil and gas from conventional reservoirs and the increasing demand for energy has paved the way for efforts to extract energy from unconventional reservoirs like coal bed methane, gas hydrates, and organic rich shale.

Organic shale is a clastic sedimentary rock that possesses very fine grain rock texture (grain size varying <4 μm), exhibits hydrocarbon storage and flow characteristics attributed to nano-scale pore throat and pore size distribution (Friedman 2003; Sondergeld et al., 2010). Traditionally, shales were considered as seals for conventional reservoirs, due to their characteristic low porosity and nanodarcy range permeability. Growing energy demands necessitated the foray into unconventional shale reservoirs,

which act as combination of source, reservoir, and seal. **Fig. 1** depicts the components of shale rock showing the co-existence of different fluids and pore systems (Dang et al., 2017). The inorganic pores can be oil or water-wet, while organic pores are generally assumed oil-wet. The presence of clay and organics add complexity to the geological and petrophysical heterogeneity. The maturation of the organic part of the matrix leads to generation of hydrocarbons. The presence of clay and organics result in complex gas storage mechanisms, mechanical properties and transportability.

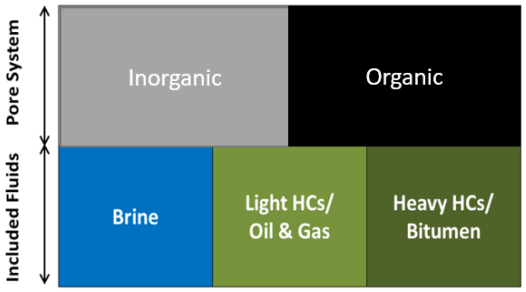

Fig. 1: Bifurcation of shale rock matrix comprising of different fluids and pore systems. Inorganic pores can be oil or water-wet, while organic pores are generally assumed oil-wet (Dang et al., 2018).

The developments in the shale gas and tight oil sector have helped establish unconventional resource plays as a major contributor to U.S. energy demands (see **Fig. 2**) (EIA, 2017). According to Annual Energy Outlook (EIA, 2018), oil and natural gas are seen as the primary fuels in energy consumption (**Fig. 3**). In the run-up to 2035, US shale is expected to contribute more than 40% to the gas supply growth (BP Energy Outlook, 2017).

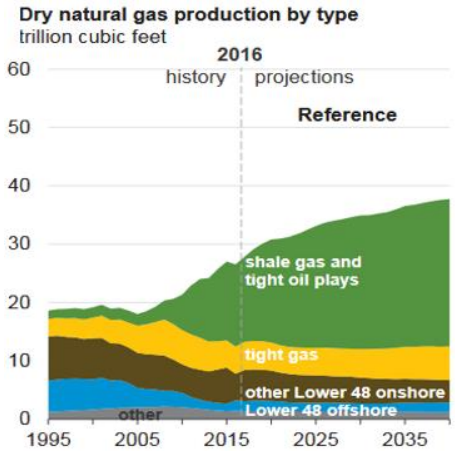

Fig. 2: Contribution of production from shale gas and tight oil plays in the U.S. energy industry (EIA, 2017).

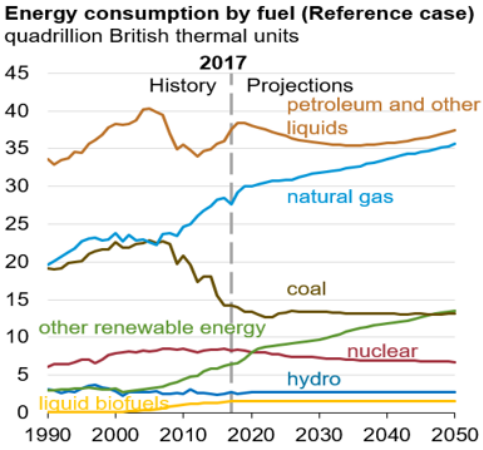

Fig. 3: Oil and natural gas are projected to be the primary fuel for energy consumption while the renewables continue to develop (EIA, 2018).

1.3. Role of hydraulic fracturing

Hydraulic fracturing is a stimulation operation where a mixture of fluid and proppant is pumped into the formation, in order to fail the rock, initiating a fracture and extending it to create a conduit connecting the wellbore to the reservoir. The fluid is pumped in stages, starting with pad stage that generally does not contain any propping agent. Fluids in each stage can be different, while proppant size can vary from stage to stage. The energy from

the fracturing fluid is used to break the rock to create fracture, and the subsequent schedule of slurry helps advance the front of fracture. It is hoped that as the fracturing fluid diffuses into the formation, the proppant will keep the fracture propped open. This sequence is followed by flowback operation, wherein an attempt is made to retrieve the injected complex chemicals. Only a fraction of the injected fluid is recovered during flowback, while small concentrations of injected chemicals can be tracked over few weeks of hydrocarbon production.

The first hydraulic fracturing operation was conducted in Houghton gas field in West Kansas in 1947. This unpropped frac operation was conducted using gasoline based frac fluid, and napalm as viscosifying agent (Howard and Fast, 1970; Clark, 1949). A need for laboratory measurements was warranted to better understand the fracturing process, to estimate hydraulically fractured network and to optimize the variables. Warpinski (2004) discussed that for shale reservoirs, the microseismic cloud is representative of the actual fracture network due to the diffusivity related limited movement of pore pressure away from the fracture planes.

Organic richness displays a vertical variability (Bohacs, 1998; Bohacs et al., 2005) due to shale depositional system, sometimes over scales less than one meter. The advent of hydraulic fracturing and horizontal drilling have increased the stimulated reservoir volume (SRV), facilitating economic production of hydrocarbons from organic rich shales. Mayerhofer et al. (2010) have shown that larger SRVs, due to longer laterals and higher injected fluid volumes, have resulted in higher cumulative six-month production

of hydrocarbons. However, large stimulation operations involving huge amounts of proppant, fracturing fluid, surface equipment have resulted in increased drilling and completion costs. Also, shale plays differ vastly from each other; some shales have multiple producible layers that need to be stimulated at different depths within the same play. Also, factors like the presence of natural fractures, ash beds (which can act as fracturing barriers), differences in matrix quality, and compatibility of formation with fracturing fluid can be critical for optimization of variables like proppant size and type; fracturing fluid; well spacing; cluster and stage spacing. Considering the volumes of raw materials used in the stimulation technique, these can have huge economic implications on the overall cost of project, if not optimized.

1.4. Proppant characterization

Hydraulic fracturing creates the SRV, which is critical to hydrocarbon production. Proppant, if placed as designed, is instrumental in keeping the fracture propped open. **Fig. 4** shows hierarchy of major proppant types available. Transitioning from the bottom to the top, the proppant types (right) are arranged in the increasing order of proppant strength, conductivity, and cost. Ceramic proppants are expensive, but provide high conductivity. Ceramics find more application in tail-ins near the wellbore, as well as in deeper and high temperature formations. In contrast, sand is the cheapest option and finds major applications in low cost projects.

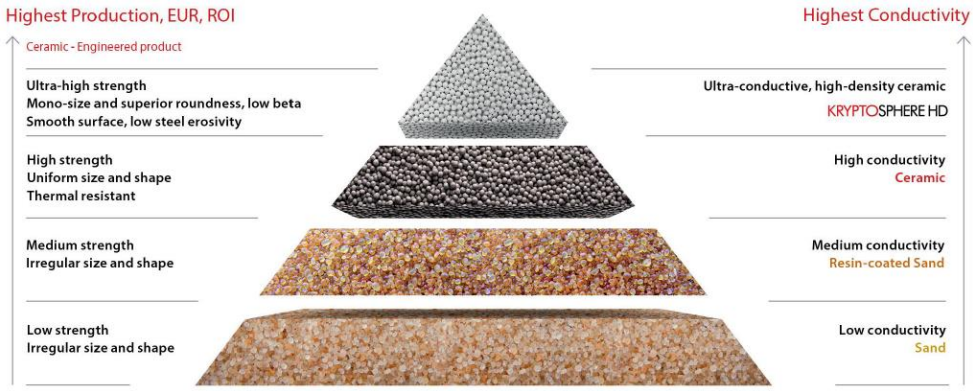

Fig. 4: Proppant hierarchy (Chapman, 2017)

Fig. 5a illustrates the sand consumption across various shale plays, as of first quarter of 2014 (Pacwest, 2014). Eagle Ford, Appalachia (including Marcellus and Utica), Permian and Bakken combined used 75% of the frac sand across North America. For most of the shale plays, frac sand occupied 90% of the share of total proppants used. Operators have been able to limit costs by introducing longer laterals, multi-pad drilling, higher intensity fracturing and reducing the use of premium proppants. **Fig. 5b** shows changing trends of using larger amounts of proppant, fluid and frac stages to drive up production performance over the years (EIA, 2016b).

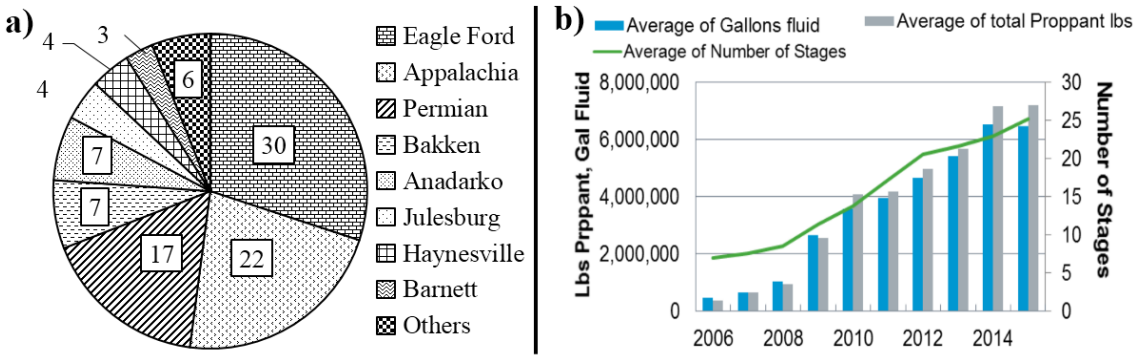

Fig. 5: a) Frac sand consumption by play (Pacwest, 2014); b) Trends in the use of proppant and water, and number of stages from 2006 to 2015. (EIA, 2016)

The demand for proppant has increased considerably; **Fig. 6** shows the worldwide use of proppant (Palisch, 2016). More than 90% of worldwide proppant was used in operations in North America. The successful implementation of horizontal drilling and hydraulic fracturing enabled overcoming extremely low matrix permeability and allowed production directly from organic rich source rocks. From 2004 – 2009, development of Barnett shale play led to gradual increase in amount of proppant used per rig. Similar completion strategies were applied to other shale plays. Rapid increase in proppant use per rig is observed from 2010 – 2012, as seen in **Fig. 6**. However, 2012 onwards, the proppant use per rig increased exponentially, demonstrating that frac operations involving increased use of proppant were adopted. A completions design in 2013-2014 involved 1000 lbs/ft proppant, 30 bbls/ft fluid, 60 ft cluster spacing, 240 ft stage spacing, and 5000 ft average lateral length. Over the years, technological advancements have increased proppant concentration to 5000 lb/ft; 50 bbls/ft fluid; tighter 15 ft. cluster spacing; 100 ft. stage spacing; and 10,000 ft average lateral length. This can potentially increase the stimulation cost from $0.5 MM to more than $1 MM per well as compared to initial frac designs (Pioneer Investor Presentation-November, 2017).

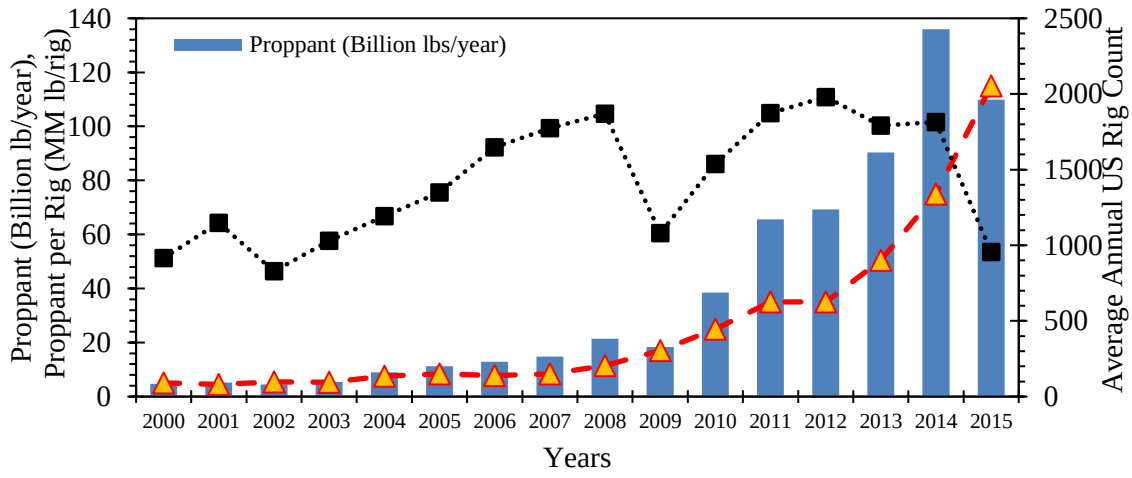

Fig. 6: Worldwide proppant use (Palisch, 2016). Proppant (billion lb/year) (blue bars) and proppant per rig (MMlb/rig) (orange-triangles) have been plotted on the primary Y-axis. Average annual US rig count (black-squares) is plotted on the secondary Y-axis.

1.5. Use of fine mesh sand

An operator uses the same proppant type, volumes and fluid chemistry concentrations, typically what has been used in the past, or in nearby wells. As a general practice, smaller mesh sand is used in the pad fluid tailed by larger sized proppant closer to the wellbore. Through such a strategy, it is hoped that finer, 100 mesh, proppant can prop open hairline and microfractures, and can be placed farther into the main fracture. On the other hand, tailing in with larger sized proppant keeps the larger fractures open (Thompson, 1977). It is thought that if the larger proppant is pumped first, bridging might limit or prevent contributions from microfractures, and can also possibly lead to screen-outs. However, in an attempt to limit the drilling and completions expense, a surge in the demand of cheaper smaller sized proppant has been observed (Epmag, 2014; PLG Consulting, 2014).

Attempts have been made to study the effect of completion parameters on well performance and expected ultimate recovery through statistical and reservoir modeling (Bandis et al., 1983; Sinha et al., 2016; Sinha et al., 2017).

Interestingly, increasing use of even smaller proppants, called microproppants, has been implemented. Microproppants, composed of quartz grains, have been characterized as particles with broad size range, where the mean diameter is 300 mesh (or 50μm). Calvin et al. (2017) have conducted field trials of these finer proppants in the pad fluid. They discussed that for Woodford shale, an uplift of 10% in gas production and 25% in condensate production was observed. Dahl et al. (2015) conducted an 11-well field trial in Barnett shale, where microproppants were added at a concentration of 0.1 lbm/gal in the pad fluid. They reported normalized production increase of 30-40% in gas and 44-53% in condensate over 210 days. It must be noted that production normalization can be complex due to nature of variables like lateral length, amount of proppant and fluid pumped, production history of the well, and toe-up or toe down well trajectory. Some of these variables cannot take proppant placement into account. These variables can possibly affect production at different scales, and are difficult to quantify, resulting in a skewed analysis of production results. The absolute impact of such proppants can be difficult to evaluate in field trial due to cost and time constraints. A well-planned experimental study can help answer some of these questions by limiting and precisely controlling the number of variables.

1.6. Fracture Conductivity

Fracture conductivity is a critical input parameter for frac modeling. Dimensionless fracture conductivity (F_{CD}) is the ratio of fracture conductivity or deliverability to reservoir deliverability:

$$F_{CD} = \frac{Fracture\ Deliverability}{Reservoir\ Deliverability} = \frac{k_{fracture} * w_{fracture}}{k_{matrix} * x_{fracture}}$$

Where,

$k_{fracture}$: fracture permeability, md

k_{matrix} : rock matrix permeability, md

$w_{fracture}$: fracture width, ft

$x_{fracture}$: fracture half-length, ft

1.7. Mechanisms affecting propped-fracture conductivity

Extensive laboratory testing have been conducted to understand the type and extent of damage mechanisms affecting the performance of proppants, placed in the fractures. Based on types of testing (short-term and long-term), damage to proppants, formation, and flow properties are assessed. **Fig. 7** broadly summarizes some of the critical damage mechanisms active in different phases of proppant testing due to mechanical and chemical degradation.

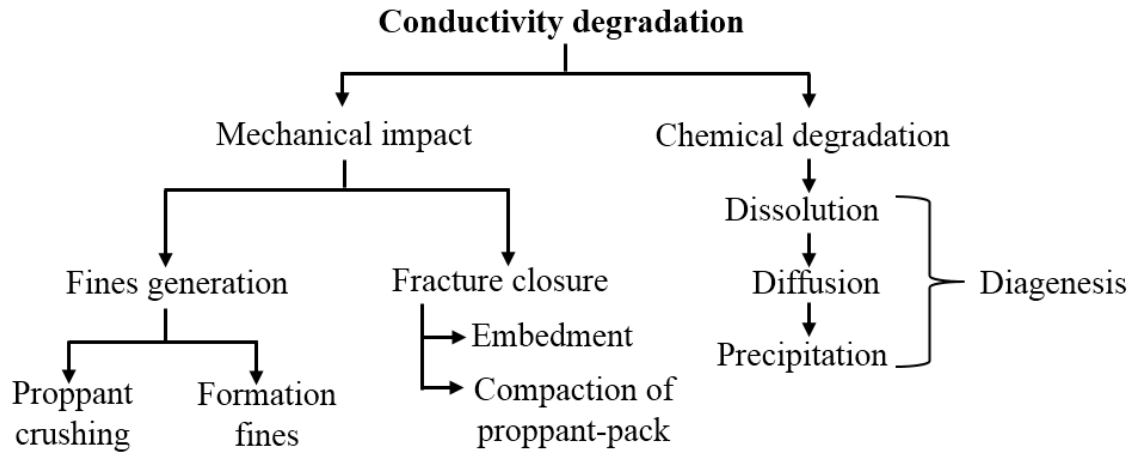

Fig. 7: Mechanical and chemical degradation of proppant conductivity (modified from Duenckel et al., 2011)

Fig. 8 is a schematic representation of the grains in a proppant pack (modified from Yasuhara et al., 2003). **Fig. 8a** (top) shows grains of proppant, and interaction between two grains. As the stress is increased, the grains undergo a tighter packing, and point contacts are established between grains, forming high stress concentration (**Fig. 8b**). Over the short term, this mechanical impact can lead to generation of fines, both from crushing of proppant, as well as due to impact of proppant and fracturing (or spalling) on formation material (**Fig. 8c**).

In the long term, based on the chemical potential difference in the system due to presence of formation material, proppant, and brine, the mechanism of pressure solution and precipitation (diagenesis) can lead to degradation of the proppant-pack system (**Fig. 8d**).

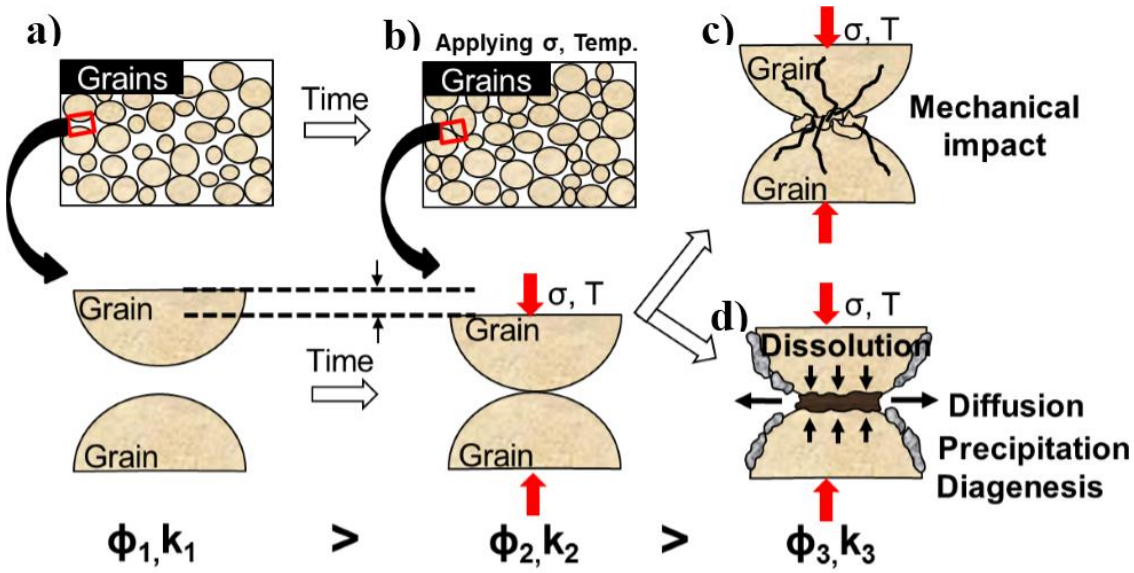

Fig. 8: Schematic of mechanisms affecting proppant conductivity (modified from Yasuhara et al., 2003)

1.7.1. Fines generation and migration

Fines can be generated either by failure of proppants or from impact of proppant on the rock platen. The API standards for crush tests determines the stress at which proppants fail. However, these are dry crush tests conducted at room temperature, and between sandstone platens, which are not a true representation of the sub-surface environment. Palisch et al. (2010) have discussed that different proppants fail differently at different closure stresses, thereby affecting proppant performance i.e. sands shatter like glass, while ceramics cleave along the failure plane. Kassis and Sondergeld (2010) conducted measurements for propped-fracture permeability as function of confining stress on Barnett shale samples. SEM images of the proppant-pack system after the experiment verify the differences in proppant failure.

Cutler et al. (1985) have stated that crush tests according to API standards should not be used solely to assess the conductivity of proppants. Schubarth and Milton-Tayler (2004) have discussed that crush percentage gives part of the picture. The dimensions and proportion of crushed proppant can possibly affect conductivity for different varieties of proppants. Fines generated, from proppant crushing and formation, can migrate in the direction of flow, plugging up the pore system between proppant grains leading to rapid reduction in permeability. Gidley et al. (1995) demonstrated that for testing of 20/40 sand, particles finer than 100 mesh were mobilized, affecting the proppant-pack permeability considerably.

Ghosh et al. (2014) performed long-term measurements at reservoir temperature between shale platens. The experimental results confirmed the intuitive understanding that sand crushed to form smaller particles than ceramic proppants. These mechanical changes were observed to be the reason for over 90% decrease in permeability in ten days of testing.

1.7.2. Propped fracture closure

The closure of propped fractures can be attributed to: 1) embedment, and 2) compaction of proppant-pack. The conductivity tests in accordance with API standards do not take into account the changing fracture width due to compaction of the proppant-pack. The limited understanding makes it difficult to accommodate closure of fracture as an independent variable in simulation studies.

Walsh (1981) developed a model describing the pressure dependence of permeability between two rough surfaces. This model takes the roughness into account using root-mean-square (RMS) asperity height (Walsh, 1981). Kassis and Sondergeld (2010) showed that monolayer propped fracture permeability agreed with the Walsh model (1981) at medium pressure ranges (approximately 1300 to 3500 psi). The disagreement at high-pressure regime was attributed to proppant embedment, confirmed through SEM imaging.

The impact of closure stress and the presence of soft components like organics and clays in shale leads to enhanced embedment of proppant. The extent of embedment is a composite effect of rock mineralogy (or strength), proppant characteristics (shape, size, and strength), temperature, and fluid. Alramahi and Sundberg (2012) conducted short-term embedment tests, and developed an analytical model relating fracture conductivity loss to embedment. However, this does not take the effect of fines migration, creep, and temperature into account. Also, clays can be sensitive to different fracturing fluids, adding more complexity.

1.7.3. Diagenesis

In geological context, diagenesis is defined as “chemical, physical, or biological changes that a sediment undergoes after initial deposition, and during and after lithification,” excluding weathering and metamorphism. These changes can occur at relatively low temperature and pressure; resulting into changes in rock’s texture and mineralogy (Duenckel et al., 2011). There have been evidences that such reactions can occur at propped-fracture interface leading to crystalline precipitation and possibly associated loss of fracture conductivity. The extent and impact of diagenetic growth on production of hydrocarbons over the life of well remains an area of limited understanding.

1.7.3.1. Pressure solution

Yasuhara et al. (2003), through a mechanistic model backed by experimental evidence, have demonstrated that the process of dissolution, diffusion, and precipitation could be accelerated at high temperatures and pressures, also known as stress corrosion. This can potentially lead to rapid destruction of porosity over a short span of time. The model developed was simplistic because it assumed all particles are of similar size and composed of silica. However, it must be noted that in presence of a complex sub-surface environment, the kinetics of these mechanisms can be significantly influenced by the chemical potential energy differences in the system.

Observations from Heald (1956) show that under favorable conditions, the presence of clays at quartz grain boundaries can accelerate pressure solution; clays are less susceptible to pressure solution than quartz. Thomson (1959) suggested that the release

of potassium into pore fluid results into high pH zones accelerating silica dissolution, and precipitation in areas with lower pH gradient. Growth of smectite clay due to presence of volcanic glass at elevated temperatures has also been observed by Mottl and Holland (1978).

Quartz hydrolysis at ambient temperatures has been extensively studied in the past. Krauskpof (1959) demonstrated that solubility of amorphous silica can increase three-fold with an increase in temperature from 25^0C to 100^0C. Knauss and Wolery (1988) observed increase in silica release rate from quartz into the solution on exposure to high pH fluids (from pH 7 to 12). Initiation of etch pits was observed through SEM imaging. Also, high temperature made the hydrolysis mechanism increasingly pH dependent.

1.7.3.2. Proppant degradation

Apart from the various mechanism impacting proppant performance discussed earlier, Weaver et al. (2005) discussed the possibility of proppant diagenesis as a potential source of degradation. They suggested that resin coated proppant helps decrease the rate of pressure dissolution and extent of proppant embedment. Weaver and Knox (1992) observed that alumina and zirconium based proppants exhibited analcite and other porosity filling crystalline overgrowths when exposed to fluid at high temperature over time.

Weaver et al. (2007) performed static laboratory tests (no-flow) in a conductivity cell, where proppants were placed between sandstone cores in a simplistic system with 2%

KCl brine at 250^0F and 10,000 psi closure stress for 140 hours. Electron dispersive X-ray (EDX) revealed crystal growths in ceramic proppants. They observed the Si/Al ratio of such overgrowths to be between that of formation and proppant. They suggested that coating proppant with surface modifying agents (SMA) tends to prevent this growth, at least over short time spans. It is therefore imperative to evaluate the impact of such overgrowths on proppant conductivity in the long term through dynamic testing.

Weaver et al. (2008) conducted dynamic flow experiments to evaluate temperature-promoted diagenetic growth. Deionized water was passed through crushed formation material to imitate synthetic formation water. This was flowed through proppant packs containing different proppants at 550^0F. Over a duration of 7 days, crystalline growth was observed throughout sintered bauxite proppant, cementing multiple grains of proppant. Also, the authors performed single-grain mechanical crush tests. Based on an average of 30 measurements of each proppant type, 20-60% loss in crush strength of different bauxite proppants was attributed to stress corrosion and geochemical degradation after exposure to formation water at high temperature. The overgrowths were observed to be mordenite and clinoptilolite, different forms of zeolites (Duenckel et al., 2011). However, these tests were conducted at zero closure stress. It is expected that proppant degradation, both mechanical and chemical, can be drastically accelerated in high pressure and temperature conditions (Arrhenius equation) (Brown et al., 2012).

Static temperature and pressure testing was performed by LaFollette and Carman (2010) involving Haynesville shale; high pH borate cross-linked gelled water and ceramic proppant was used to imitate sub-surface conditions and evaluate diagenetic growth. For

static experiments spanning 60 days, they started to observe honeycomb structures on proppant grains. However, the elemental and mineral compositions of such overgrowths could not be identified because the thickness of precipitated overgrowths was insufficient for Energy-dispersive X-ray Spectroscopy (EDS) analysis. Water analysis showed an increase in sodium, calcium, potassium and Total Dissolved Solids (TDS) reached a peak at 60 days. Brinell hardness of shale samples exposed to fracturing fluids at elevated temperatures decreased by 60% over a span of 60 days, suggesting the possibility that proppant embedment could be a huge detrimental factor in proppant performance.

Duenckel et al. (2011) evaluated the "dissolution and reprecipitation process," and the possible conditions for such growth. As per Stim-Lab Proppant Conductivity Consortium findings (2008), most of the diagenetic growth has been associated with zeolites. Most of the transformation from volcanic glass to forms of zeolite (namely clinoptilolite, mordenite, and analcite) is expected to accelerate at high temperature and alkaline pH environment (Hawkins 1981). The continuous source of silicate over time is critical for zeolite crystallization. Duenckel et al. (2011) performed static tests at elevated temperature and pressure for a variety of proppant and formation material. They observed diagenetic growth within 15 days on all proppants when the formation material from Haynesville, Pinedale and Steamboat formations were present. Through SEM-EDS analysis, they observed these precipitates to be rich in silica. In a separate study, lower conductivity was observed when testing was performed between shale platens instead of sandstone platens. However, they did not observe any zeolite growth, and concluded that reprecipitation of dissolved formation can be difficult to simulate in flow-

through/dynamic experiments. Through field observations, they cited that most of the sub-surface environment is acidic due to presence of CO_2 and H_2S. Based on the recovered proppants, they did not see any evidence of zeolite deposition.

1.8. Motivation

A typical fracture job can take 7-10 days and can take as much as a month before flowback is initiated. In all this time, the proppant and formation are exposed to alkaline/high pH environments from the chemicals associated with the fracturing fluid. Proppant grains collected during flowback represent a small fraction of injected proppant, closer to the wellbore, but away from the direct contact with the formation. Also, any diagenetic growth would cement the proppant grains due to the reprecipitation process. This would add complexity to retrieving the grains affected by diagenetic activity, as part of flowback.

Most conventional laboratory testing involves the use of weathered sandstone cores, instead of shale platens; these are not a true representation of the sub-surface formations. Fresh surface of shales are exposed that have high potential energy and chemical affinity, during fracturing. An exposure to injected proppant and complex fracturing fluids containing combinations of biocides, friction reducers, scale inhibitors, crosslinkers, pH adjusting agents, surfactants; and can disturb the chemical equilibrium. The presence of high temperature and pressure can initiate and accelerate complex reactions at the chemically active formation face leading to drastic deterioration of proppant performance.

The role of high-ionic-strength fracturing fluids, particularly at high pH, in affecting proppant performance due to pressure solution and precipitation needs further evaluation.

Laboratory proppant testing is generally conducted under simplistic conditions. To simulate some sub-surface environments (eg. Vaca Muerta), it is worthwhile to evaluate the influence of the presence of basalt. Studies by (Lejay et al., 2017) and (Calvin et al., 2015) show bedded fractures filled ash beds across the Vaca Muerta, Niobrara and Eagle Ford formations. Based on XRD analysis, basalt consists of sodium-anorthite [$(Ca,Na)(Si,Al)_4O_8$], augite [$Ca(Fe,Mg)Si_2O_6$], and forsterite [Mg_2SiO_4]. Presence of silica and basalt, when exposed to high pH brine at elevated temperature, releases cations like sodium, potassium, magnesium and aluminum, which are conducive to the formation of clay minerals and zeolites.

1.9. Developments in proppant testing

The pioneering work in fracture conductivity measurement until 1970's involved placing proppant between metal platens. These measurements were conducted at room temperature using nitrogen, oil, or water. Cooke (1973) demonstrated that tests conducted for longer duration at constant stress for 10/20 sand in 250^0F brine exhibited continued decline in permeability over three weeks. A linear decrease in permeability with the logarithm of time was observed. Comparative experiment at room and high temperature (250°F) using glass beads showed significant reduction in porosity. Cooke observed higher breaking of glass beads when exposed to high temperature brines. Crushing and redistribution of fines in pore spaces was found to be an important factor. Cooke observed

that brine permeability was one-third oil permeability; and he performed experiments to study the non-darcy flow effects. Cooke (1973) stressed the need for long-term experiments to assess the impact of reservoir conditions on proppants.

Absence of testing standards led to disparity in fracture conductivity values reported in literature. Some of these different testing conditions were identified as: a) short testing times, b) varying proppant size distribution within same mesh range, c) testing fluid composition, d) testing with steel versus rock platens and e) temperature and fluid effects. Finally, American Petroleum Institute (API) issued "Recommended Practices for Evaluating Proppant Conductivity", in 1985. McDaniel (1986) followed these procedures to establish the impact of high closure stress and high temperature testing using brine for long durations of time. The tests involved maintaining pH in the range of 6.5-7.5 to minimize silica dissolution. The test fluid was prepared using deionized water and 2% KCl. A test at 75^0F demonstrated that as much as 40% of fracture conductivity was lost over five days of testing. The conductivity loss due to temperature increase was irreversible, i.e. conductivity could not be regained after cooling the cell. Tests also showed that closure stress increased the adverse effects of temperature and brine on proppants. An experimental study was conducted to compare conductivity loss for test fluid with and without silica pre-saturation. They observed 15% additional conductivity loss for the fluid without silica pre-saturation, as compared to silica pre-saturation test.

Apart from time, closure stress and temperature, it was critical to study the impact of embedment and fracturing fluid additives on conductivity and permeability. Penny (1987) performed short-term conductivity tests using steel platens to establish baseline

conductivity, where no embedment is expected. Higher permeability was observed between metal platens, as compared to Ohio sandstone patens. This was explained by the 'wall effect,' i.e. it is expected that the area next to metal platens will exhibit higher conductivity than the bulk proppant-pack response. However, as compared to metals, this 'wall effect' is minimized in sandstone cores due to embedment, leading to lower permeability.

Considering sandstone is stiffer (89% quartz and feldspar) as compared to organic-rich shales, the effect of embedment and fracture closure on proppant-pack permeability in shales needs to be evaluated. Organic-rich shale possess complex mineralogy dominant with reactive clays and extreme heterogeneity. Mechanisms like proppant crushing, fines generation and migration, cyclic stress, and embedment have a direct dependence on the mechanical properties of the rock and strength of proppant.

1.10. Objectives

- Evaluation of proppant performance after placement in the fracture. Long-term testing is designed to understand long-term degradation mechanisms that are masked in the outdated, but still currently practiced, 2-hour short tests (API standards).

- To conduct experiments which more closely model in-situ conditions. To achieve this requires improvements in conductivity cell design, experimental procedure, and use of shale platens instead of sandstone platens at reservoir temperature and pressure conditions spanning 10-60 days.

- To understand, quantify and isolate the contribution of mechanical and chemical degradation mechanisms such as proppant crushing, embedment, fines migration, diagenesis, and fracture closure affecting the proppant conductivity.

Chapter 2: Experimental setup and procedure

2.1. Schematic of experimental setup

The experimental setup for proppant conductivity testing is illustrated in **Fig. 9**. The solid green line represents fluid flow at elevated temperature, long-dashed blue line represents the communication between conductivity cell and differential gauge, dotted-orange line represents gas line to regulate back-pressure regulator, while the short-dashed black lines show the communication between instruments and computer. Details of each component are presented in **Appendix A**.

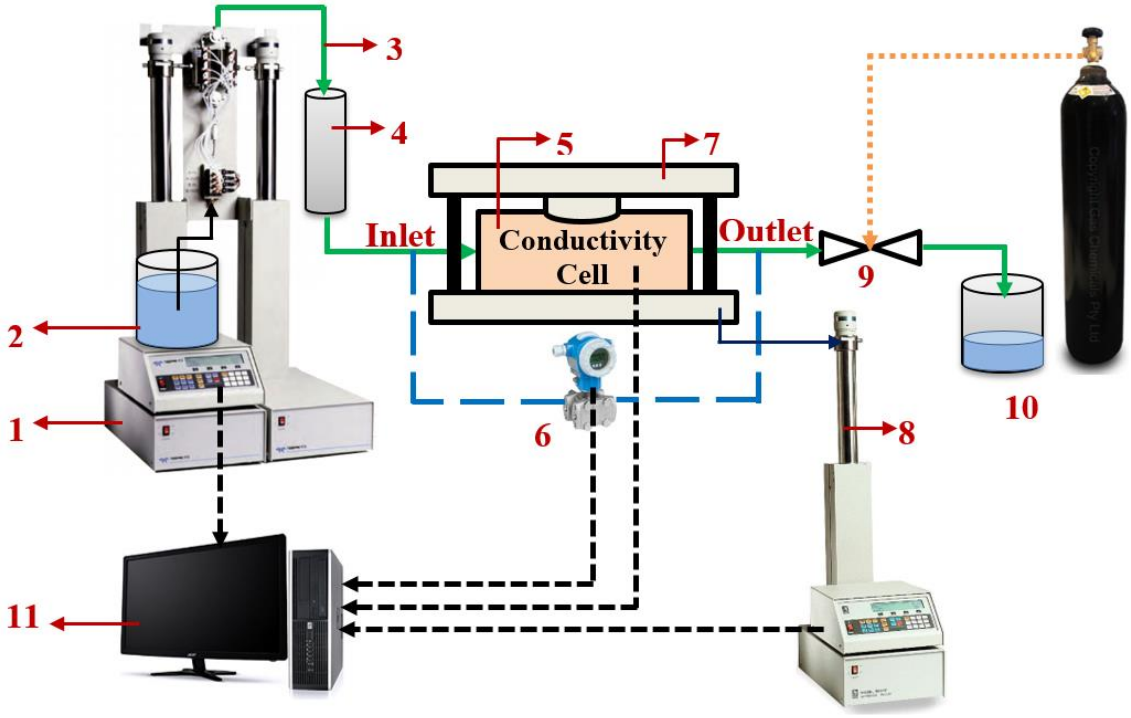

Fig. 9: Schematic of experimental setup. Two syringe pumps are connected in parallel to maintain continuous brine supply throughout the duration of the experiment. Flow is regulated using a pump controller with flow accuracy of 0.01 ml/min at a constant flow rate of 3 ml/min. The differential pressure gauge is calibrated for a range of 0-25 psi with an accuracy of ±0.01 psi. The temperature was set at 250°F throughout the duration of the experiment. A closure stress of up to 10,000 psi can be applied on the proppant-pack.

2.2. Conductivity cell

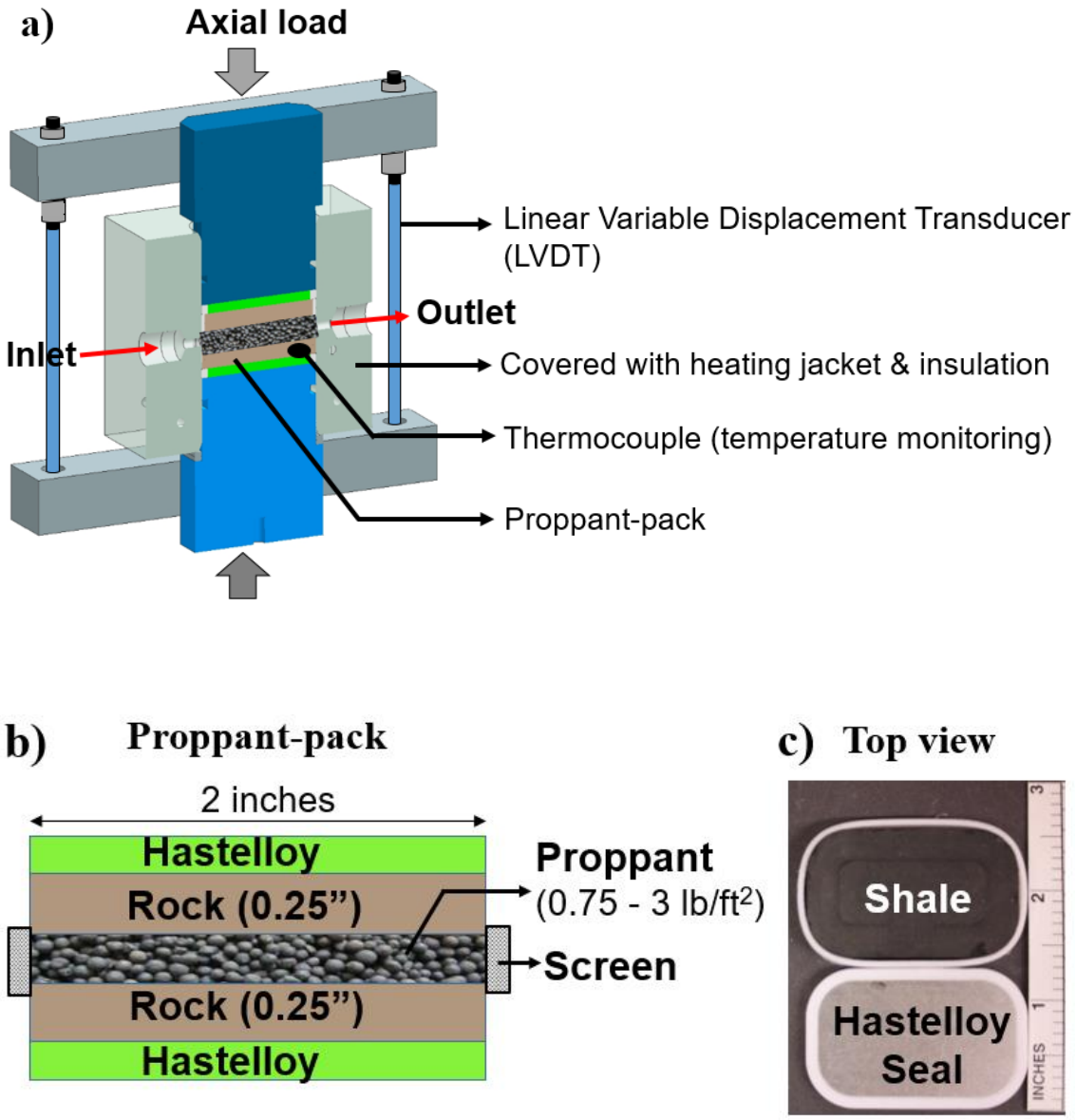

Fig. 10: Components of conductivity cell. a) Cross-section of the conductivity cell (Hastelloy C-276) consisting of upper and lower pistons, platens (steel or shale) and proppant. At mid-proppant level there are two ports to allow fluid flow through the pack. Two LVDTs are used to measure continuous changes in compaction. b) An expanded view of the platen-proppant pack assembly consisting of a sealed Hastelloy platen, rock and proppant. Hastelloy screens are placed at the inlet and outlet ports to contain the proppant. c) Top view showing the rock and Hastelloy-teflon seals.

Cross-section view of the conductivity cell is illustrated in **Fig. 10**. The proppant-pack is located at the center of conductivity cell such that brine can flow horizontally through the pack. An axial load, applied through the top and bottom pistons, simulates closure stress on the proppant-pack, as shown in **Fig. 10a**.

All components of our modified conductivity cell are made of Hastelloy C-276, a nickel-chromium-molybdenum alloy with 5% iron, which improves resistance to pitting and stress corrosion (Haynes 2016). Another critical feature of the modified conductivity cell is the ability to measure compaction. Compaction is recorded by two Linear Variable Differential Transformers (LVDTs) with a resolution of ±0.0001 inch (see vertical rods in **Fig. 10a**).

Fig. 10b illustrates the expanded cross-section of the proppant-pack assembly. The proppant-pack is 2 inches long, and consists of Hastelloy platens with Teflon seals at the top and bottom, to prevent the fluid loss. The proppant is sandwiched between the top and bottom surface platens, which are machined from the rock of interest. The cell has been designed to accommodate rock or metal platens (2" long * 1.25" wide * 0.25" thick). The proppant concentration can be varied from 0.75 – 3 lb/ft^2, giving a diverse range of expected field conditions. In addition, Hastelloy screens are used at the ends of proppant-pack to contain the proppant within the pack. **Fig. 10c** shows the top view of the seal and rock platens with a Teflon sleeve on the perimeter.

2.3. Experimental Procedure

2.3.1. Petrophysical characterization of rock

The experimental procedure for determining rock mineralogy, porosity, TOC, static Young's modulus using nanoindentation are discussed in **Appendix B**.

2.3.2. Proppant conductivity testing

2.3.2.1. Sample preparation

The rock platens measuring 2" long * 1.25" wide * 0.25" thick were machined using diamond saw (see **Fig. 10b** and **Fig. 10c**). The platens were then sequentially polished with 300, 600, 1200 and 1500 grit paper for a total duration of 30 minutes, to obtain a smooth surface. The rock platen was then scanned using profilometer to measure roughness. Also, the formation material near the platen was used for petrophysical characterization of the rock (discussed in **Appendix B**).

2.3.2.2. Brine preparation

The brine was prepared using distilled water (total dissolved solids (TDS): 1.05±0.07 ppm @ 23.8°C). The brine was composed of deionized water mixed with 3% NaCl and 0.5% KCl, by weight. This corresponds to a TDS of 33,900 ppm @ 23.9°C. For the experiments dealing with pH 10 brine, 0.05 molar sodium carbonate was added to the brine.

2.4. LVDT calibration

The linear voltage differential/displacement transformer (LVDT) was calibrated using MTS Calibrator Model 650.03 (see **Fig. 11**). The calibration was performed at room temperature. The rotation of micrometer head on the left provides a linear movement to the end of the fixture arm housing the LVDT core and shell.

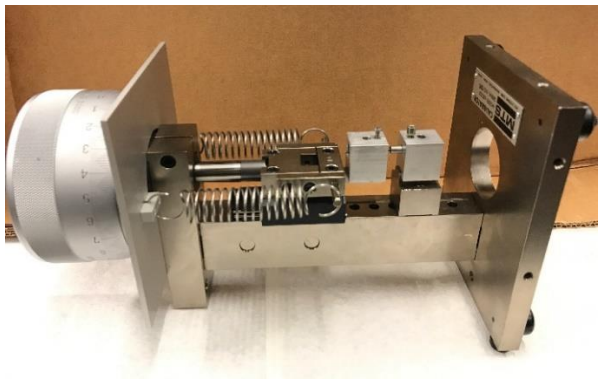

Fig. 11: MTS Calibrator Model 650.03

The LVDT element is moved from one limit to the other, in small increments, and the corresponding change in voltage response is recorded. Responses for the two LVDTs are shown in **Fig. 12**. The relationship between distance and voltage is used to measure compaction of proppant-pack.

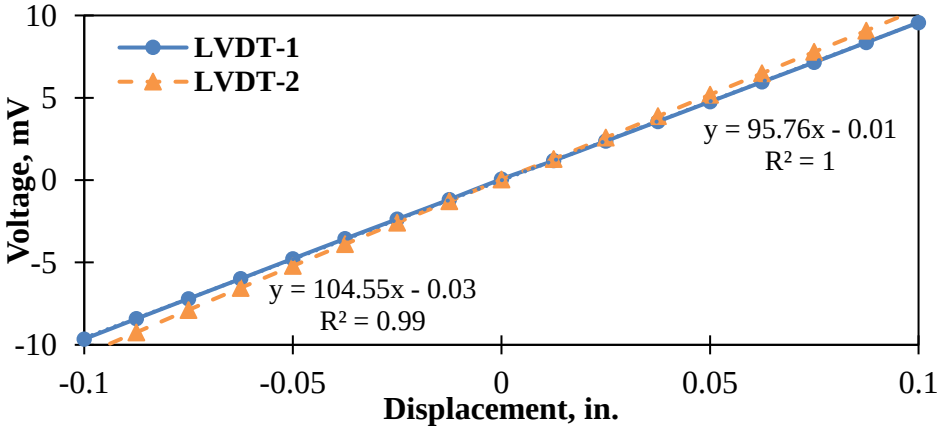

Fig. 12: LVDT calibration using MTS calibrator for 2 LVDTs. A linear trend was observed across the range of LVDTs.

2.5. Profilometer

2.5.1. Specifications

A confocal microscope was used to measure the extent of embedment of proppant on the shale surface. The Keyence confocal microscope (VK-X200) is a non-contact laser microscope that can measure the roughness and profile of any surface. A 20x lens was used to acquire the surface profile, which has a resolution of 0.5 nm, an accuracy of 0.2+ (L/100) µm, and repeatability of 40 nm in the Z-direction. The lens enables of height measurement of up to 24.5 mm. The Keyence microscope acquires data at individual spots, and stitches blocks to form a 10x10 matrix (total area: 27 mm^2 approximately). The surface of rock is scanned before and after the experiment to detect any change in roughness.

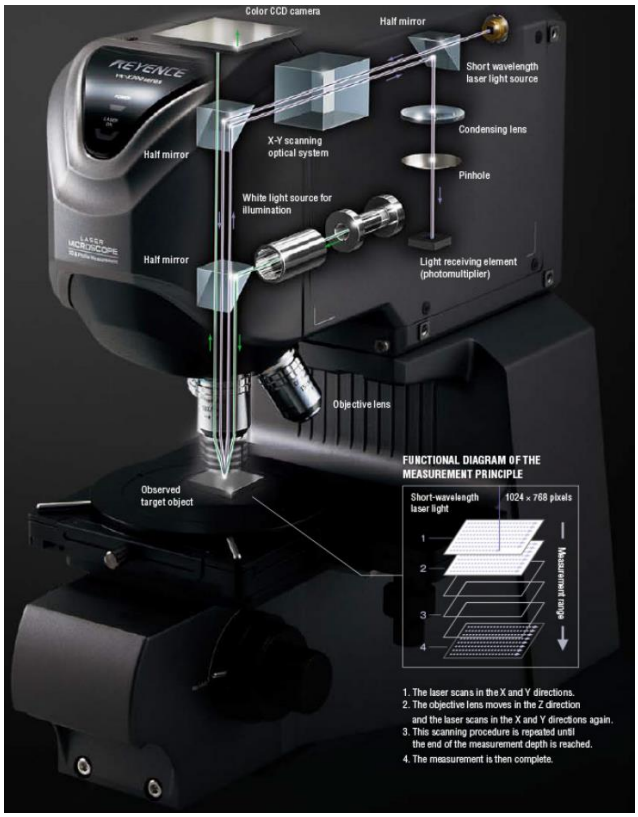

Fig. 13: Schematic of the Keyence VK-X200 confocal microscope

2.5.2. Operating principle

The Keyence optical microscope incorporates two light sources: 1) a white light for gathering color, and 2) a laser source for scanning the rock surface and acquiring height details. **Fig. 13** shows a cut-away schematic of the device. White light, in combination with a laser light source, is used to scan a surface and acquire both an optical image and high-resolution surface profile information. Nanometer-level heights can be measured by analyzing the intensity of the returned laser light relative to the z-position of the laser source. At a spot, the laser is scanned in the X, Y, and Z orientations to acquire data throughout the range of the lens (Keyence User Manual, 2014). The measurement procedure and processing details are discussed in detail in **Appendix C**.

Post completion of proppant-conductivity testing, the same rock platen scanned earlier is used. The embedded grains of proppant are carefully pulled apart using a tweezer, so that the shape and dimensions of the embedment are not altered. The broken fragments of the proppant can be cleaned by blowing air at a controlled pressure of 50 psi or less. The rock is then scanned under the confocal microscope. This measurement procedure is repeated on the post-experiment rock surface to accurately measure the embedment. The embedment depth, width, profile and surface roughness can be measured on an area of interest.

2.6. Laser Particle Size Analyzer

2.6.1. Specifications

A laser particle size analyzer (Beckman Coulter LS 13 320 with Tornado Dry Powder System) was used to characterize the particle size distribution of proppants before and after the experiment. The analyzer can resolve particles in the range of 0.4 µm - 2000 µm with a repeatability of 1% about the mean size. The particle size distribution is reported in volume percent (Beckman Coulter User Manual, 2011).

2.6.2. Measurement and calibration

The analyzer measures the signal with the laser off to subtract any noise due to ambient light. Also, background is measured without any sample, to eliminate signal due to light leakage or scattering from dust on lens or particulate presence in the optical path. For the measurement, 10-15 gram of dry proppant is loaded, and a vacuum is applied to draw the proppant into the instrument. The calibration of the analyzer was checked by scanning a standard powder sample. The particle size distribution was within the range: mean of 34.6 ± 1.5 µm.

2.7. Calibration of measurements using conductivity cell

The calibration was performed using a machined platen of Berea sandstone (22.7% porosity). **Fig. 14a** is an illustration of the sandstone platen measuring 2" long, 1.25" wide, and 0.62" high. Hastelloy platens acted as top and bottom seals. A closure stress of 2000 psi was applied on the rock through the hydraulic press. Dodecane was flowed through the sandstone at room temperature at a constant flow rate of 1 ml/min using the ISCO metering pump. The variation in differential pressure ($\Delta P = P_{inlet}-P_{outlet}$) over time, recorded at a frequency of 60 seconds is shown in **Fig. 14b**.

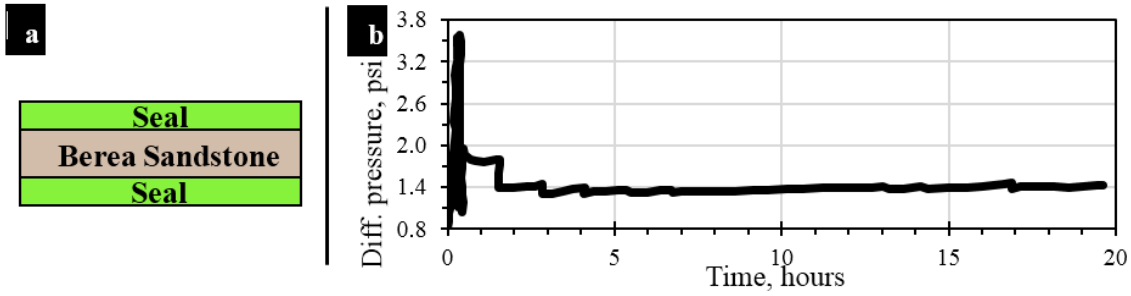

Fig. 14: a) Schematic cross-section view of proppant-pack comprised of Hastelloy seals and Berea sandstone platens. This configuration was used as a "standard" for calibration; b) Variation in differential pressure (ΔP), i.e. the difference between the inlet and outlet pressures across the Berea sandstone layer, as a function of time in hours.

The differential pressure quickly stabilized to 1.4 psi in about 2 hours, and was constant for the next 20 hours. Applying Darcy's Law, a permeability of 262 md was obtained. For the purpose of comparison, a pressure-pulse decay permeameter was used to measure permeability on a similar sandstone sample at a confining stress of 2000 psi. The Klinkenberg-corrected permeability value of 315 md was calculated. The permeability value using conductivity cell was within the 20% range of the permeability measured using pressure-pulse decay permeameter.

2.8. Experimental conditions

All experiments are carried out at 5000 psi closure stress, pore-pressure of 300 psi, at 250^0F temperature. **A proppant concentration of 1.5 lb/ft^2 is used, except where noted.** The closure stress is applied at a constant ramp-rate of approximately 100 psi/min. The brine is composed of distilled water mixed with 3% NaCl and 0.5% KCl (by weight), except where noted. The brine is flowed at a constant flow rate of 3 ml/min throughout the duration of the experiment.

Chapter 3: Results and Discussion

3.1. Proppant Characteristics

For all the experiments conducted in this study, 20/40, 40/70, and 60/100 mesh quartz proppant were used. The mean grain diameters for 20/40, 40/70 and 60/100 mesh proppants are 700 µm, 390 µm and 220 µm, respectively. The 2D surface of proppant grains was evaluated under SEM for roundness and circularity. A perfect spherical proppant grain would approach circularity and roundness value of one (Krumbein and Sloss, 1963). As illustrated in SEM images (**Fig. 15**), the 60/100 mesh proppant is angular relative to sub-rounded and circular 20/40 mesh proppant.

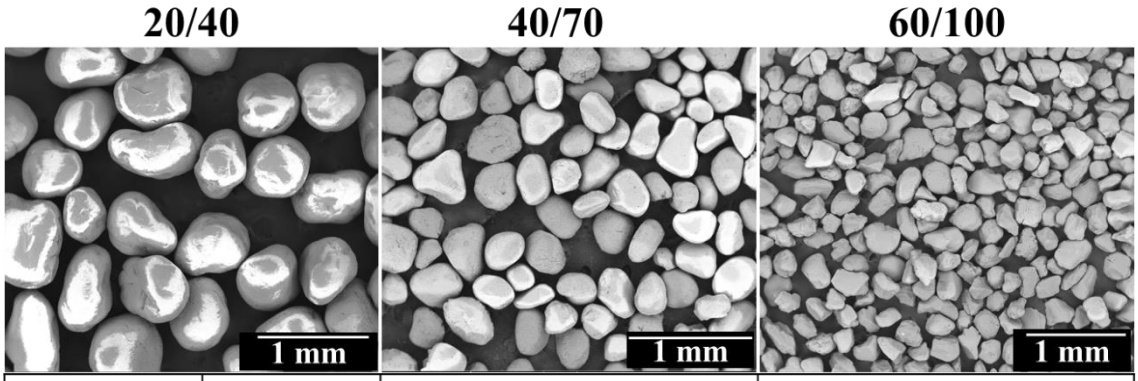

	20/40	40/70	60/100
Roundness	0.87	0.79	0.70
Circularity	0.95	0.89	0.84

Fig. 15: Secondary electron images of 20/40, 40/70 and 60/100 mesh Ottawa sand. Based on the 2-dimensional view of proppant through SEM images, roundness and circularity were calculated. Among the three sizes of proppants evaluated, 20/40 is the most rounded and circular; while 60/100 is the most angular. Calculations were performed on similar number of grains for consistency.

3.2. Repeatability Measurements

To verify repeatability, measurements were conducted using 20/40 Ottawa sand between Hastelloy metal platens. **Fig. 10b** shows a schematic of the proppant-pack used in these tests. The tests were conducted for a duration of approximately 12 days. An axial load, simulating closure stress of 5000 psi was applied on the proppant-pack. Brine was continuously flowed at a constant flow rate of 3 ml/min. The temperature of the proppant-pack system was maintained at 250ºF throughout the experiment. The permeability and compaction changes for the two experiments are illustrated in **Fig. 16**.

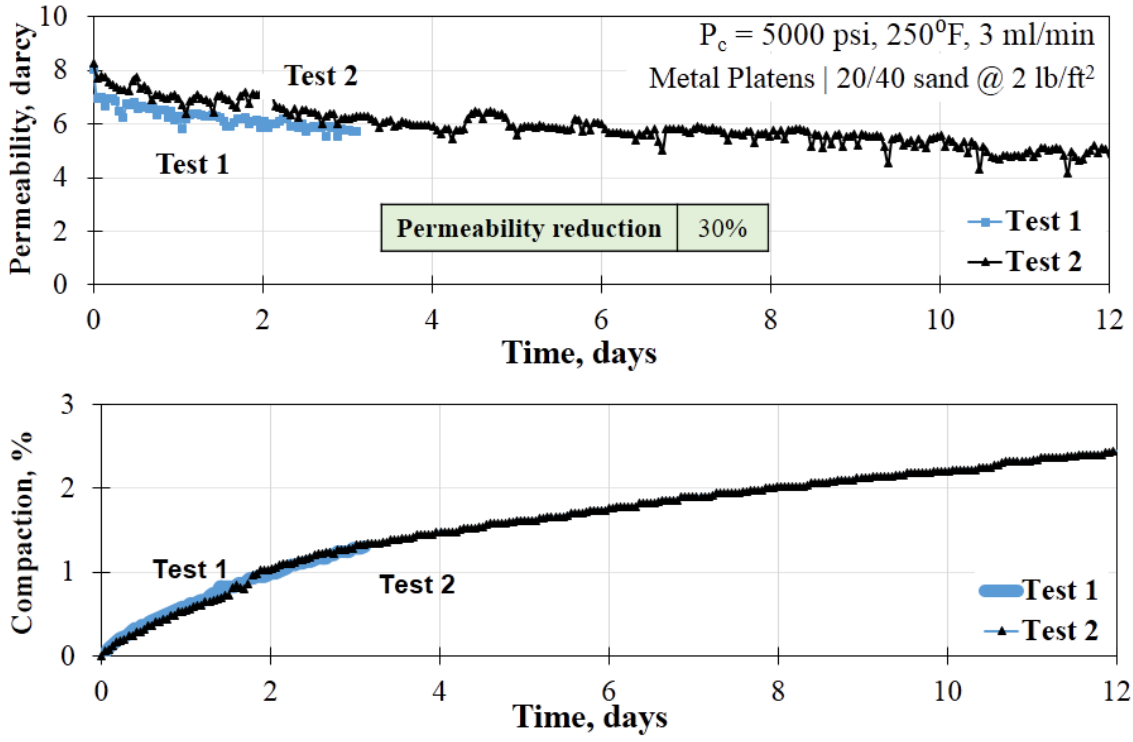

Fig. 16: Proppant-pack brine permeability for 20/40 Ottawa sand between Hastelloy platens at a proppant concentration of 2 lb/ft^2 (T= 250°F). Note there are two experimental curves, Test 2 is of longer duration than Test 1; however, over the same time interval there is good agreement.

The brine permeability measured across a proppant-pack consisting of 20/40 Ottawa sand (concentration: 2 lb/ft^2) between Hastelloy metal platens is illustrated (see **Fig. 16, top**).

The 20/40 sand suffered a loss in permeability of approximately 30 % over a span of 12 days, finally degrading to a permeability of 5 darcy. Repeating the measurement under similar conditions of proppant, closure stress, and temperature, similar results of permeability were obtained. Although the tests are for different time intervals, it should be noted that the changes in compaction are in good agreement over the time interval (see **Fig. 16, bottom**).

After the confidence in repeatability of permeability measurement was achieved, this study was extended to compare the performance of proppants of different sizes.

3.3. Effect of Proppant Size on Propped-Fracture Permeability

This study was conducted to understand the impact of proppant size on propped-fracture conductivity. For this purpose, three proppant sizes: 20/40, 40/70 and 60/100 mesh Ottawa sand were considered. The proppant characteristics, i.e. size and shape have been discussed in section 3.1 (also see **Fig. 15**).

The data for differential pressure and compaction (using LVDTs) were recorded at a frequency of 60 seconds. The proppant-packs were loaded at a similar ramp-rate of approximately 100 psi/min and had a proppant concentration of 2 lb/ft^2. All other conditions are mentioned in section 2.8.

Fig. 17 shows the normalized brine permeability for the three proppant sizes between metal platens, as a function of time. The brine permeability reduced by approximately 30% for 20/40 sand (reducing to 5 darcy), and 56% for 40/70 sand over a duration of 12 days. However, the 60/100 mesh sand experienced a drastic 99% drop in brine permeability, from 10 darcy to less than 30 md, within a much shorter duration of only 4 days. This shows that proppant performance has a direct dependence on proppant size. The smaller the proppant size, the poorer the performance.

To better understand the performance of different proppant sizes, the 40/70 and 60/100 mesh sands were examined under SEM. SEM analysis before and after the experiment was used to qualitatively evaluate the extent of damage. **Fig. 18** shows the SEM image of 40/70 sand, before and after the experiment. As a result of flow-through testing at elevated closure stress and temperature (5000 psi and 250^0F), crushing of proppant can be observed.

The native and post-experiment scans of 60/100 sand are shown in **Fig. 19**. The native sand grains are shown on the left. Post-experiment, proppant crushing can be observed in abundance, leading to generation of fines (**Fig. 19**, right). Magnified image at the bottom shows extensive fracturing across the grains throughout the proppant-pack. These minute-sized fines are capable of blocking the pore space.

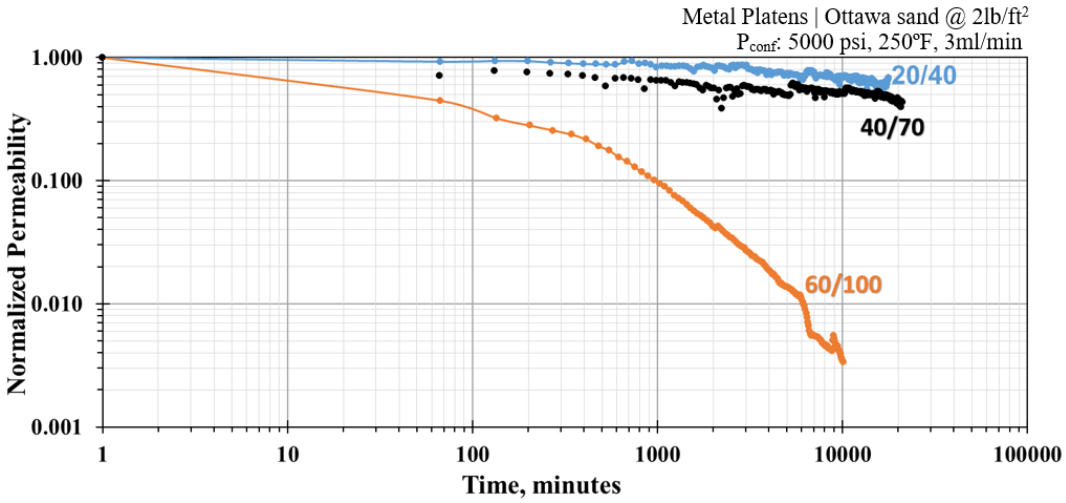

Fig. 17: Normalized brine permeability for 20/40, 40/70 and 60/100 mesh Ottawa sand tested between Hastelloy metal platens. The proppant (concentration: 2 lb/ft^2) was loaded to 5000 psi at a rate of 100 psi/min. Temperature was regulated at 250^{0}F. Brine was flowed continuously at flow rate of 3 ml/min for 12 days. Proppant size has a direct relationship with permeability. Larger proppants had better performance. The 60/100 mesh sand suffered the greatest and quickest permeability reduction under these conditions.

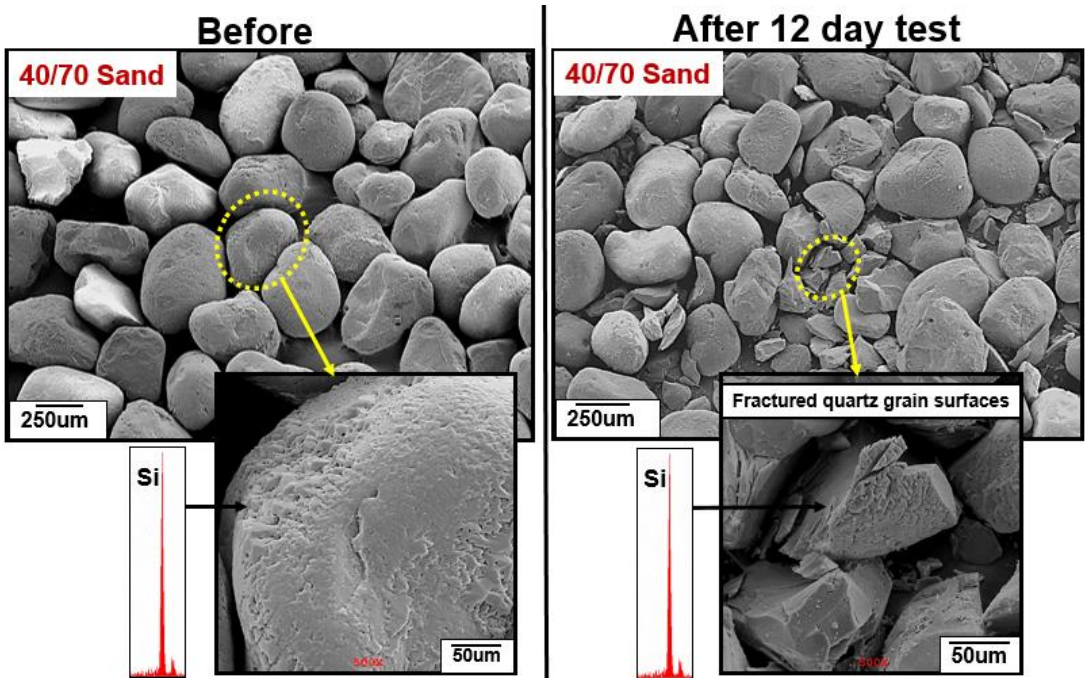

Fig. 18: Scanning electron images of rounded 40/70 sand. The native 40/70 proppant (left) has an abraded surface with quartz overgrowth in C-crystallographic orientation attributed to friction during fluid transport. Long-term testing (12 days) at 5000 psi and 250^{0}F between Hastelloy metal platens was performed. This resulted into considerable mechanical crushing of proppant (right), which resulted in generation of fines.

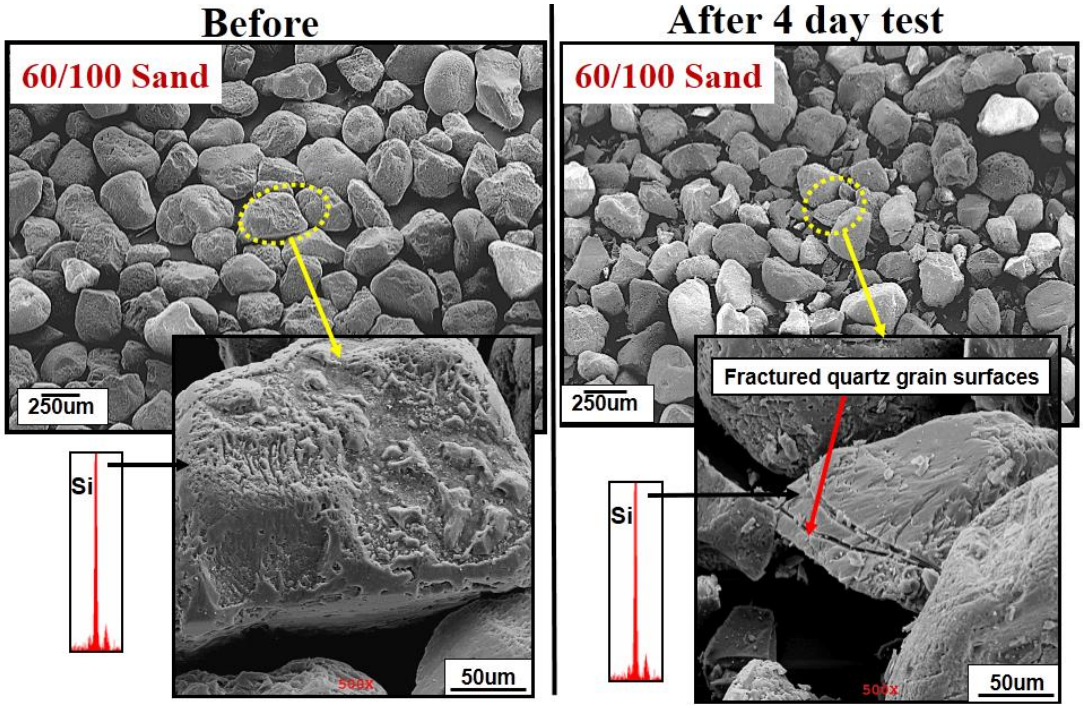

Fig. 19: Scanning electron images of very angular 60/100 sand. Abraded quartz surface of the native proppant can be observed (left). Long-term testing at 5000 psi and 250^{0}F between Hastelloy metal platens resulted in extensive mechanical crushing of angular and irregular proppant (right). Generation of very minute-sized fines capable of blocking pores is observed.

Particle size analysis of proppant grains was performed to quantify the extent of proppant crushing, and the impact on permeability reduction (see **Fig. 20**). **Fig. 20a** shows the distributions for initial 20/40 (blue-pattern) and 60/100 (orange-solid) mesh Ottawa sands. In accordance with API standards, both initial samples had less than 5% particles outside of the respective mesh sizes. Note that the smallest grains measured in initial proppant distribution are 122 µm.

Post-experiment, **Fig. 20b** shows the distribution for each proppant due to crushing. **Fig. 20b** shows grain diameter (d_{gr}) range: 0-122 µm to demonstrate proppant crushing. Significant crushing can be observed in both 20/40 and 60/100 sands. However, 15%

particles of 20/40 sand (by volume) fall below 122 μm in comparison to approximately 30% particles for 60/100 mesh sand.

Fig. 20c shows the additional fines generated due to crushing of proppants. Note that this shows only those particles that were generated compared to initial sand of that particular size, and does not account for the proportion of particles that were already present in the initial sand. **Fig. 20d** shows the coarser grains that underwent crushing for both 20/40 and 60/100 sands. These plots were obtained by subtracting the post-experiment particle distribution from the initial distribution.

The particle size analysis helps answer why the permeability through 60/100 proppant-pack between metal platens was considerably lower than 20/40 proppant-pack. The coarser 20/40 sand is expected to have larger pores compared to the finer 60/100 sand. In comparison to 20/40 sand, the presence of additional 15% finer crushed grains (by volume) of 60/100 sand are expected to plug the smaller pores in 60/100 mesh sand more rapidly leading to a quick and dramatic drop in permeability.

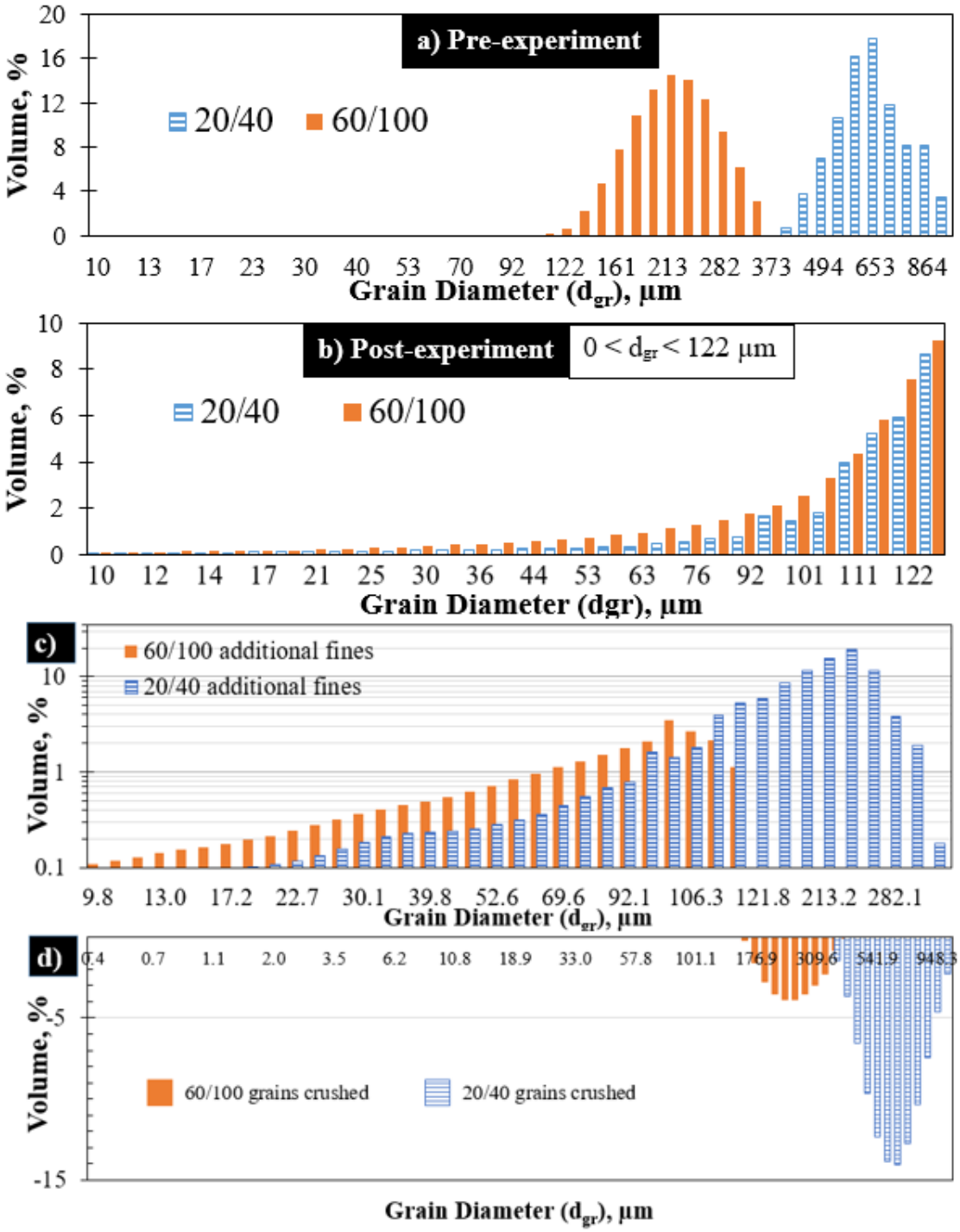

Fig. 20: Laser particle size analysis for 20/40 and 60/100 mesh sand performed a) before and b) after the experiment. Note that the graph for post experiment crushing between metal platens shows grain diameter below 122 µm. Significant crushing is observed in both 20/40 and 60/100 mesh sands. As compared to 20/40 sand, 15% additional grains of 60/100 mesh sand (by volume) fall below 122 µm. c) Additional fines generated in comparison to initial sand. d) Proportion of coarser grains that underwent crushing.

3.4. Evaluation of Fines Migration

The fines generated because of proppant crushing in addition to formation fines can migrate in the direction of flow, plugging up the pore system between proppant grains, reducing permeability. Gidley et al. (1995) demonstrated that particles finer than 100 mesh were mobilized, affecting the proppant-pack permeability considerably. Silica sands, having lower crush resistance, tend to experience greater fines migration, as compared to stronger ceramic or resin coated sands where generated fines are entrapped in the resin.

An experiment was conducted to evaluate the extent of fines migration. This was done with a proppant-pack comprising of 20/40 sand and metal platens (proppant concentration: 2 lb/ft^2). The permeability data was presented earlier (see **Fig. 16**). To quantify fines migration, particle size analysis was done on the proppant at the following three stages:

1) initial sand;

2) crushed at 5000 psi for 15 minutes; and

3) post 12 days of exposure to continuous flow-through testing at 250^0F and 5000 psi.

Fig. 21 shows the particle size distribution on X-axis, and volume on Y-axis. The initial 20/40 sand (blue-stripe pattern), in accordance with API standards, falls within the 20-40 mesh range (marked by vertical red lines). After loading the proppant at 5000 psi closure stress for 15 minutes (orange-solid), crushing of coarser grains and generation of finer particles is observed; 15% particles (by volume) fall below the finer 40 mesh sieve.

Post completion of 12 days of flow-through testing between metal platens, the proppant-pack was taken apart. The proppant grains were divided into those near the inlet and the outlet, and were analyzed with a laser particle size analyzer. The proppant size distributions at inlet and outlet are shown **Fig. 21** (black-cross pattern) (see left for inlet, and right for outlet). Zero percentage of particles (by volume) were retained within the 20/40 mesh range implying severe crushing at both the inlet and outlet. Note that between metal platens, fines are generated entirely from crushing of proppant.

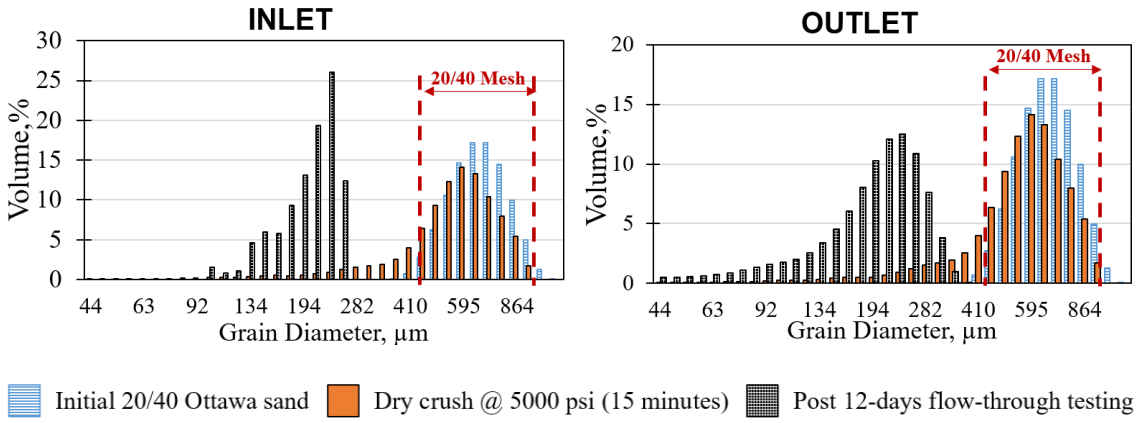

Fig. 21: Particle size analysis of the proppants collected at the inlet (left) and outlet (right). The native proppant lies in the 20/40 mesh range (blue). The proppants were crushed at 5000 psi for 15 minutes (orange). The proppant distribution after flow-through testing for 12 days (at 5000 psi and 250^{0}F) is shown in black. The changing distribution is representative of extensive crushing, and fines migration. Migration of 14% additional finer particles towards outlet can have detrimental effect on permeability.

A greater proportion of the particles belonging to coarser grain sizes were measured at the inlet. Correspondingly, particles were crushed to much smaller mesh range at the outlet. As shown in **Fig. 21** (right), the grains of proppant collected from outlet had 14% additional particles below 100 mesh size (or 149 µm), as compared to inlet. The migration of these additional crushed finer particles in the direction of flow can block pore spaces and obstruct flow, leading to drastic reductions in permeability.

3.5. Impact of Rock Mineralogy on Proppant Performance

The measurements were extended to proppant-packs containing 20/40 Ottawa sand (concentration: 1.5 lb/ft^2) and shale platens. For this study, shale platens were fabricated from Vaca Muerta and Eagle Ford shale.

The shale mineralogy was measured using transmission Fourier Transform Infrared Spectroscopy (FTIR) (Sondergeld and Rai, 1993; Ballard, 2007). The Vaca Muerta sample consisted of 12 wt% quartz, 46 wt% carbonate, 19 wt% clay, 18% feldspar and 5 wt% others. Meanwhile, the Eagle Ford sample had 41% carbonate, 58% clay and 1% others (**Fig. 22)**. Eagle Ford sample has three times greater clay content than Vaca Muerta sample. FTIR has 5 wt% error associated with the measurement of clay.

The Vaca Muerta and Eagle Ford samples had a crushed helium porosity of 3.9% and 9.4%, and LECO^{TM} TOC of 2.2 wt% and 5.1 wt%, respectively. Young's modulus was measured through nanoindentation, on dry rock before starting the experiment. The Vaca Muerta and Eagle Ford samples had a Young's modulus of 24.5±4 GPa and 15.9±2 GPa, respectively.

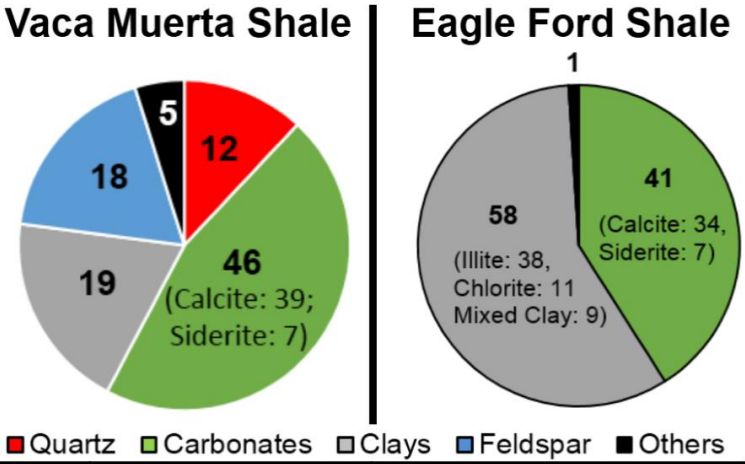

Property	Vaca Muerta	Eagle Ford
TOC, wt%	2.2	5.1
ϕ_{Helium},%	3.9	9.4
Young's Modulus, GPa	24.5 ± 4	15.9 ± 2

Fig. 22: The mineralogy of Vaca Muerta and Eagle Ford shale obtained by transmission FTIR. Eagle Ford sample has three times greater clay content than Vaca Muerta sample. Young's modulus was determined using nanoindentation technique.

The permeability for the proppant-packs with both Vaca Muerta and Eagle Ford shale platens started at 120 darcy and dropped precipitously. Within two days, the permeability dropped by approximately 50% for Vaca Muerta and 85% for Eagle Ford shale. Subsequently, even after eight days of continuous flow-through testing at similar conditions of 5000 psi and 250^{0}F, the propped Vaca Muerta platens exhibited five times greater permeability as compared to propped Eagle Ford shale platens. Fracture conductivity, product of fracture permeability and propped width, is plotted as a function of time, in days (see **Fig. 23**).

The difference in the initial conductivity is representative of the different compactions of the two rocks, primarily due to different mineralogy. After 8 days of testing, the fracture

conductivity achieved by Vaca Muerta proppant-pack (103.6 md-ft) is approximately eight times greater than the conductivity attained by Eagle Ford proppant-pack (12.8 md-ft).

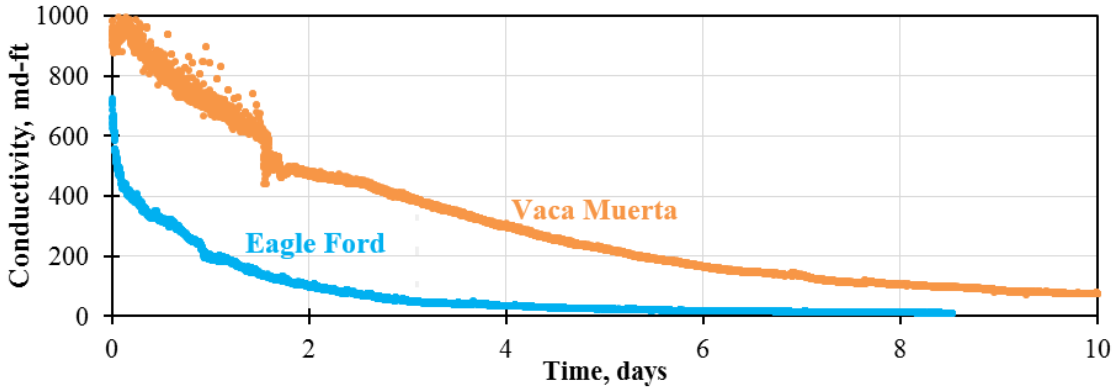

Fig. 23: Fracture conductivity (md-ft) as a function of time for Vaca Muerta (orange) and Eagle Ford (blue) shale platens. The difference in initial conductivity is due to different compactions of the two rocks, primarily due to different mineralogy. Even after 8 days of testing, the fracture conductivity achieved by Vaca Muerta platens is approximately eight times greater than the conductivity attained by Eagle Ford platens.

The LVDTs attached to the cell continuously record changes in proppant-pack thickness over time. The reduction in proppant-pack thickness, normalized to initial thickness, is shown in **Fig. 24**. The table (**Fig. 24a**) shows the step-wise procedure as the proppant-pack is loaded. The proppant-pack is initially at zero axial load (or closure stress) and at room temperature (step 1). Compaction measurement is started after an initial contact has been established. Transitioning from step 1 to step 2, an axial load of 5000 psi is applied at 100 psi/min and temperature is raised to 250^0F. The cell is left at standby for 12 hours for temperature to stabilize. Note that there is no brine flow at this stage.

Fig. 24b illustrates the changes in compaction at different stages of the experiment for metal, Vaca Muerta, and Eagle Ford rock platens. Transitioning from step 1 to step 2, the

compaction of metal proppant-pack is representative of compaction only due to rearrangement and crushing of proppant grains. The proppant-pack thickness for Vaca Muerta shale reduced by 30%, as compared to approximately 55% for Eagle Ford shale (step 1 → step 2). This compaction resulted from the application of an axial load of 5000 psi and heat and has mixed components of crushing and embedment over a period of 12 hours.

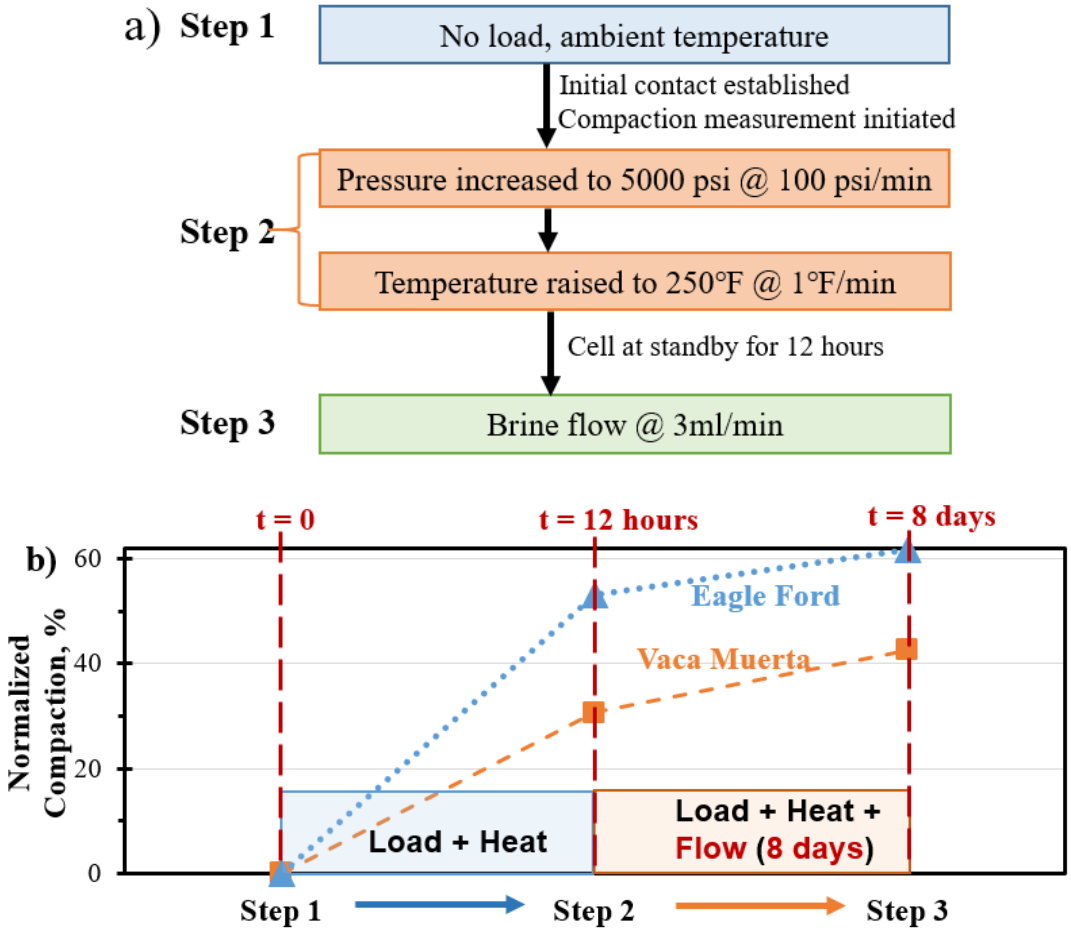

Fig. 24: Compaction measured through LVDTs for the metal (black-circle), Vaca Muerta (orange-square) and Eagle Ford (blue-triangle) tests. Table (top) describes the stress, temperature and flow conditions at different times during the experiment. The graph (bottom) shows the normalized reduction (%) in proppant-pack thickness at different steps. Any deviation from metal test is due to embedment. At the end of 8 days, 20% additional compaction is observed in Eagle Ford, as compared to Vaca Muerta. This is primarily due to different clay content.

Transitioning from step 2 to step 3 (**Fig. 24b**), the brine is flowed at 3 ml/min continuously. After 8 days, metal proppant-pack underwent 30% compaction. As compared to Vaca Muerta platens, the Eagle Ford proppant-pack thickness reduces by an additional 20%. Any deviation from metal platen response is most likely due to the embedment component. The fracture width closure (or proppant-pack thickness reduction) is continuous over time. We expect greater embedment in Eagle Ford platens, considering Eagle Ford shale has approximately three times greater clay content than Vaca Muerta shale.

The proppant-pack system comprised of 20/40 Ottawa sand and Vaca Muerta shale platens was imaged with an SEM to study the intensity of proppant-pack damage. **Fig. 25** shows the surface of a grain of 20/40 Ottawa sand after exposure to the saline solution at 250°F for 10 days; the grain has a locally pitted surface. The surface, partially corroded chemically by the fluid, has possibly weakened the proppant grains.

A manifestation of the high temperature and pressure environment can be seen in the form of fractured proppant in **Fig. 26**. The stress applied by Vaca Muerta shale platen caused extensive proppant fracturing, observed uniformly across the proppant-pack. Also, abundant precipitation of chloride flakes/grains was observed. This precipitation was seen within the fractures, as well as on the surface of the proppant.

In addition to the mechanical crushing, embedment of proppant into the shale surface was visible. Embedment, captured in compaction data (see **Fig. 24b**), does more damage than

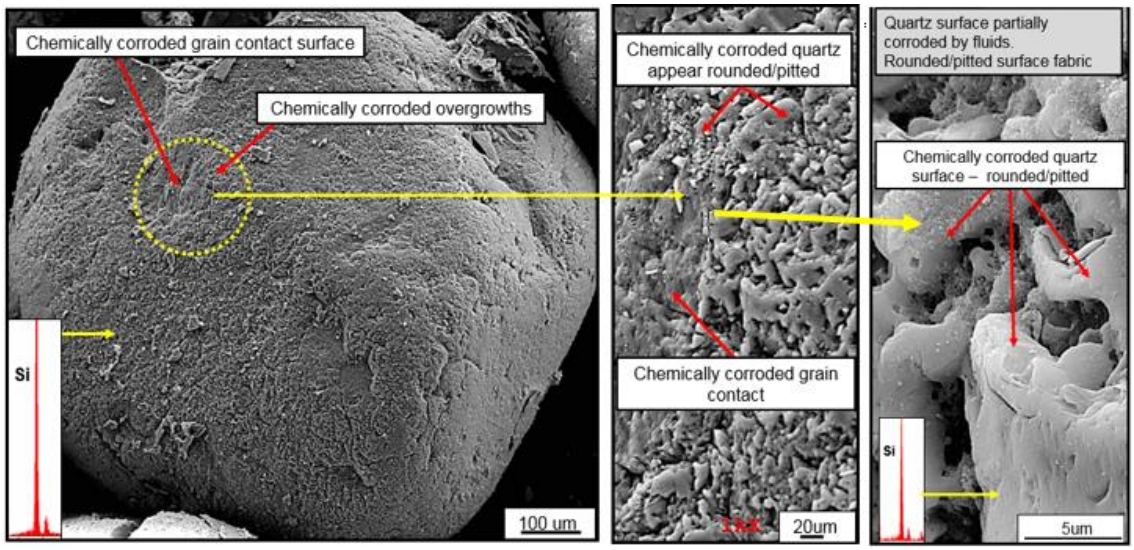

Fig. 25: Scanning electron image of the 20/40 Ottawa sand proppant after exposure to saline environment (deionized water + 3% NaCl + 0.5% KCl, by weight) at an elevated temperature of 250^{0}F between Vaca Muerta shale platens at an axial load of 5000 psi for a duration of 10 days. The quartz proppant surface suffers moderate corrosion by the fluid; this is evident from the locally pitted surface (right) of proppant grain.

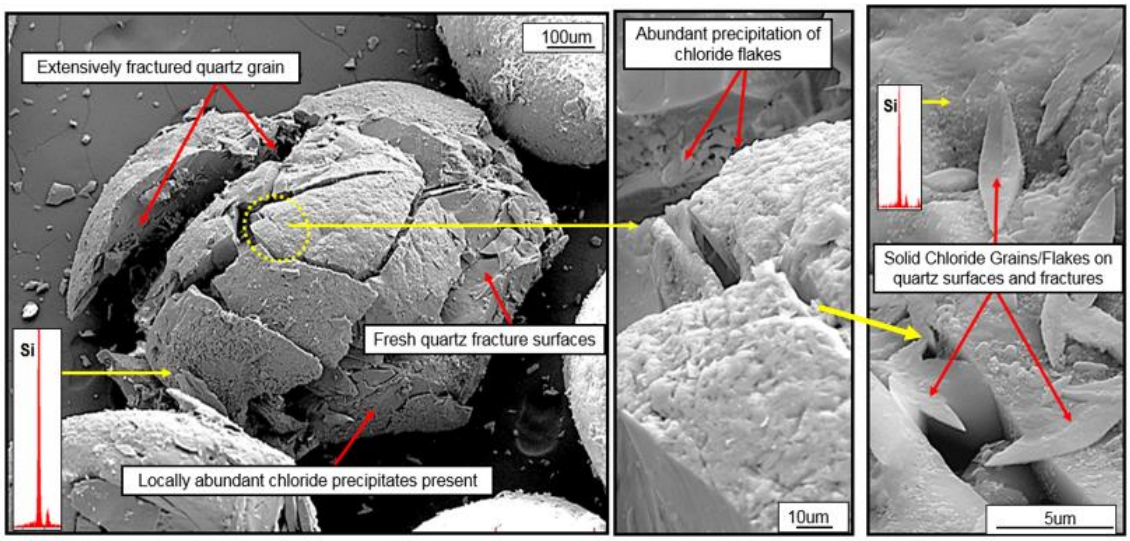

Fig. 26: Secondary electron image of the 20/40 Ottawa sand proppant from the Vaca Muerta shale experiment. Axial load of 5000 psi applied by Vaca Muerta shale platen has resulted into extensive fracturing of proppant grains (left), resulting into generation of fines. Significant mechanical crushing is observed uniformly across the entire proppant-pack. Abundant precipitation of chloride flakes/grains (right) is observed both within fractures, as well as on the surface of the proppant. The 20/40 Ottawa sand (concentration: 2 lb/ft^2) was loaded at a constant rate of 100 psi/min.

expected. Apart from continuous closure of the fracture, even after 10 days, embedment leads to dislodging of additional fines from the formation surface (see **Fig. 27**).

These shale shards dislodged from the rock surface and are of uneven shape and size. As they migrate towards the outlet, in the direction of flow, they possibly plug the pores hence leading to an increased reduction in permeability (**Fig. 27**). This coupled embedment generated fines migration was not observed in tests using metal platens, where fines observed are entirely from proppant crushing.

Fines migration has been discussed earlier in proppant-packs consisting of 20/40 Ottawa sand and metal platens (**Fig. 21**). To qualitatively verify fines migrations in Vaca Muerta shale experiment, the proppant-pack was examined under SEM at three different locations moving downstream (**Fig. 28**). Observations from EDX in SEM confirm that majority proportion of fines were crushed proppant. Near inlet (left), extensive fractured quartz proppant grains can be observed. Moving towards the outlet (right), finer proppant crushed grains can be observed (note the changing scales moving from inlet to outlet). Apart from extensive proppant crushing, SEM images verify considerable proportion of finer particles blocking the pore space towards the outlet. Ghosh et al. (2014) conducted continuous flow-through testing using Ottawa sand and Barnett shale samples. They observed extensive breakage and pore blocking by crushed Ottawa sand. This was seen as the primary reason for rapid destruction of permeability, as compared to ceramic and resin coated proppants.

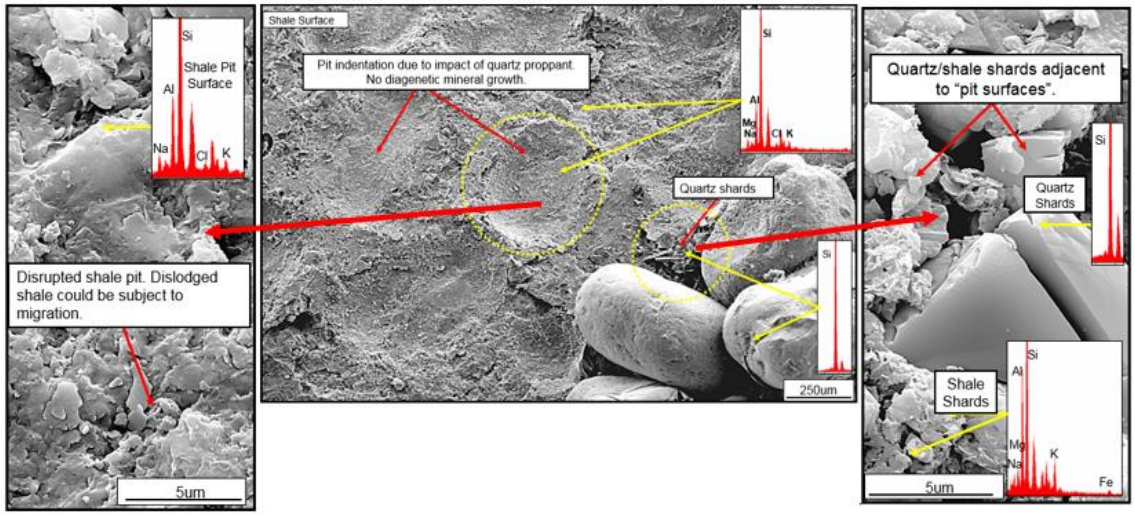

Fig. 27: Secondary electron images of the 20/40 Ottawa sand (concentration: 2 lb/ft^2) and Vaca Muerta platen system (closure stress: 5000 psi). Apart from extensive proppant crushing, significant embedment of proppant into the shale surface is observed, leading to further reduction of fracture width (center). Additional fines (quartz shards) are generated from the dislodged rock surface due to embedment (left). These fines, owing to minute size and irregular shape, could be subject to migration possibly blocking pores downstream (right).

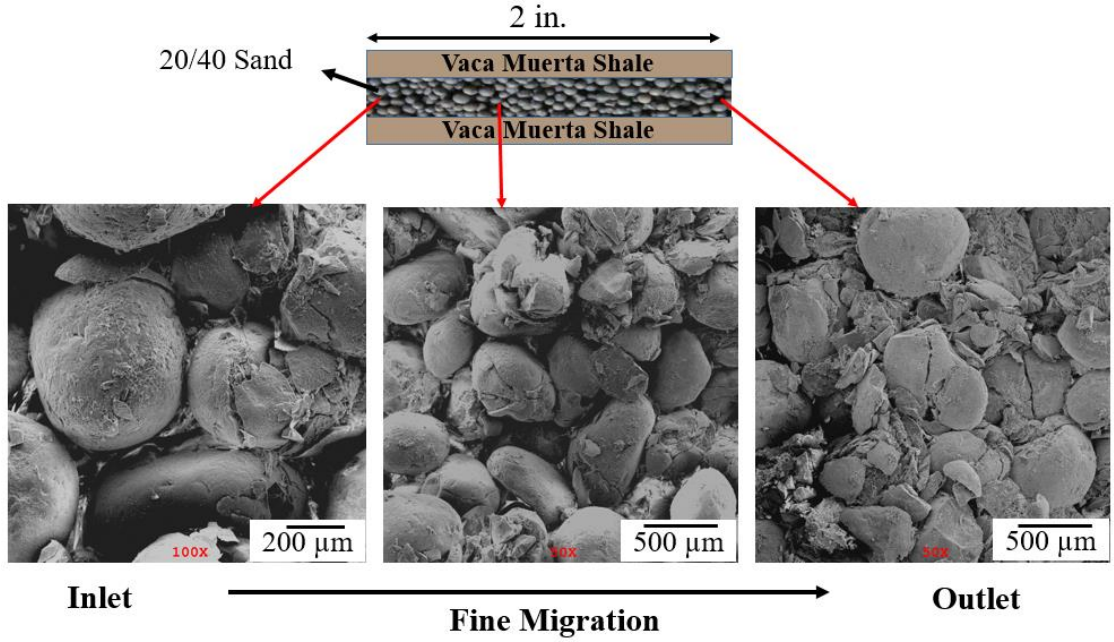

Fig. 28: Secondary electron images of proppant from Vaca Muerta shale experiment. Images were captured at different locations moving from inlet (left) to outlet (right). Note the changing scale from inlet to outlet. Apart from crushed proppant, additional fine particles can be observed at the outlet. 20/40 Ottawa sand was used at 1.5 lb/ft^2 concentration, closure stress of 5000 psi and 250^{0}F temperature.

The grains of proppant were observed using optical microscope. The native 20/40 sand is shown in **Fig. 29a**. However, after a long-term experiment between Vaca Muerta platens over a duration of approximately 10 days, the proppant experienced significant crushing (**Fig. 29c**). Apart from crushed proppant, fines from the rock were also generated. This is evident in the dark colored fine particles seen in **Fig. 29c**. However, due to their minute size, it was not feasible to separate the formation fines from crushed proppant.

Laser particle size analyzer was used to quantify the proportion of crushed grains. **Fig. 29b** is a plot of the grain diameter, and volume. Particle size distribution of native 20/40 sand (crimson), 20/40 sand after flow-through testing between Eagle Ford (blue), Vaca Muerta (orange) and metal (black) platens are shown. Any deviation from initial sand is representative of different amounts of proppant crushing. Particles as small as 2 µm could be observed, but X-axis has been clipped to 20 µm for simplicity.

The volume crush %, i.e. particles falling below 40 mesh (by volume) for the corresponding Eagle Ford, Vaca Muerta and metal platens is shown in **Fig. 29d**. After 10 days of flow-through testing, 38 % of the 20/40 proppant particles between Eagle Ford shale platens (blue), and 42% of the proppant particles between Vaca Muerta (orange) shale platen fell below 40 mesh size. As expected, most crushing was observed between metal platens.

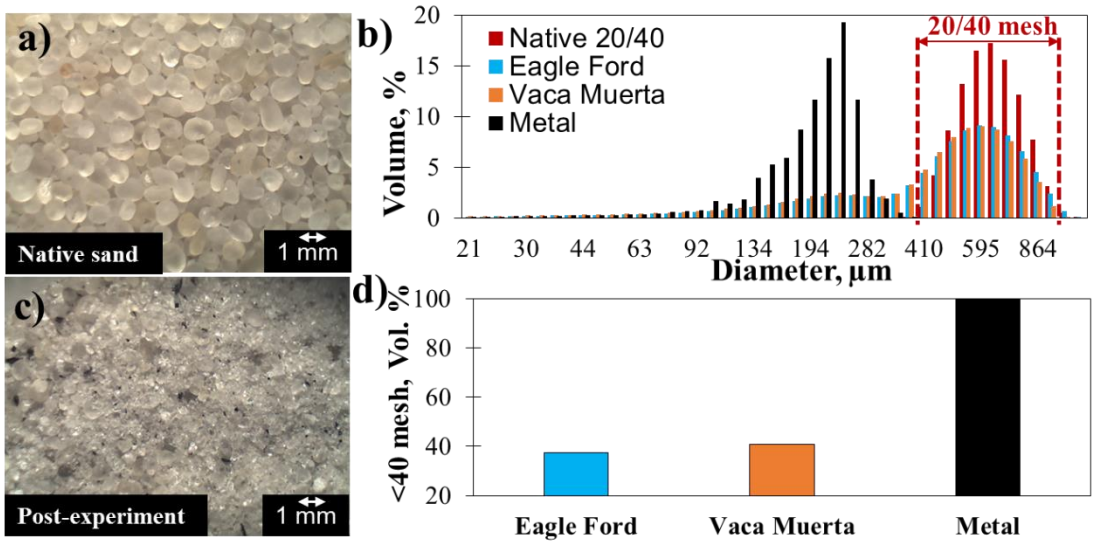

Fig. 29: Optical image of 20/40 Ottawa sand a) before and c) after the long term testing between Vaca Muerta shale platen. b) Particle size analysis of the grain size distribution for native sand (crimson), post 10-day flow-through testing between Eagle Ford (blue), Vaca Muerta (orange) shale and metal (black) platens. d) This graph shows the volume of particles (%) below 40 mesh.

The surface of the rock was examined for proppant embedment. The rock platen was originally polished to 1200 grit paper. The flat and polished surfaces of Vaca Muerta (see **Fig. 30, left**) and Eagle Ford (see **Fig. 31, left**) shale platens were then scanned using laser profilometer. The color scale shows the variation in depth in µm. The green color shows the reference average depth of the polished sample surface.

The surface of shale was again scanned with the profilometer after approximately 10 days of continuous flow-through conditions at 250^0F and 5000 psi stress. The brine was flowed through the proppant-pack consisting of 20/40 Ottawa sand (concentration: 1.5 lb/ft^2).

The embedment of 20/40 sand on the shale surface is illustrated for Vaca Muerta (see **Fig. 30, right**) and Eagle Ford (see **Fig. 31, right**) shale platens. With reference to the polished surface (green), the cooler colors (or negative scale) depict the embedment of proppant, and red colors (or positive scale) represent the height due to either proppant or extruded rock around the embedded zone.

Comparing the pre- and post- experiment profilometer scans, embedment as deep as approximately 140 μm were observed in Vaca Muerta shale, with extrusion of approximately 70 μm at some places (**Fig. 30**). However, in Eagle Ford platens, embedments as deep as 350 μm were measured, with little extrusion between grains (**Fig. 31**). The proppant sticking on the rock surface was removed using a brush. But some of the proppant was so embedded that they could not be removed. At some locations, these show up as hills (or positive heights depicted by red color). Notice the red color in top left corner in **Fig 31 (right)** is associated with proppant that could not be removed.

Laser profilometer is a direct measure of proppant embedment, and the observed difference seems primarily due to the respective rock mineralogy. Eagle Ford sample tested in this study had three times greater clay content than Vaca Muerta shale. Correspondingly, embedment (measured using profilometer) in Eagle Ford is approximately 2.5 times deeper than Vaca Muerta shale sample. This confirms the notion that a rock with greater proportion of soft components will undergo greater proppant embedment. Proppant embedment leads to a reduction of the fracture aperture, and can have significant impact on reduction of proppant-pack permeability.

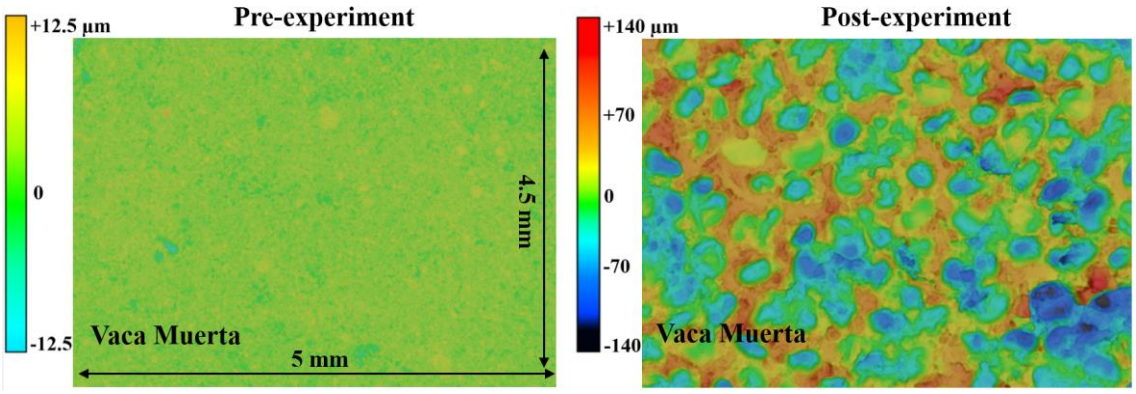

Fig. 30: Laser profilometer scan of Vaca Muerta shale platen before (left) and after (right) the experiment. The platen was initially polished using 1200 grit. The color scale shows variation in depth in µm. The green color is the reference average depth for polished surface (left). After the experiment (right), the blue color represents embedment and red shows uplifted/extruded zones around the embedment. For Vaca Muerta shale platen, approximate embedment of around 140 µm can be observed. The embedment is from 20/40 Ottawa sand (concentration: 1.5 lb/ft^2), 5000 psi axial load and 250^{0}F, when brine was flowed for a duration of approximately 10 days.

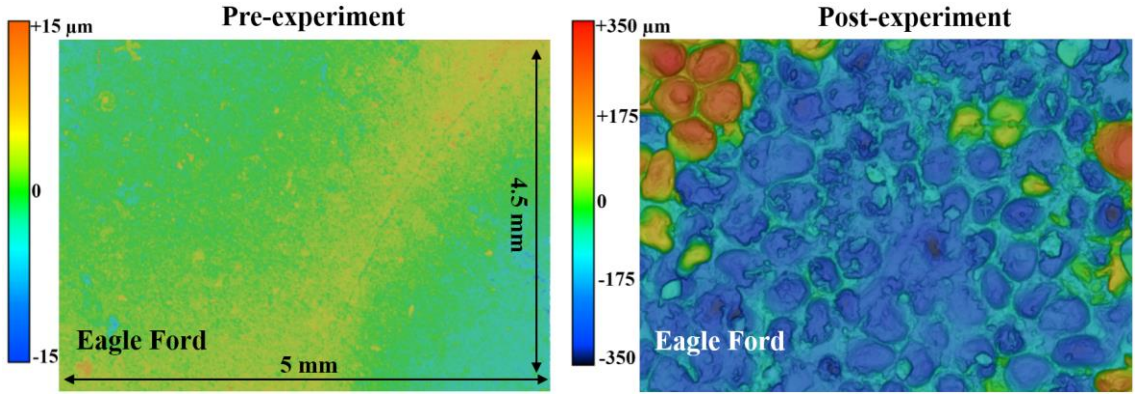

Fig. 31: Laser profilometer scan of Eagle Ford shale platen before (left) and after (right) the experiment. The platen was initially polished using 1200 grit. The color scale shows variation in depth in microns. The green color is the reference average depth for polished surface (left). After the experiment (right), the blue color represents embedment and red shows uplifted/extruded zones around the embedment. For Eagle Ford shale platen, approximate embedment of around 350 µm can be observed. Note that the red color in top-left corner represents proppants that could not be removed from the rock surface. Deeper embedment is expected owing to greater clay content, as compared to Vaca Muerta shale.

The root-mean-square roughness of the shale platen surface was measured using the laser profilometer before and after the experiment. For Vaca Muerta shale, a change from 2 µm to 36 µm was observed, as compared to 68 µm for Eagle Ford sample (**Table 1**). Eagle Ford sample was approximately twice as rough due to deeper embedment. Also, based on profilometer scans, the embedment in Eagle Ford was equivalent to 40-85 % the grain size of 20/40 proppant, as compared to 15-30 % of the grain diameter of 20/40 sand for Vaca Muerta shale.

TABLE 1

	Surface Roughness (RMS), µm		**Embedment proportion of grain diameter (%)**
Rock	**Pre-experiment**	**Post-experiment**	(using Profilometer)
Vaca Muerta (Clay: 19%)	2	36	15-30
Eagle Ford (Clay: 58%)	2	68	40-85

3.6. Effect of Time

A long-term (60-day) permeability measurement was conducted across a proppant-pack consisting of 20/40 mesh Ottawa sand (concentration: 2 lb/ft^2) and Vaca Muerta shale at similar closure stress and temperature conditions (5000 psi, 250ºF). Brine was prepared using deionized water mixed with 3% NaCl and 0.5% KCl (by weight) was used. For a long-term experiment, the permeability started at 80 darcy (**Fig. 32**); however, it dropped precipitously and seemed to stabilize at approximately 70 md after 15 days. The permeability continued to drop gradually, and reduced to approximately 35 md after 60 days.

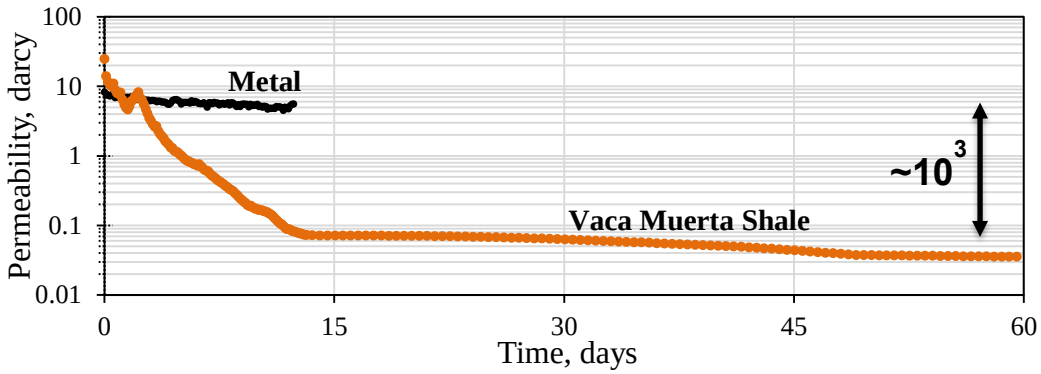

Fig. 32: Comparison of brine permeability for Vaca Muerta shale and metal platens. 20/40 Ottawa sand at 2 lb/ft^2 concentration was used. Brine was flowed at 3 ml/min (0.027 bbl/D) while 5000 psi closure stress and 250ºF temperature was maintained. The brine permeability for Vaca Muerta shale dropped precipitously to 35 md over a period of 60 days.

The proppant-pack was imaged under the SEM and EDX performed. **Fig. 33** illustrates pore space between the grains of 20/40 mesh Ottawa sand, blocked by fractured quartz remnants from the crushed proppant. The minute-sized fines generated from proppant and formation tend to be carried in the direction of flow. Over time, obstruction led to more than 99% reduction in brine permeability of proppant-pack.

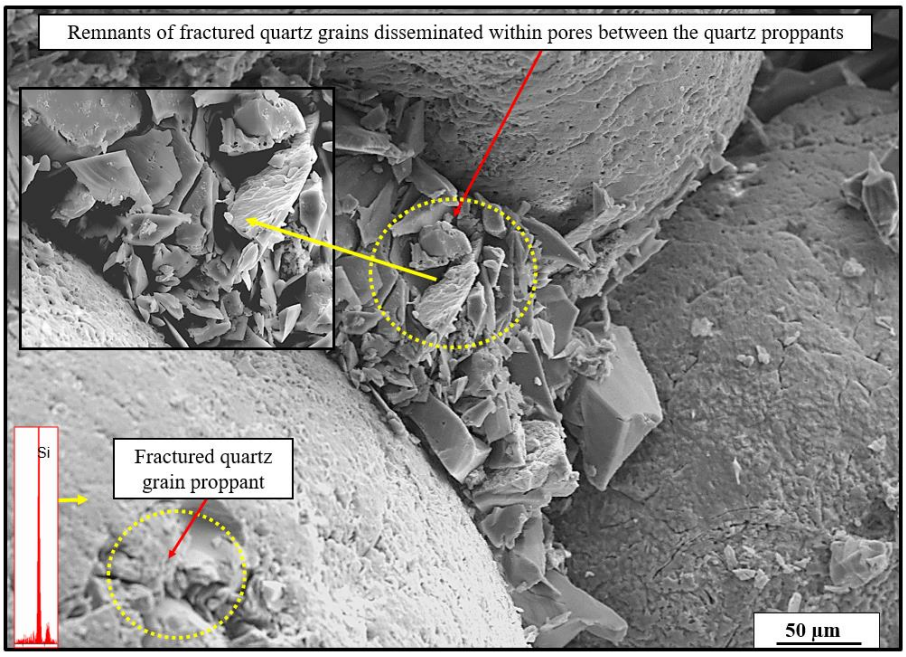

Fig. 33: Secondary electron image of 20/40 Ottawa sand. The 20/40 sand (2 lb/ft2) was tested between Vaca Muerta shale platens at a closure stress of 5000 psi, 250ºF temperature for 60-day experiment. Pore space between the grains of 20/40 sand blocked by crushed proppant (confirmed by EDX in SEM).

Fig. 34 presents the highly fractured proppant grains embedded into the surface of the rock. The embedment has dislodged particles from the rock surface. Considerable proppant crushing, fines migration, closure of propped-fracture due to proppant embedment collectively have led to reduction in proppant-pack permeability by more than 99% in 60 days. However, for this experiment between a simplistic system of proppant and rock in 3% NaCl and 0.5% KCl (by weight), no growth of diagenetic minerals capable of affecting proppant-pack permeability was observed.

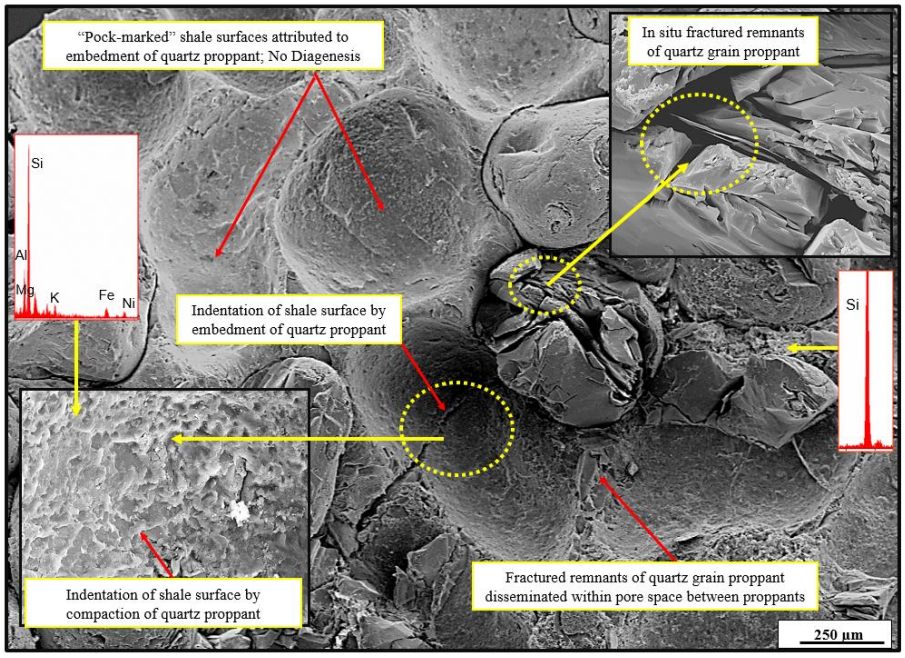

Fig. 34: Secondary electron image of 20/40 Ottawa sand embedding into the Vaca Muerta shale platen. The embedment has dislodged particles from the rock surface. Considerable damage from proppant crushing, fines migration, closure of propped-fracture due to proppant embedment collectively have led to the reduction in proppant-pack permeability. However, no growth of diagenetic minerals capable of affecting proppant-pack permeability was observed in this simple rock-proppant-brine system.

During a long-term experiment, it is expected that crushing and rearrangement of proppant grains dominate the initial stage of the experiment, as the closure stress is applied. This is followed by embedment and fines migration. We suspect that at a later stage, pressure solution and diagenesis can happen, driven by the appropriate chemical environment, which is dependent on fluid and rock chemistry. Our experiments are such that we cannot determine the precise onset of any particular process. Breaks in slope observed in **Fig. 32** are possibly representative of these mechanisms, and needs further evaluation.

3.7. Impact of Fluid Chemistry on Proppant Performance

Hydraulic fracturing can involve the use of a cross-linked fluid system. For example, borate cross-linked gel fluids involve the use of borate ions to crosslink hydrated polymers (guar and hydroxypropyl guar-HPG) and provide increased viscosity. It is claimed that these jobs are efficient because the crosslinking action is reversible and helps achieve good performance due to efficient cleanup. The crosslinking action is triggered by altering the pH of the fluid system. Properties like effective clean-up, ability to pump higher proppant concentrations as well as large diameter proppants, stable fluid rheology at temperatures as high as 300°F, and good transportability of proppant has led to extensive use of this technique in both low and high permeability formations (Halliburton, 2013; Palisch et al., 2010). Although alkaline systems make the clean-up process efficient, the long-term effect on the proppant performance has not been evaluated.

Dry crush tests were conducted to evaluate the effect of heat and brine treatment on proppant. To evaluate the impact of different alkalinity brines and heat treatment of proppants, the following procedure was adopted to perform dry crush tests. The 20/40 Ottawa sand was exposed to two different brine systems (pH:7 and pH:10, described in **Fig. 35c**) at 200^{o}F in a sealed beaker as shown in schematic (**Fig. 35a**). The treatment was conducted for a period of 10 days, and silica concentration was measured through Inductively Coupled Plasma (ICP) test (**Fig. 35d**). Over 10 days, higher silica concentration was measured for alkaline (pH:10) brine treatment. The proppant grains were then subjected to uniaxial loading (5000 psi for 15 minutes) between Eagle Ford shale platens at a proppant concentration of 1.5 lb/ft^2 (as shown in **Fig. 35b**).

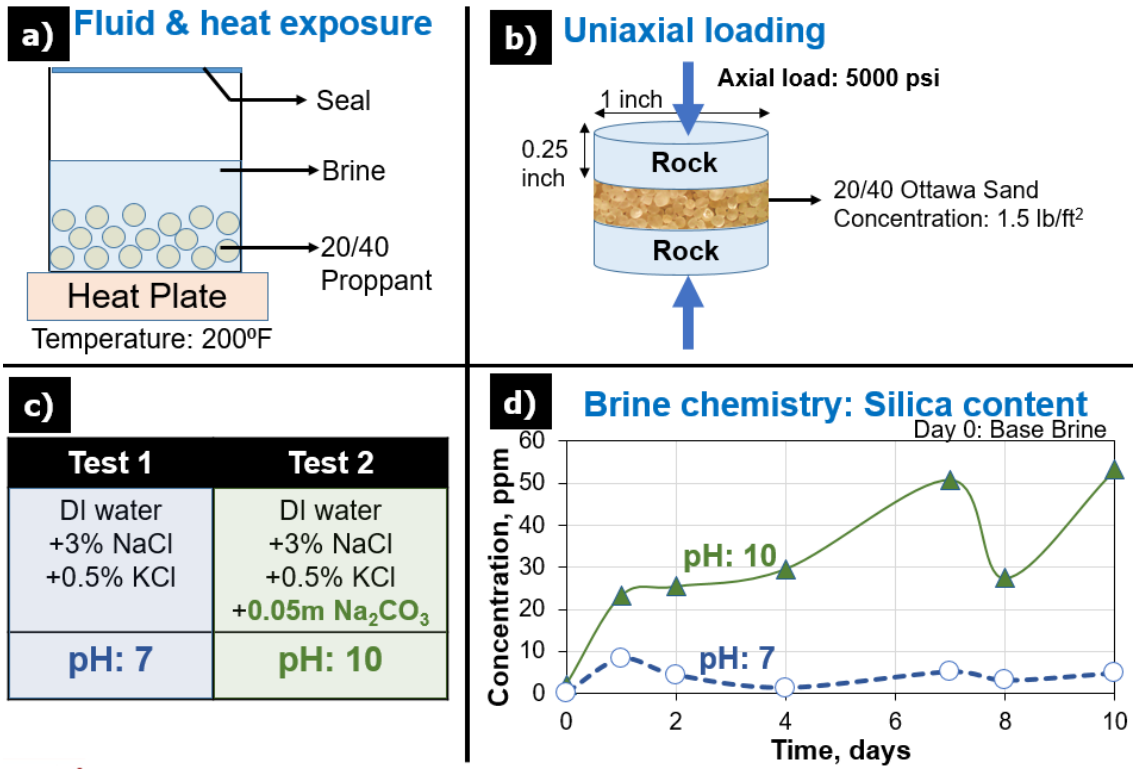

Fig. 35: Procedure for heat and fluid treatment of 20/40 sand between Eagle Ford platens. a) Heated to 200ºF in a sealed beaker for 10 days. b) Uniaxial loading to 5000 psi for 15 minutes (at a proppant concentration of 1.5 lb/ft^2). c) Two different brine systems were used: pH:7 and pH:10. d) High silica dissolution was observed in pH:10 treatment (measured through ICP testing).

The proppant was evaluated for particle size analysis to quantify proppant crushing. **Fig. 36** shows the particle size distribution with grain diameter on x-axis. The graph shows particle size distribution for a) initial 20/40 Ottawa sand proppant; b) initial 20/40 sand proppant crushed for 15 mins; c) 20/40 Ottawa sand treated with pH: 7 brine (at 200°F for 10 days); and d) 20/40 Ottawa sand treated with pH: 10 brine (at 200°F for 10 days). Generation of finer particles due to crushing can be observed for all crush tests.

Most crushing is observed for proppants that underwent heat treatment with basic brine. The crush percentage is quantified in **Fig. 37**. Particles below 40 mesh are quantified as

proppant crush volume percent. The proppant treated with pH:10 brine registered 2.5 times greater amount of crushed particle as compared to native and pH:7 treated brine. However, note that this evaluation is over a short span of 15 minutes between Eagle Ford shale platens at a concentration of 1.5 lb/ft^2. Dynamic test would give a complete picture of performance over a relatively longer time.

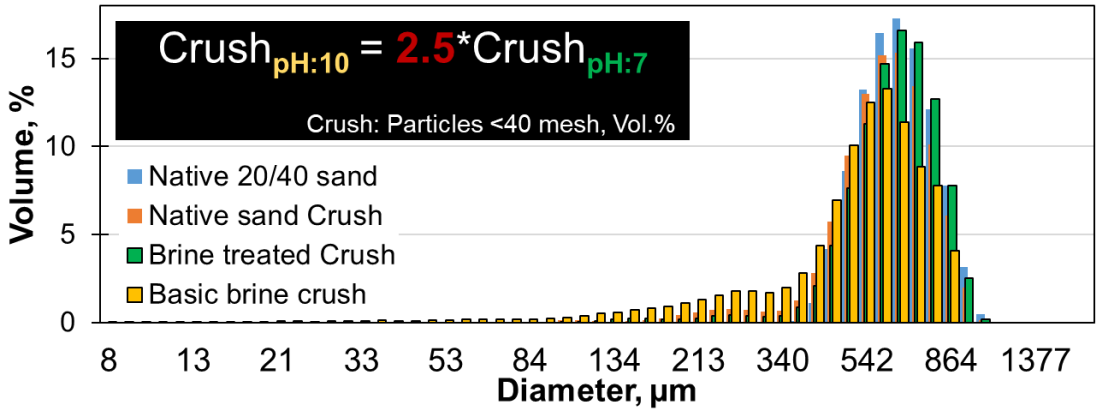

Fig. 36: Particle size distribution for dry crush test of heat and brine treated proppants. The dry crush test was conducted using 20/40 Ottawa sand at a concentration of 1.5 lb/ft^2. Greater crush was observed for the proppant exposed to alkaline brine (pH:10) at 200°F over a duration of 10 days.

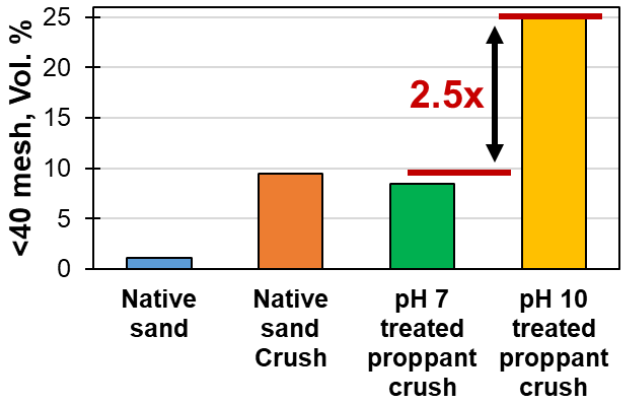

Fig. 37: Proppant crush (volume percent) for particles falling below 40 mesh. pH:10 and heat treated proppants registered a 2.5 times greater crush as compared to native and pH:7 treated proppant. The results are from a 15-minute dry crush test between Eagle Ford platens at a concentration of 1.5 lb/ft^2.

Dry crush tests (at 5000 psi over 15-minutes) discussed earlier demonstrated that exposure to alkaline brine (pH: 10 at 200°F over 10 days) led to greater crushing of 20/40 Ottawa proppant (see **Fig. 37**). A set of experiments was conducted to evaluate the effect of brine chemistries on proppant performance under dynamic conditions.

For this study, similar Eagle Ford shale platens were used for all the three experiments. The petrophysical properties of the Eagle Ford shale have been discussed earlier (see **Fig. 22**). 20/40 quartz proppant at a concentration of 1.5 lb/ft^2 was used for this study. As shown in **Fig. 38**, three fluid systems were tested to simulate sub-surface fluid environment. Case 1 is a pH: 7 fluid system composed of distilled water mixed with 3% NaCl and 0.5% KCl, by weight. For case 2, the pH was raised to 10 by adding 0.05m Na_2CO_3. In case 3, apart from a similar pH: 10 system, basalt was added. Formations like Vaca Muerta, Niobrara, and Eagle Ford have been found to possess bedded fractures filled with volcanic ash (Calvin et al., 2015; Lejay et al., 2017). Basalt (surrogate for volcanic ash) was used to simulate propped-fracture system more representative of in-situ conditions. Basalt (crushed and sieved to 20/40 mesh size, < 5 wt%) was added to the rock-proppant-brine system.

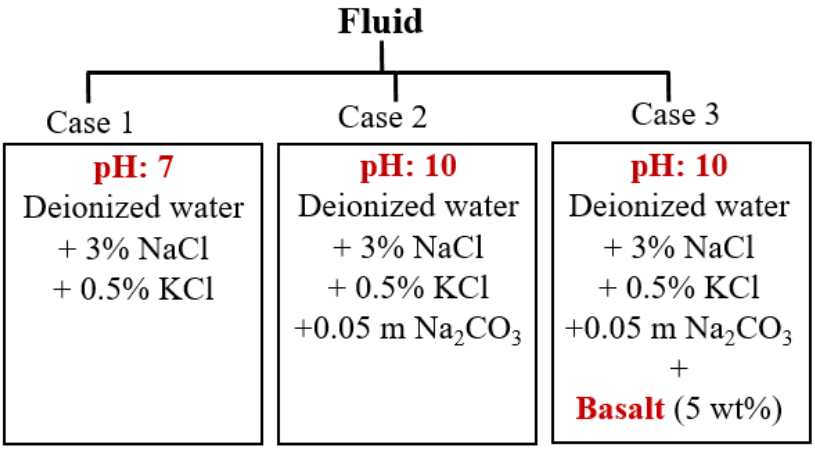

Fig. 38: Brine chemistry for the 3 fluid systems tested with Eagle Ford platens and 20/40 Ottawa sand (concentration: 1.5 lb/ft^2). The salts were added by weight percent. Sodium carbonate was used to raise the alkalinity to pH: 10. Basalt, surrogate for volcanic ash, was added to introduce cations like sodium, potassium, magnesium, and aluminum to closely imitate the subsurface environment.

The comparison in permeability for the different cases is shown in **Fig. 39**. The permeability for 20/40 sand between metal platens with pH:7 brine (represented in black) is compared to the permeability between Eagle Ford platens between three different brine systems, keeping other parameters (like proppant type, concentration, temperature, flow rate, closure stress, etc.) consistent with section 2.8. **Fig. 39a** shows permeability variation for six days. The progress from six days onwards is shown in **Fig. 39b**. Note that the permeability in **Fig. 39b** is on a logarithmic scale for the purpose of comparison. Even after eight days of testing, the brine-permeability for metal is 3 times greater than the brine-permeability between Eagle Ford platens under a similar pH:7 brine system. The brine-permeability for Eagle Ford platens with the pH:10 brine systems (with basalt - green and without basalt - crimson) drops at a steeper rate than the pH:7 brine system. It is interesting to note that most permeability declines for both pH:10 systems are within the first-two days, and, as expected, follow a similar trend. After eight days of testing,

comparing the performance of Eagle Ford platens, the pH:10 brine-permeability is lower than pH:7 brine-permeability by a factor of 10. Also, the brine-permeability of pH:10-Eagle Ford system is lower than pH:7-metal system by a factor of 30 (See **Fig. 39b**).

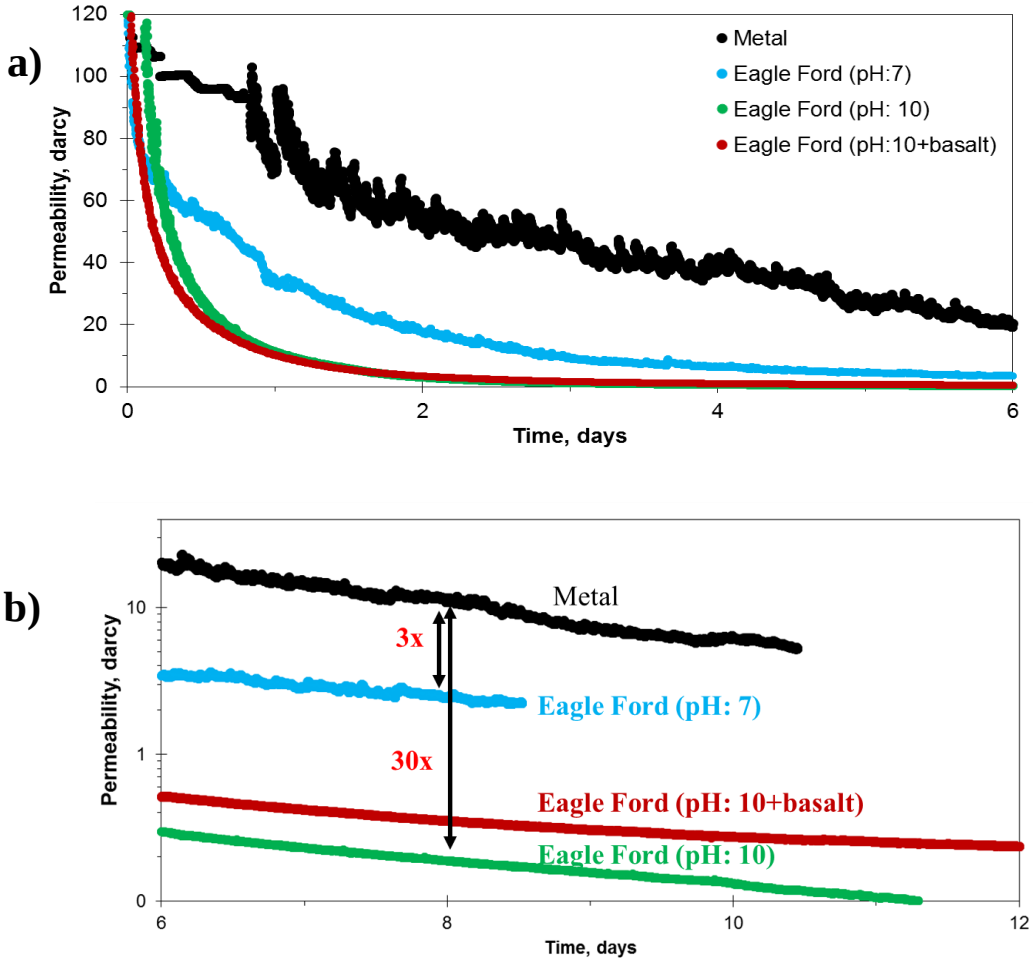

Fig. 39: Permeability variation over time for the three brine systems, comparison between metal and Eagle Ford platens. Duration: a) 0-6 days, b) 6-12 days. 20/40 Ottawa sand was used at a proppant concentration of 1.5 lb/ft^2.

To further understand the difference in permeabilities of these systems, the variations in compactions were compared. The compaction of fracture width (or proppant-pack) was computed using the LVDT data. The sequence of the experimental procedure involving changes in pressure, temperature, and flow conditions over different stages of the experiment have been presented in **Fig. 40a**.

The proppant-pack is initially at zero axial load (or closure stress) and at room temperature (step 1). Compaction measurement is started after an initial contact has been established. Transitioning from step 1 to step 2, an axial load of 5000 psi is applied at 100 psi/min and temperature is raised to 250ºF. The cell is left at standby for 12 hours for temperature to stabilize. Note that there is no brine flow at this stage.

Fig. 40b illustrates the changes in compaction at different stages of the experiment for pH:7 (metal), pH:7, pH:10 and pH:10 + basalt between Eagle Ford platens. Transitioning from step 1 to step 2, the compaction of metal proppant-pack is representative of compaction only due to rearrangement and crushing of proppant grains. Transitioning from step 2 to step 3 (**Fig. 40b**), the brine is flowed at 3 ml/min (approximately 0.03 bbl/D) continuously. After 8 days, metal proppant-pack underwent 32% compaction. As compared to metal platens, the Eagle Ford proppant-pack thickness reduces by an additional 29% approximately (for all brine systems). Any deviation from metal is most likely due to the embedment component.

The transition from step 3 to step 4 is representative of time change, with all other pressure, temperature and flow conditions being constant. The fracture width closure (or proppant-pack thickness reduction) is continuous over time, validating the creep aspect of fracture width reduction. Over a period of 18 days, the pH:10 + basalt brine system underwent a gross compaction of 90% due to combined effects of proppant rearrangement, crushing, fines migration, and embedment.

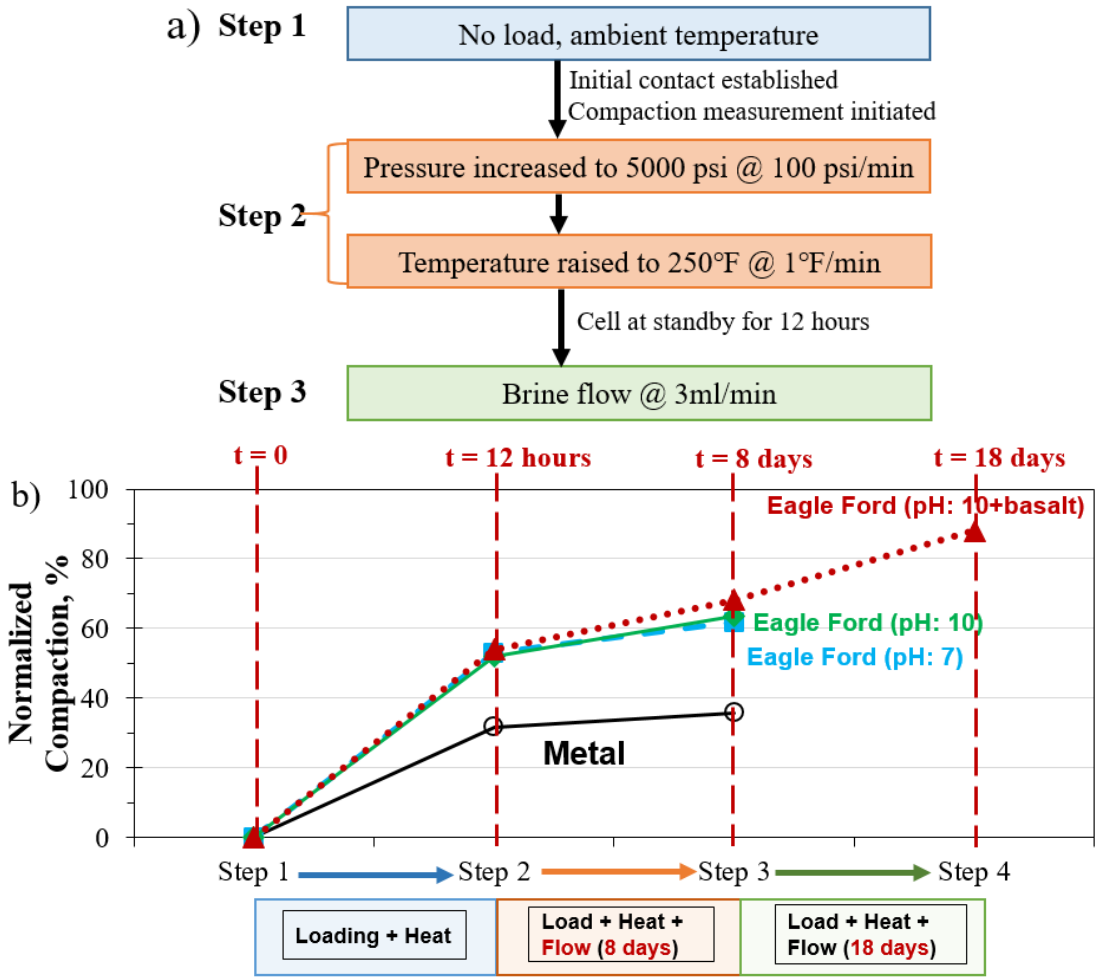

Fig. 40: Compaction measured through LVDTs for the metal-pH:7 (black-circle), Eagle Ford-pH:7 (blue-square), Eagle Ford-pH:10 (green-diamond), and Eagle Ford-pH:10+basalt (crimson-triangle) tests. 20/40 Ottawa sand (concentration: 1.5 lb/ft^2) was used between Eagle Ford platens. Table (top) describes the stress, temperature and flow conditions at different times during the experiment. The graph (bottom) shows the normalized compaction (%) in proppant-pack thickness at different steps. Any deviation from metal test is due to embedment component. At the end of 18 days, the propped fracture between Eagle Ford platens compacted by a staggering 90%.

The surface of the rock was scanned using laser profilometer to measure embedment craters on the rock surface leading to closure of proppant-pack. The Eagle Ford platens for both pH:7 and pH:10 experiments were polished to 2 µm RMS (Root mean square average) roughness before the experiment. **Fig. 41** shows the embedment profiles after

the proppant-pack underwent a closure stress of 5000 psi with 20/40 sand at 1.5 lb/ft^2, and 250ºF. **Fig. 41 (left)** shows the embedment profile when the fluid system was pH:7. The green color (or zero on depth scale) is representative of the polished rock surface before experiment. After testing, the cooler colors (or negative scale) show embedments, and the hotter colors (or positive numbers on depth scale) show upliftments/extrusions. These can either be associated with uplifted rock surrounding the embedment (see central part of Fig. 38-left), or due to proppant that were still stuck to the surface and could not be separated from the rock (see top-left corner of **Fig. 41-left**).

Fig. 41 (right) shows the embedment profile of the similar Eagle Ford platen which has undergone similar testing in a pH:10 fluid environment. Note that the embedments for pH:10 experiment (Fig. 38, right) are visibly wider than the ph:7 experiment (Fig. 38, left). This is due to the fact that pH:10 experiment ran for a longer duration than the pH:7 experiment. Overall, a similar embedment depth of 350 µm was measured for both platens, which corresponds to approximately one grain diameter of the 20/40 Ottawa proppant. For both the cases, RMS roughness changed from 2 µm (initial polished surface) to 68 µm (post-experiment).

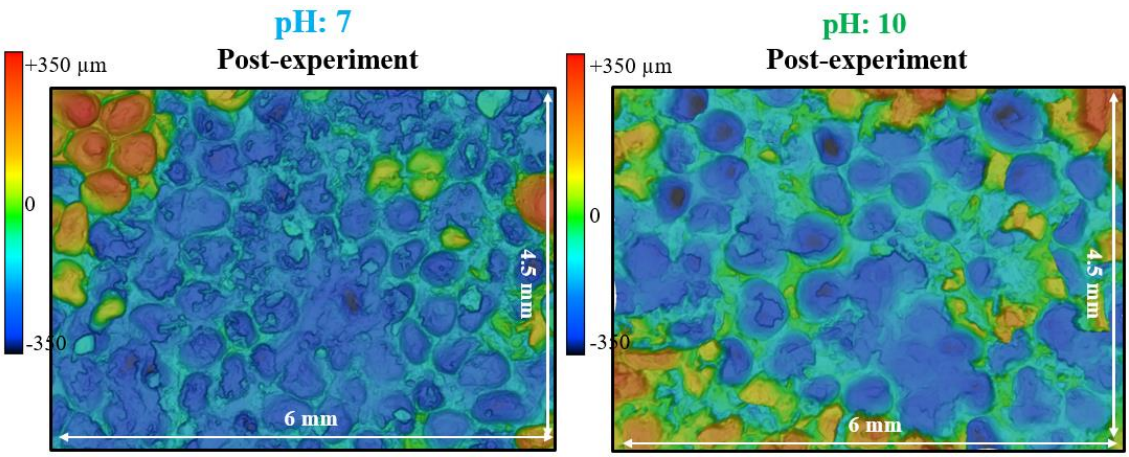

Parameter	Pre-experiment	Post-experiment
Surface Roughness (RMS), µm	2	68

$$Embedment\ depth \approx 1\ grain\ diameter$$

Fig. 41: Proppant embedment profiles for pH:7 (left) and pH:10 (right) brine systems. 20/40 Ottawa sand (concentration: 1.5 lb/ft^2) was used between Eagle Ford platens. The color scale represents depth. Green color (or zero) shows reference surface of the polished rock before experiment. Cooler colors (negative scale) shows embedment of proppant into the rock surface. Hotter colors (positive scale) shows either extrusions around the embedded zones or upliftment due to proppant stuck on rock surface.

To understand the extreme drop in permeability for case C (Eagle Ford proppant-pack with pH:10 brine and basalt), and the similarity in compaction and embedment profiles, we examined the proppant under the SEM. **Fig. 42a** shows extensive crushing of proppant resulting into generation of fines, which upon migration could block the pore space between proppant grains destroying permeability. The closure stress of 5000 psi in high temperature environment has resulted in the development of fracture across the proppant grains (see **Fig. 42b** and **42c**). Most of mechanical damage, like crushing, is expected to happen in the initial span of the proppant testing (or during a stimulation operation in the well).

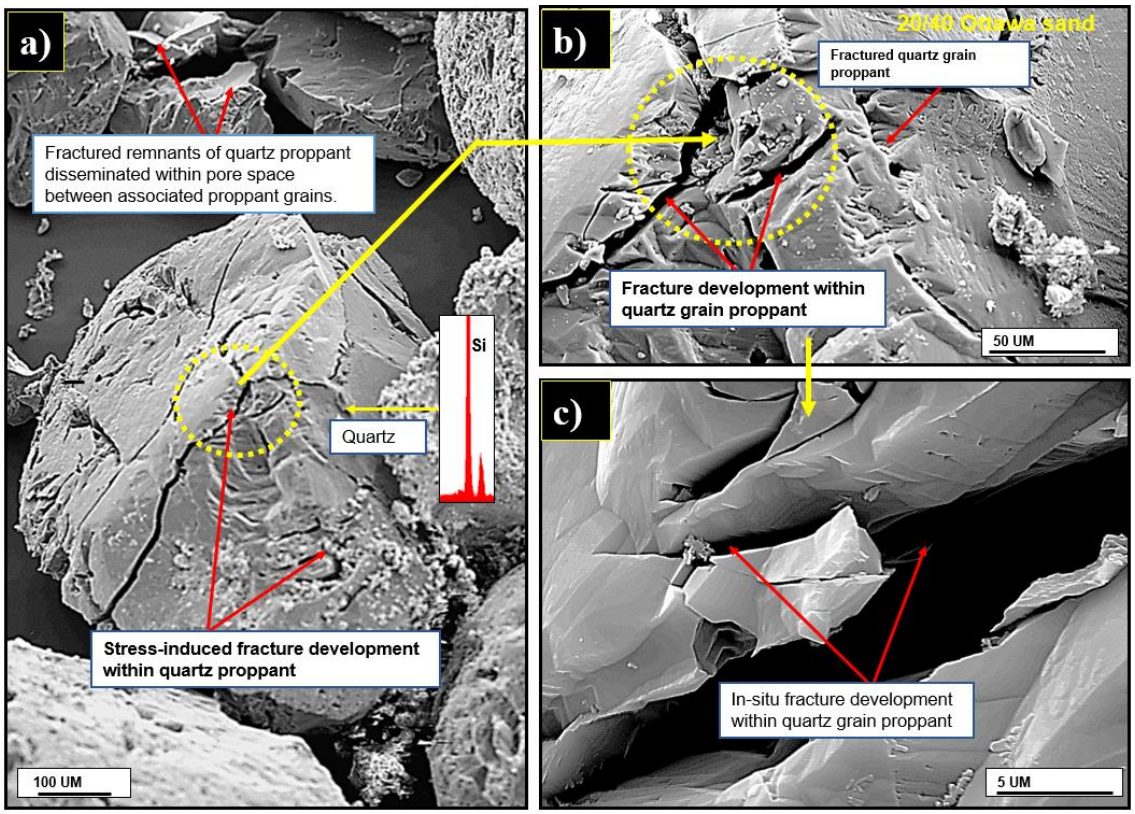

Fig. 42: SEM images of 20/40 Ottawa sand (concentration: 1.5 lb/ft^2) after testing between Eagle Ford shale in presence of alkaline environment (pH:10) and basalt. a) Extensive crushing of proppant grains leading to generation of fines. b and c) Closure stress of 5000 psi resulted into development of fracture across the grains of proppant.

Apart from mechanical damages reported earlier, the proppant-pack was also scanned for possible secondary growths that could lead to the reduced permeabilities. **Fig. 43a** shows a grain of the 20/40 sand with some coating. A closer scrutiny with EDX confirms the growth of incipient smectite clay coating (see **Fig. 43b**). Growth of extensive fracture networks across the proppant grains can be seen (note the red-dashed lines on proppant surface in **Fig. 43c**). The entire surface of the proppant seems to be covered with a coating of diagenetic smectite. The fracturing of proppant possibly exposes fresh silica surfaces. Under favorable chemical conditions and over long duration of time, an extensive

development of diagenetic smectite network with associated micro-pore development between clay platelets is observed (**Fig. 43d**).

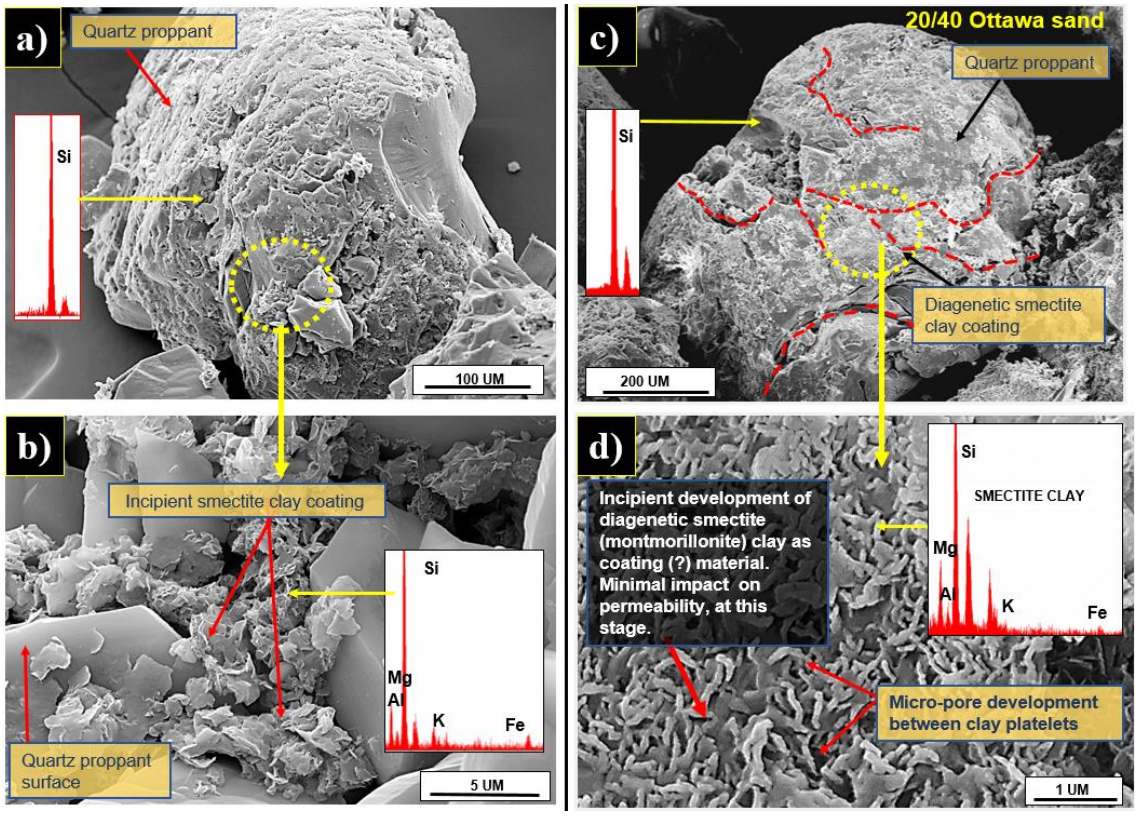

Fig. 43: SEM image of 20/40 Ottawa proppant (concentration: 1.5 lb/ft^2) tested under alkaline environment (pH:10) between Eagle Ford platens at 5000 psi closure stress and 250°F. a) Clay coating is observed on surface. b) EDX confirms the smectite incipient growth along the surface of the proppant. c) Extensive mechanical damage of the proppant grains can be observed (note the red-dashed lines marking the fractures). This fracture exposes the fresh silica surfaces to the fluid system. d) Growth of diagenetic smectite is observed along with associated pore development between clay platelets across the proppant surface.

Furthermore, at the surface of one of the proppant grains, zeolite-like crystal growths were observed (see **Fig. 44a**). At higher magnification, EDX was used to confirm the tubular diagenetic zeolite-like crystals (**Fig. 44b** and **c**). This growth is at an incipient stage during the relatively short-term test. However, over the life of the well, such growth

could intensify and plug-up the propped fractures, demanding an earlier need of re-stimulation, hence adding to the well costs.

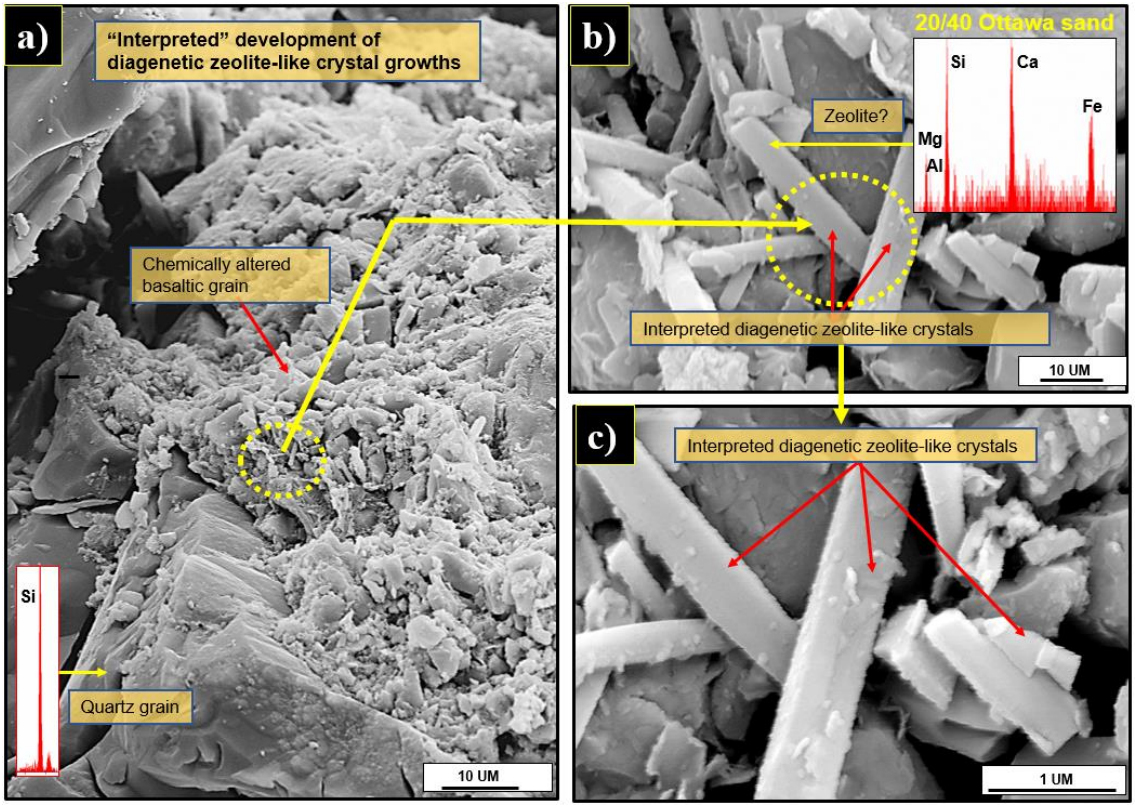

Fig. 44: SEM image of 20/40 Ottawa proppant (concentration: 1.5 lb/ft^2) tested under alkaline environment (pH:10) between Eagle Ford platens at 5000 psi closure stress and 250°F. a) Proppant surface with altered surface. b) and c) At higher magnification, tubular structures are observed. EDX confirms diagenetic zeolite-like crystals at the surface. This growth is at an incipient stage in this relatively short-term test.

Another experiment was conducted between similar Vaca Muerta shale (rock properties discussed in **Fig. 22**) and 20/40 Ottawa sand (concentration: 2 lb/ft^2) system at similar conditions of 250ºF and 5000 psi. The alkalinity was raised to pH 10. Also, basalt (crushed and sieved to 20/40 mesh size, < 5 wt %) was added, to incorporate the presence of complex ions in the rock-proppant-brine system. The proppant-pack was observed under the SEM. As illustrated in **Fig. 45**, physical damage in the form of extensive fracturing of proppant grains can be observed. Also, although at an incipient stage, development of diagenetic smectite covering the proppant grains can be observed.

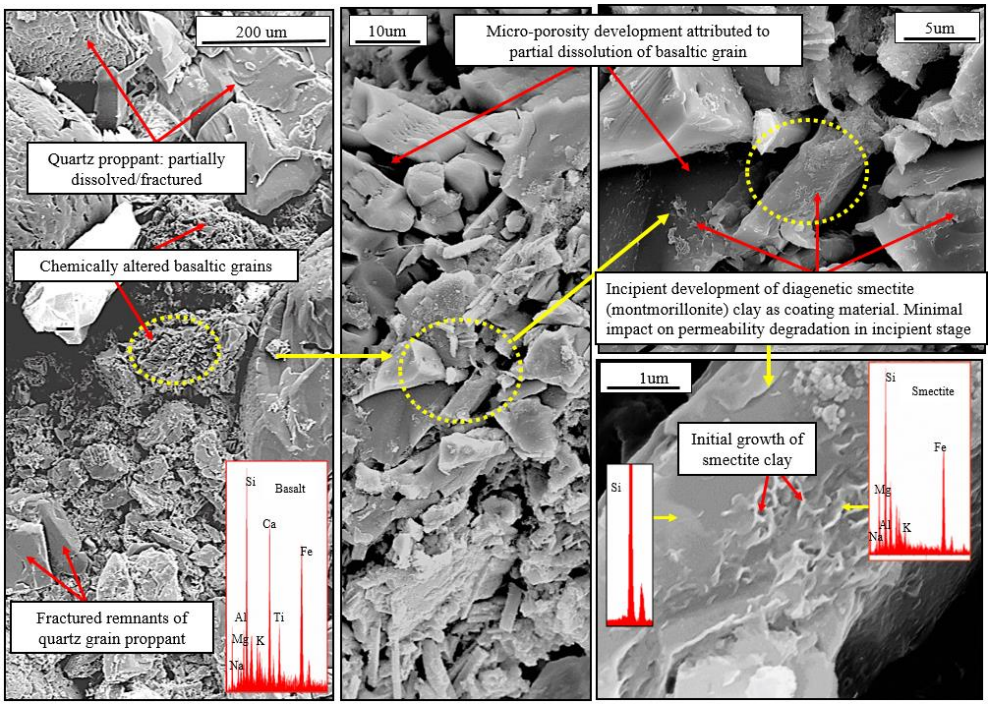

Fig. 45: Secondary electron image of Vaca Muerta shale – 20/40 Ottawa sand system. An axial load (5000 psi), is applied to the proppant-pack (concentration: 2 lb/ft^2) with basalt (crushed and sieved to 20/40 mesh). Brine, prepared using deionized water mixed with 3% NaCl and 0.5% KCl (by weight), was flowed at 3 ml/min. The environment was made basic (pH: 10) by mixing 0.05 m sodium carbonate. The temperature was maintained at 250ºF. Extensive proppant crushing can be observed (left). Within a relatively short time span of approximately 10 days, growth of smectite clay at an incipient stage on the surface of the proppant grain can be observed.

Fig. 46 presents a similar minor development of diagenetic smectite in this experiment of relatively short time span of 10 days. Over longer periods of time, and under certain rock mineralogy environments, this intra-granular micro-pore development, and growth of microporous smectite clay can be accelerated. It can possibly lead to further weakening of proppant grains and further reduction of proppant-pack permeability. Ghosh et al. (2014) observed similar secondary growth of smectite for continuous flow-through testing (spanning 7-30 days; 225°F) for proppant-pack consisting of Barnett shale and 20/40 Ottawa sand.

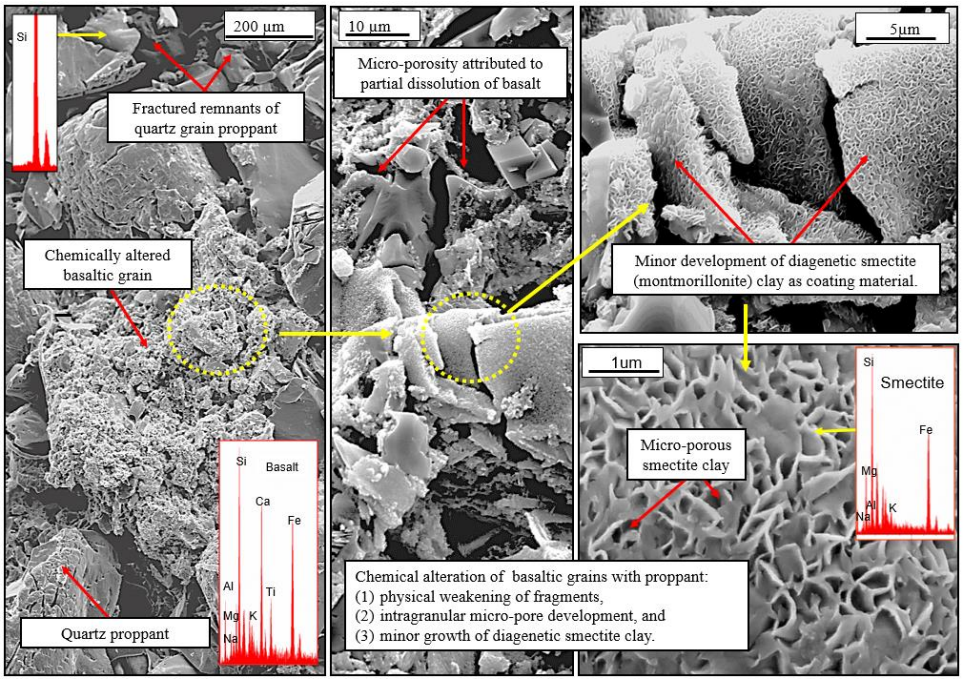

Fig. 46: Secondary electron image of Vaca Muerta shale – 20/40 sand (with basalt) and pH: 10 brine. Proppant concentration: 2 lb/ft^2. Development of diagenetic smectite clay and intra-granular microporosity was observed on proppant grain. Over a longer duration, and in certain chemical conditions, such growth could be accelerated, leading to further weakening of proppant grains and further reduction of permeability.

3.8. Effect of Proppant Size in Alkaline/High pH Environment

This study was done to compare the performance of 20/40 and 60/100 Ottawa sand under a high alkalinity (pH:10) environment. The proppants were tested under similar concentration of 1.5 lb/ft^2, 5000 psi closure stress and 250°F. Brine was prepared similarly with distilled water, 3% NaCl and 0.5% KCl (by weight), and 0.05 m Na_2CO_3 to raise the pH to 10. Similar Eagle Ford platens as mentioned earlier were used (**Fig. 22**).

The comparison of permeabilities for the two proppant sizes is shown in **Fig. 47**. The permeability for both sizes drops precipitously within the first two days (see **Fig. 47-top**). However, the reduction in permeability is much steeper for 60/100 Ottawa sand, and exhibits a dramatic drop within the first few hours of testing. It may seem like the permeabilities have stabilized at the end of days, but the decline in permeability is continuous even through 12 days of testing (**Fig. 47-bottom**). Note that the permeability in bottom graph is shown on a logarithmic scale to accommodate the large range of permeability variation, as well as capture the difference between the brine-permeabilities of the two proppant sizes. Even though the decline in permeability is continuous, the 20/40 sand brine-permeability remains greater than the brine-permeability of 60/100 sand by a factor of 2 through the 12 days of testing. Overall, the permeability of both the proppant sizes drops by more than three orders of magnitude (from approximately 180 darcy to less than 100 md), within a short span of 12 days. Considering the life of the well, such large declines in permeability can have huge ramifications on the performance of stimulation operations.

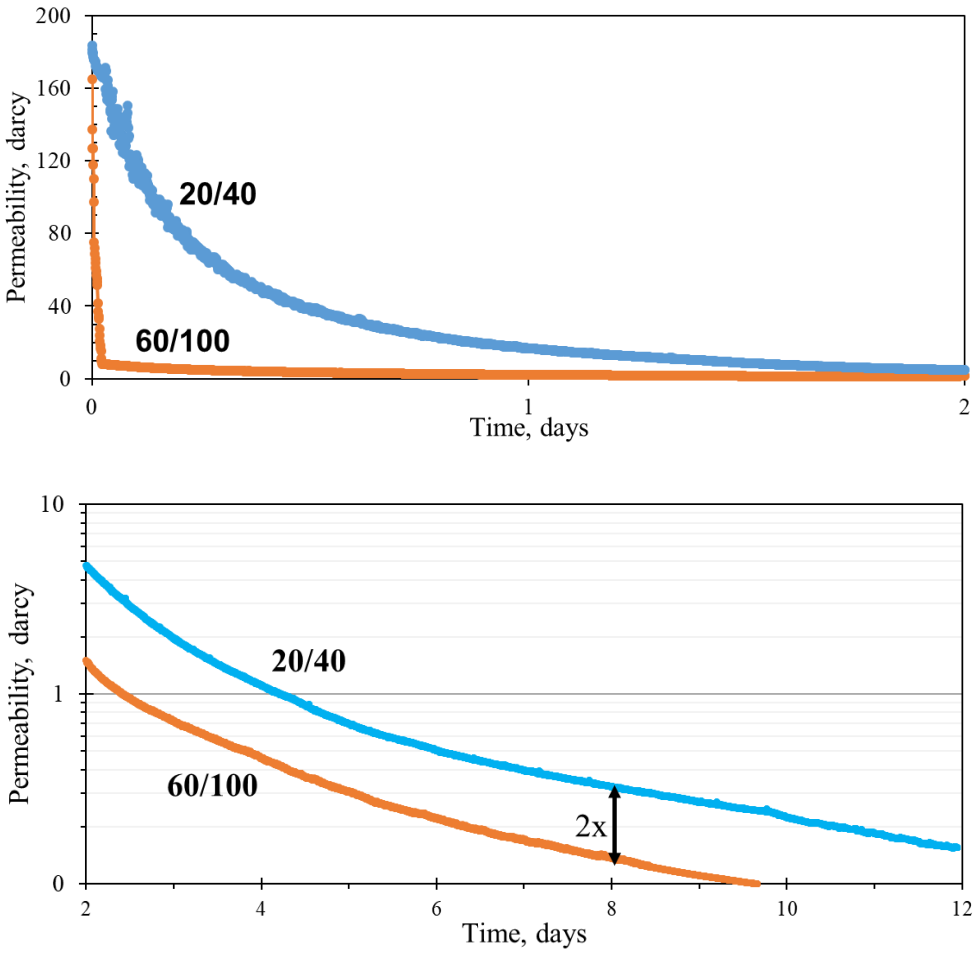

Fig. 47: Permeability variation over time for 20/40 and 60/100 Ottawa sand (concentration: 1.5 lb/ft^2). The permeability for 60/100 sand drops at a steeper rate than 20/40 sand over the first two days (top). However, the permeability for both the sizes continue to degrade over the next 10 days, with 20/40 permeability greater than 60/100 permeability by a factor of 2. Overall, the permeabilities drop by more than three orders of magnitude within a short span of 12 days of testing at 5000 psi closure stress between Eagle Ford platens and 250°F brine (pH:10).

The LVDTs were used to compute the compaction throughout the duration of the experiment. **Fig. 48** shows a step-wise extent of fracture closure that is a coupled product of proppant rearrangement, crushing, fines migration, and embedment over the duration of the experiment. The sequence of the experimental procedure involving changes in pressure, temperature, and flow conditions over different stages of the experiment have

been presented in **Fig. 48a**. The graph shows changes in compaction (normalized to initial thickness), for these different time steps as the proppant-pack is loaded, heated, and flow is started for the testing duration (**Fig. 48b**). The proppant-pack is initially at zero axial load (or closure stress) and at room temperature (step 1). Compaction measurement is started after an initial contact has been established. Transitioning from step 1 to step 2, an axial load of 5000 psi is applied at 100 psi/min and temperature is raised to 250^0F. The cell is left at standby for 12 hours for temperature to stabilize. Note that there is no brine flow at this stage.

Fig. 48 (bottom) illustrates the changes in compaction at different stages of the experiment for metal-20/40 sand, Eagle Ford rock- 20/40 and 60/100 sand combinations. Transitioning from step 1 to step 2, the compaction of metal proppant-pack is representative of compaction only due to rearrangement and crushing of proppant grains. The proppant-pack thickness for Eagle Ford shale reduced by 35%, for both 20/40 and 60/100 sands (step 1 → step 2). This compaction resulted from the application of an axial load of 5000 psi and heat, and has mixed components of crushing and embedment over a period of 12 hours.

Transitioning from step 2 to step 3 (**Fig. 48-bottom**), the brine is flowed at 3 ml/min continuously. After 8 days, metal proppant-pack underwent 35% compaction. For Eagle Ford platens, proppant-packs comprising each proppant size experienced thickness reduction of 65%. Any deviation from metal is most likely due to the embedment component. The fracture width closure (or proppant-pack thickness reduction) is

continuous over time. This difference in total compaction of 30% between metal and Eagle Ford platens can be attributed to the difference in clay content. No significant difference in compaction for proppant-packs consisting of 20/40 and 60/100 sands was observed.

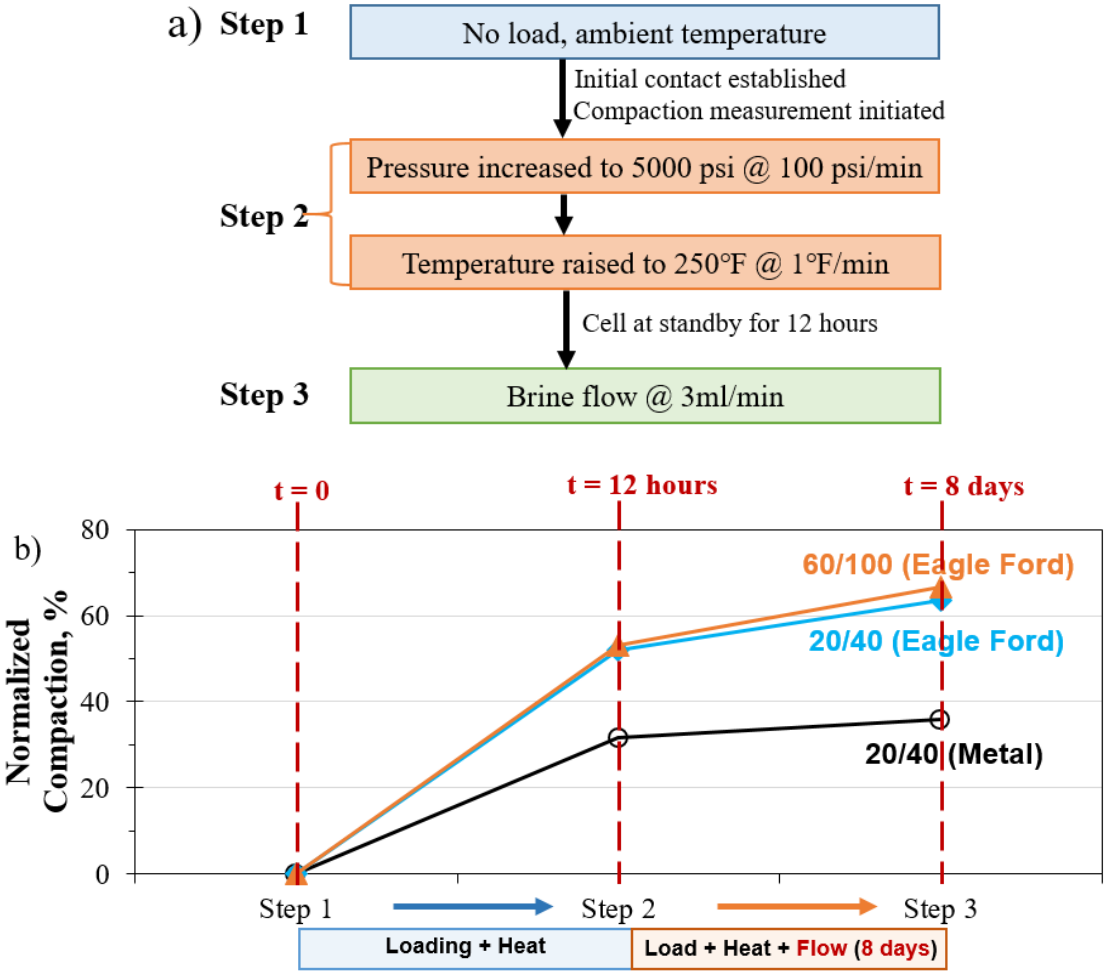

Fig. 48: Compaction measured through LVDTs for the metal (black-circle), 60/100 sand-Eagle Ford platen (orange-triangle) and 20/40 sand-Eagle Ford platen (blue-diamond) tests at a proppant concentration of 1.5 lb/ft^2.Table (top) describes the stress, temperature and flow conditions at different times during the experiment. The graph (bottom) shows the normalized compaction (%) in proppant-pack thickness at different steps. Any deviation from metal test is due to embedment component. At the end of 8 days, 30% additional compaction is observed in Eagle Ford platens as compared to metal. This is primarily due to different clay content.

Both the proppant-packs were scanned under the SEM to gather information about the damage mechanisms. **Fig. 49 (a-c)** shows the grain of initial 20/40 Ottawa sand with slightly abraded surface. **Fig. 49 (d-f)** show the scan for a similar grain after the experiment. Corrosion of the quartz surface can be seen possibly due to the action of continuous flow alkaline brine at 250°F for an extended period of time. Also, EDX shows that precipitation of Na-K crystals from the brine can be observed (see **Fig. 49f**).

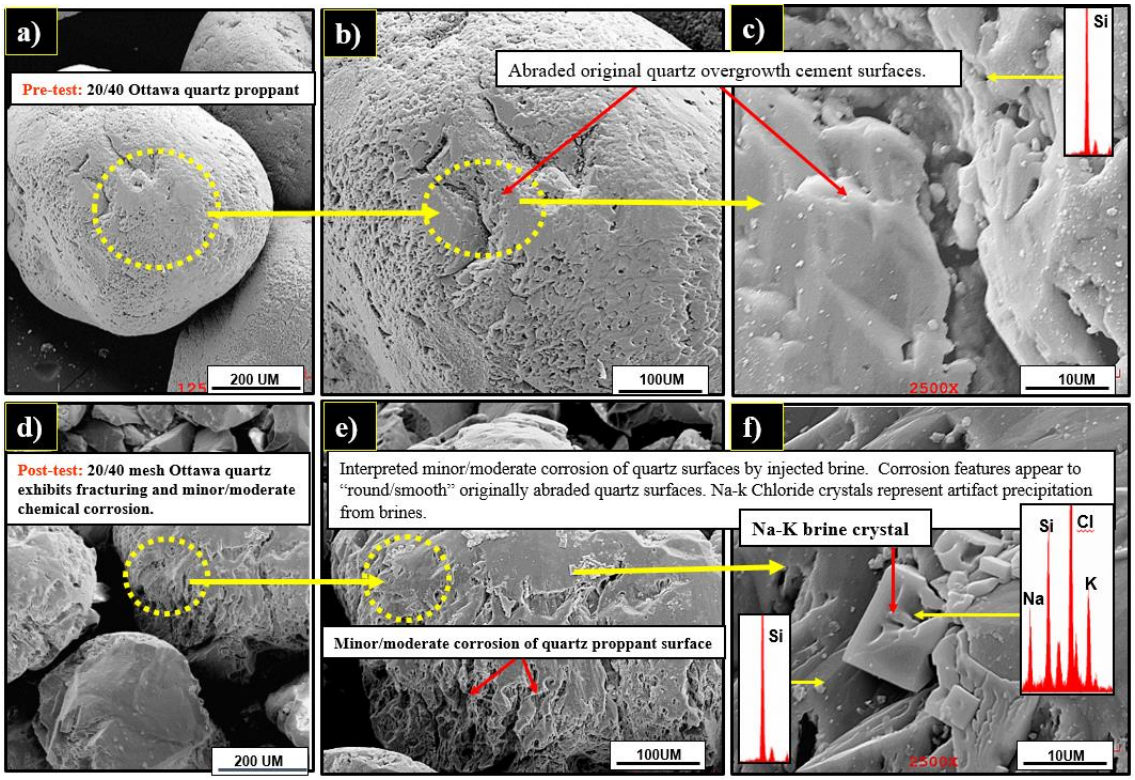

Fig. 49: SEM image of initial 20/40 Ottawa sand (a-c). The abraded quartz surface of the proppant can be observed. Images (d-f) show the surface of 20/40 sand after testing in alkaline environment at 250°F and 5000 psi for extended period of time. The testing was conducted at a proppant concentration of 1.5 lb/ft^2. Moderate corrosion of proppant surface due to the action of fluid can be observed (see image e). EDX confirms precipitation of Na-K crystals possibly from brine.

Broadly, **Fig. 50** shows extensive mechanical damage. The action of closure stress has led to stress intensification at points of contact between proppant-proppant grains, as well as proppant-rock boundary. This has translated into crushing of proppant and generation of fines. The generated fines have a wide range of sizes from approximately 10-200 µm (see **Fig. 50a**). These remnant quartz particles can possibly disseminate and block the pore space, adding to the resistance for fluid to flow. The closure stress has led to development of stress-induced fracture along the proppant grains (**Fig. 50b** and **c**).

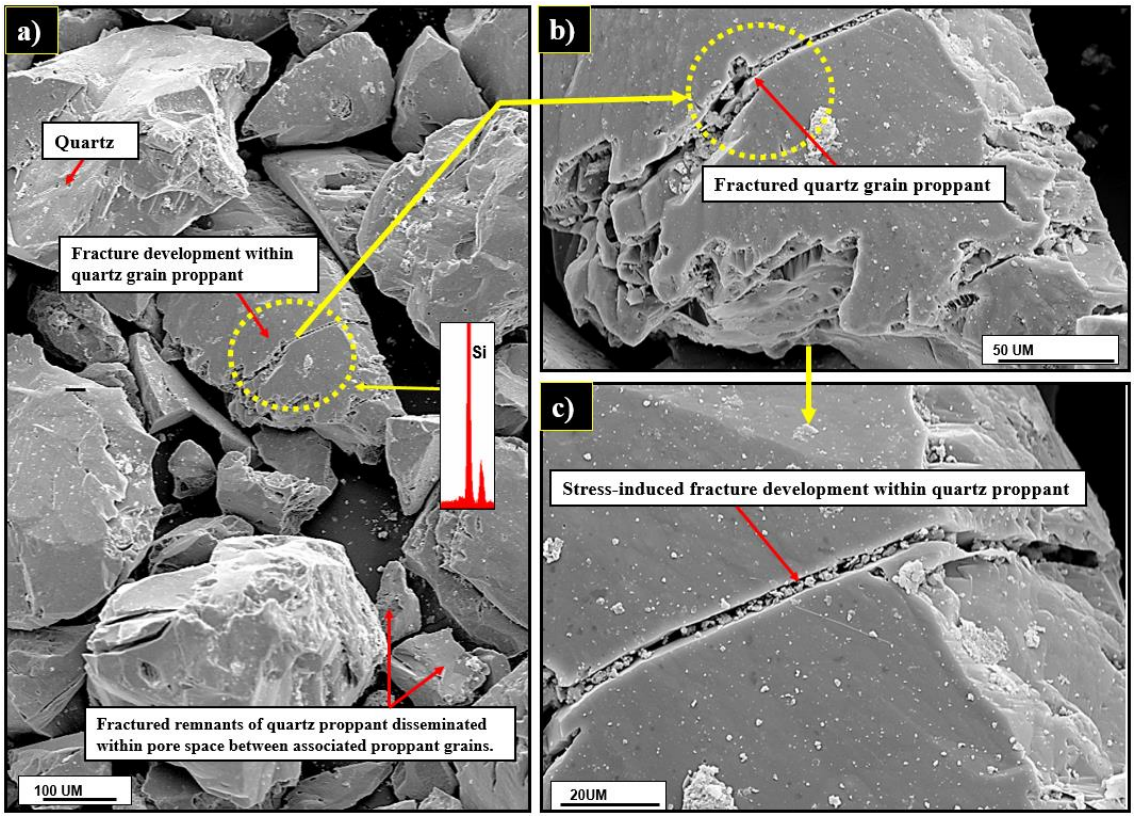

Fig. 50: SEM image of the 20/40 Ottawa sand (concentration: 1.5 lb/ft^2) after testing for extended period of time. a) Mechanical crushing leading to generation of fines capable of blocking pore space can be observed. b) The closure stress has resulted in generation of fracture across the grain of the proppant.

The impact of proppant on the rock platens led to embedment into the surface of rock (**Fig. 51**). Once the embedded proppant is carefully extracted from the rock, the 'pock-marked' surface of the shale is visible (see **Fig. 51a**-center). Note that the boundary of the embedded zone is uplifted due to plunging of proppant into rock surface. The embedment of proppant leads to closure of the fracture, adding to the restriction of fluid flow. The extent of fracture closure due to embedment is critical, and is expected to be a function of rock mineralogy, proppant strength, size, and in-situ pressure and temperature conditions. The image also shows extensive mechanical damage that the proppants have undergone. The disintegrated grains have shattered into fines across the proppant-pack.

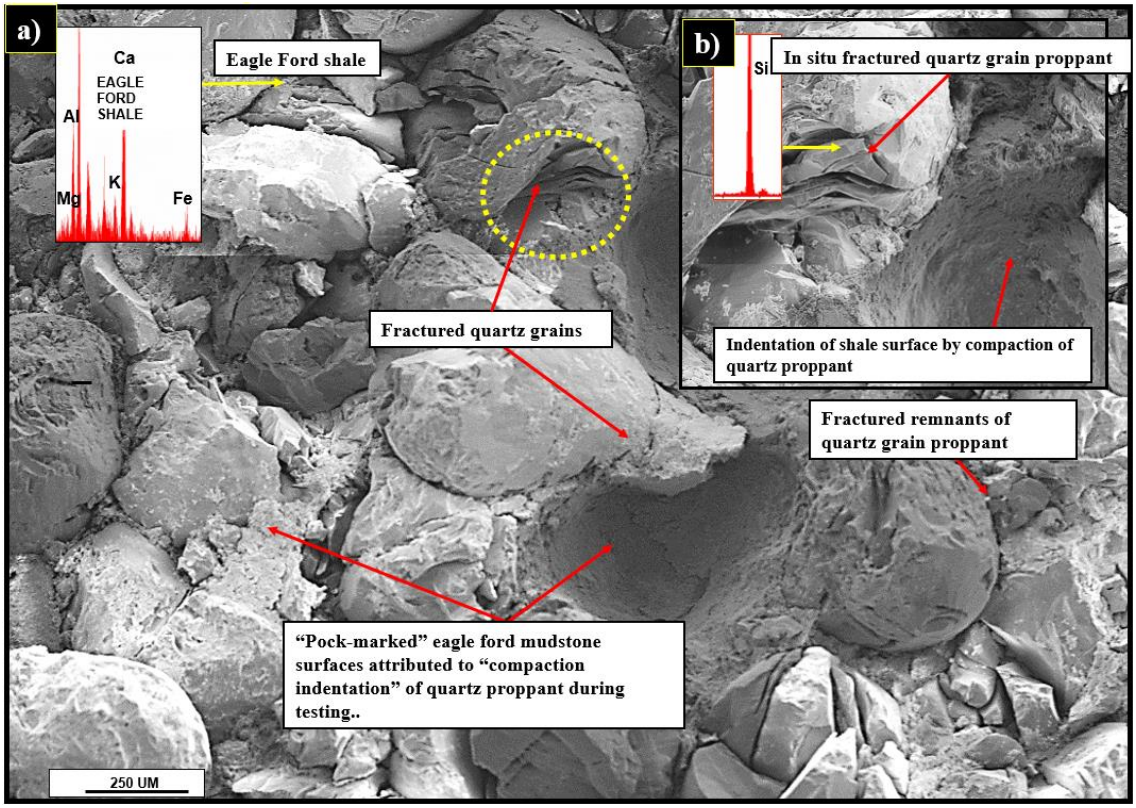

Fig. 51: SEM image of 20/40 Ottawa sand (concentration: 1.5 lb/ft^2) embedment in the Eagle Ford shale after long-term testing. The boundary of the embedded zone is uplifted due to the embedment action. Proppant grains have undergone extensive mechanical impact leading to dislodged fines across the proppant-pack.

Similar SEM imaging was done on the proppant-pack consisting of 60/100 Ottawa sand. **Fig. 52** shows a comparison of proppant grains before (**Fig. 52 a-c**) and after (**Fig. 52 d-f)** the long-term testing conditions. For the native 60/100 sand, abraded surface of the rock can be seen. However, as a result of the testing conditions, minute-sized fines can be observed (see **Fig. 52d**). Also, corrosion of proppant surface due to the action of fluid environment at high temperature and pressure can be observed (**Fig. 52e** and **f**). This action has smoothed the abraded surface of the native 60/100 proppant.

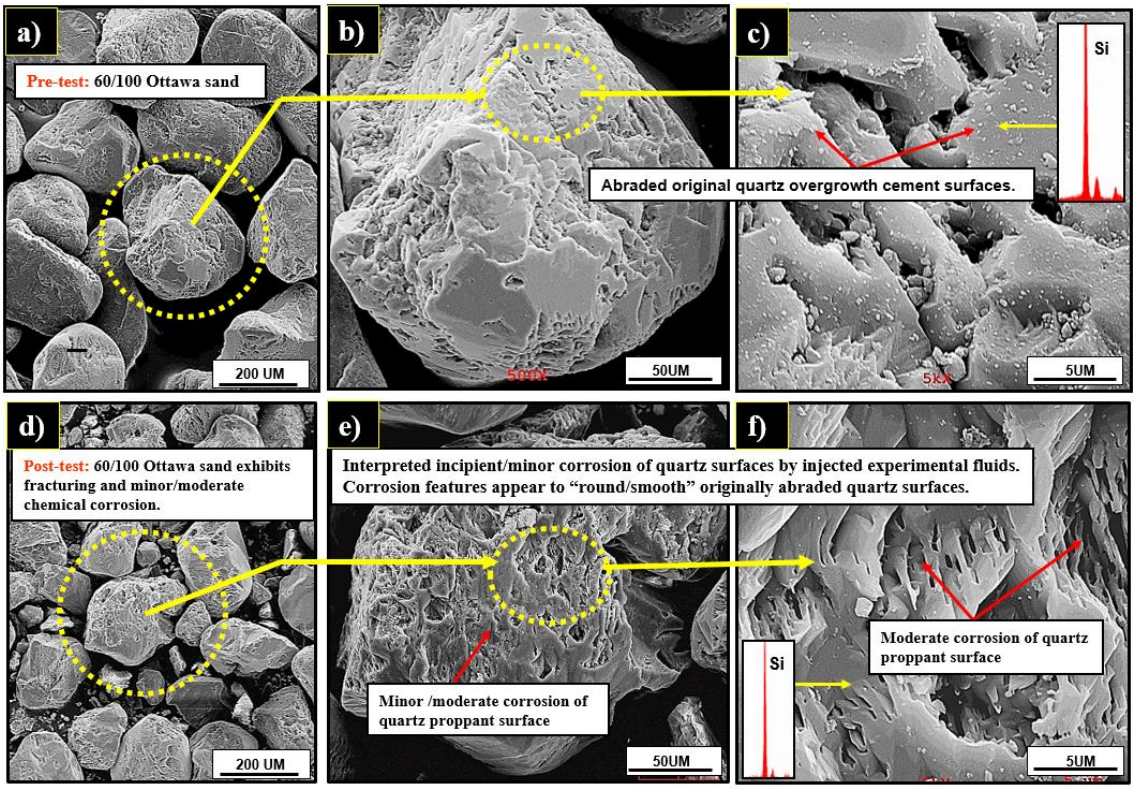

Fig. 52: SEM image of native 60/100 Ottawa sand (a-c). The abraded quartz surface of the proppant can be observed. Images (d-f) show the surface of 60/100 sand (concentration: 1.5 lb/ft^2) after testing in alkaline environment at 250°F and 5000 psi for extended period of time. d) Fines generated by crushing of proppant can be observed. e and f) Moderate corrosion of proppant surface due to the action of fluid can be observed.

The proppant bed was also imaged with a SEM. **Fig. 53** shows an image of the proppant bed of 60/100 sand on Eagle Ford platen after testing in high temperature and pressure conditions over extended duration. Note that the grains of proppant have undergone extensive disintegration (**Fig. 53a**). Mechanical and chemical alterations have led most proppant grains to shatter into fines of different shapes and sizes. **Fig. 53b** shows fractured remnants of the proppant at a higher magnification.

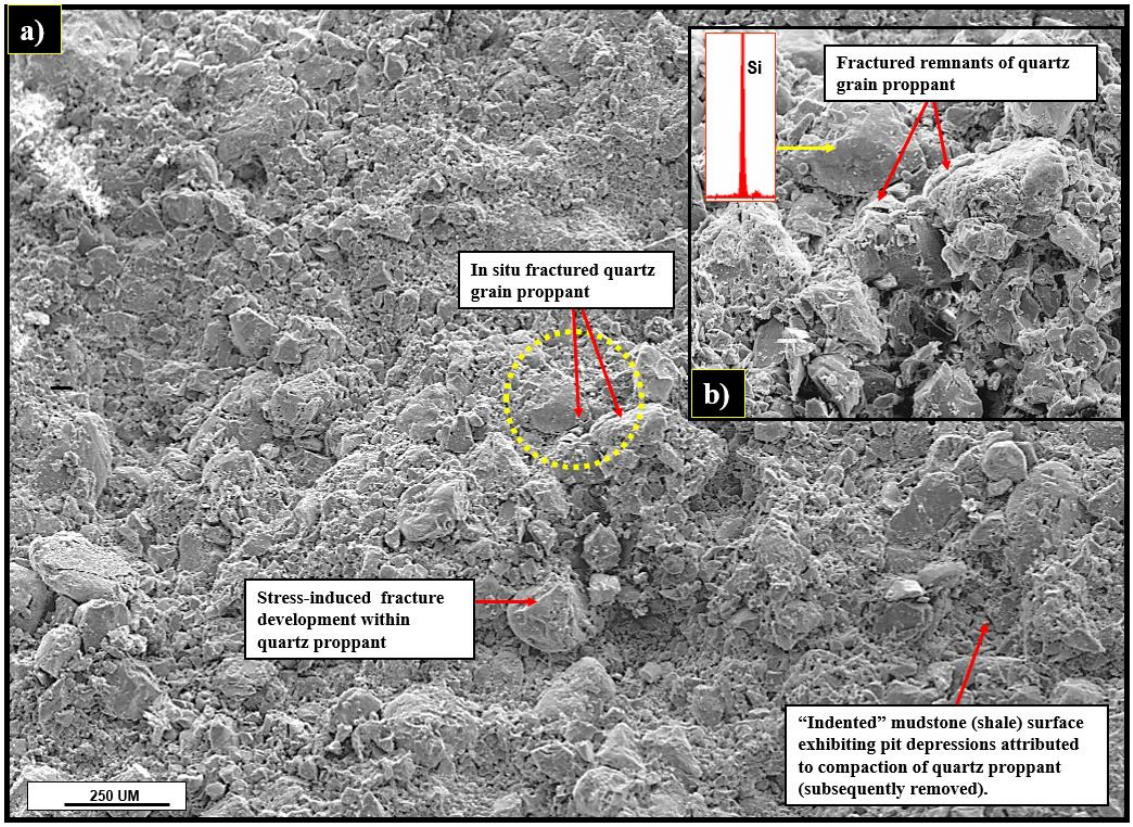

Fig. 53: SEM image of the 60/100 Ottawa sand (concentration: 1.5 lb/ft^2) after testing for an extended period of time. a) A major proportion of proppant grains seem to have undergone extensive shattering and disintegration. b) Mechanical damage resulting into fractured remnants of the 60/100 sand at a higher magnification.

The 60/100 Ottawa proppant grains were gently scrapped from the surface of the Eagle Ford platen. **Fig. 54a** shows the embedment on shale surface. The mechanical damage to the proppant can be observed. **Fig. 54b** shows the embedment on the shale surface at a higher magnification. The extent of embedment was quantified by scanning the rock surface using a laser profilometer. A study by Kassis and Sondergeld (2010) showed similar deformation of Barnett shale when tested with Ottawa sand. They observed microfracturing of the host rock associated with failure of Ottawa sand at 6000 psi closure stress.

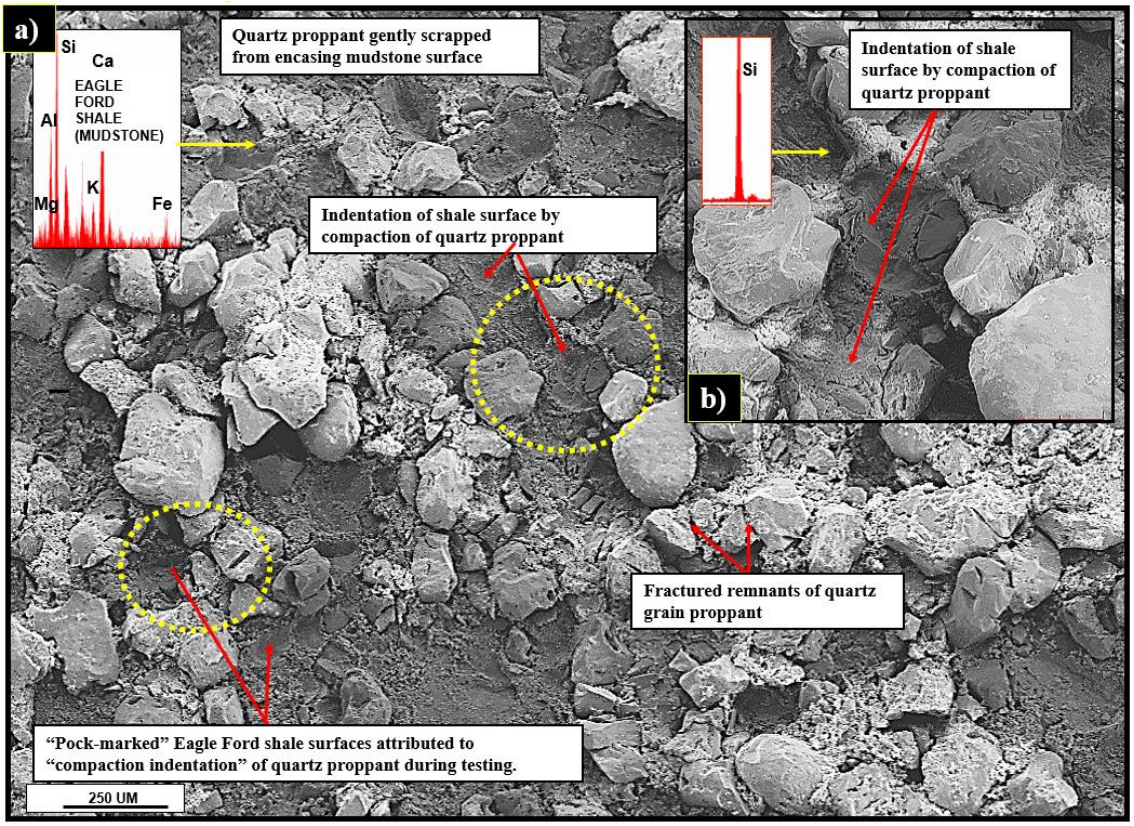

Fig. 54: SEM image of the proppant-pack consisting of 60/100 Ottawa sand (concentration: 1.5 lb/ft^2) and Eagle Ford platens. Mechanical damage of crushed proppant and resulting embedment on the shale surface can be observed. b) An enlarged view of the proppant embedment.

The proppants, before and after experiment, were compared to understand the extent of crushing, and their possible effect on the steep permeability decline within a relatively short period of time. **Fig. 55 (top)** compares the optical image of 20/40 sand before and after the experiment. **Fig. 55 (bottom)** compares the 60/100 sand before and after the experiment. In the post-experiment images (**Fig. 55-right**), apart from severe crushing of proppant, fines from formation can also be observed. Note the dark colored formation fines generated as a result of impact of proppant with the Eagle Ford platens. It was not feasible to separate the formation fines due to their minute size.

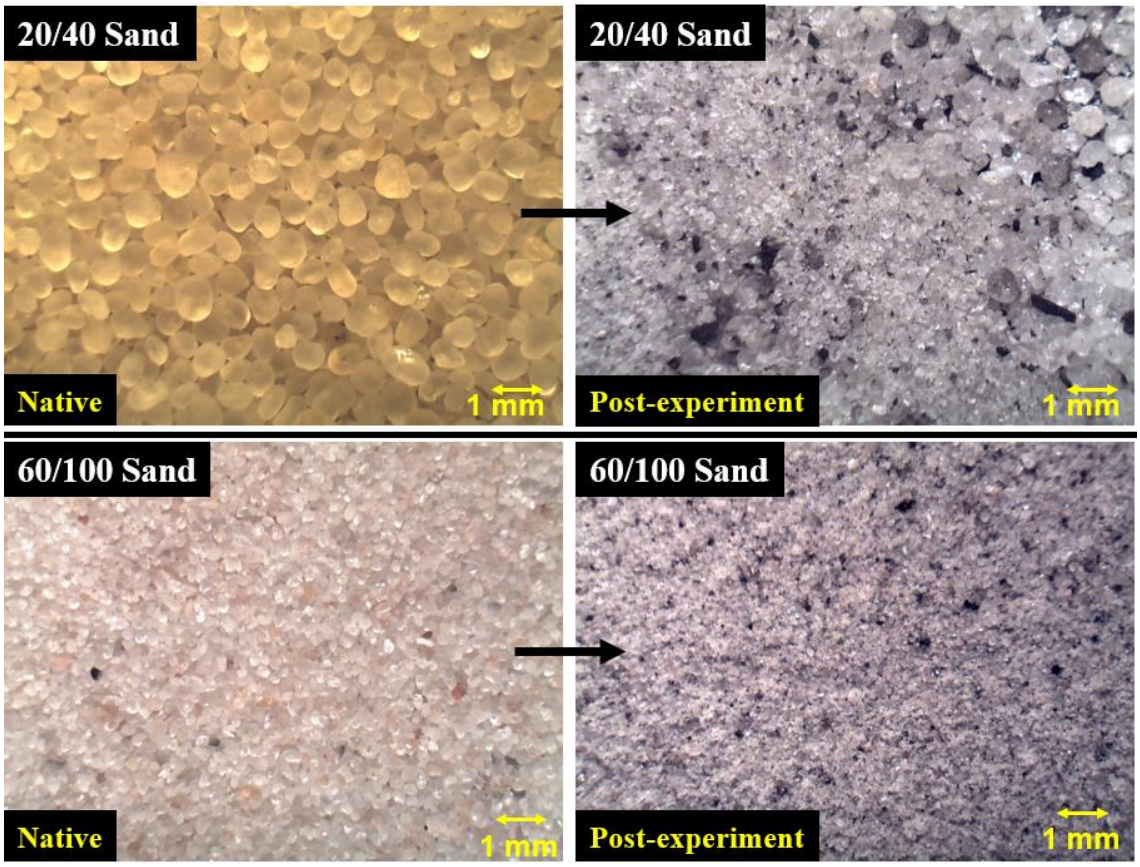

Fig. 55: Optical images of fines generated from proppant crushing. Images of 20/40 sand before and after experiments are compared on top. The images at bottom compare the 60/100 sand before and after the experiment. The tests were conducted at a proppant concentration of 1.5 lb/ft^2. Note the fines generated from proppant crushing as well as the formation (dark-colored particles). The formation fines could not be separated for analysis due to their minute size.

Particle size analysis was used to quantify proppant crushing for both sizes of proppant and examine impact on permeability reduction. **Fig. 56a** shows the distributions for native 20/40 (blue-pattern) and 60/100 (orange-solid) mesh sands. In accordance with API standards, both the samples in native state had less than 5% particles outside of the respective mesh sizes. Note that the 60/100 mesh boundary has been marked in native proppant distribution (see dashed line in **Fig. 56a**).

Post-experiment, **Fig. 56b** shows the distribution for both proppants (below 100 mesh) due to crushing. Significant crushing can be observed in both 20/40 and 60/100 sands. The testing was conducted at similar proppant concentration of 1.5 lb/ft^2 for both the proppant sizes. However, 18% particles of 20/40 sand (by volume) fall below 100 mesh in comparison to 56% particles for 60/100 mesh sand. 60/100 sand experienced a higher percentage of finer particles than 20/40 Ottawa sand by a factor of 3.

The particle size analysis helps answer why the brine-permeability through 60/100 proppant-pack between Eagle Ford platens was considerably lower than 20/40 proppant-pack. The finer 60/100 sand is expected to have smaller pores compared to the coarser 20/40 sand. The coupled effect of presence of smaller pore space and presence of three times additional finer particles in 60/100 sand is expected to plug the permeability in 60/100 mesh sand more rapidly leading to a quick and dramatic drop in permeability (as discussed in **Fig. 47**).

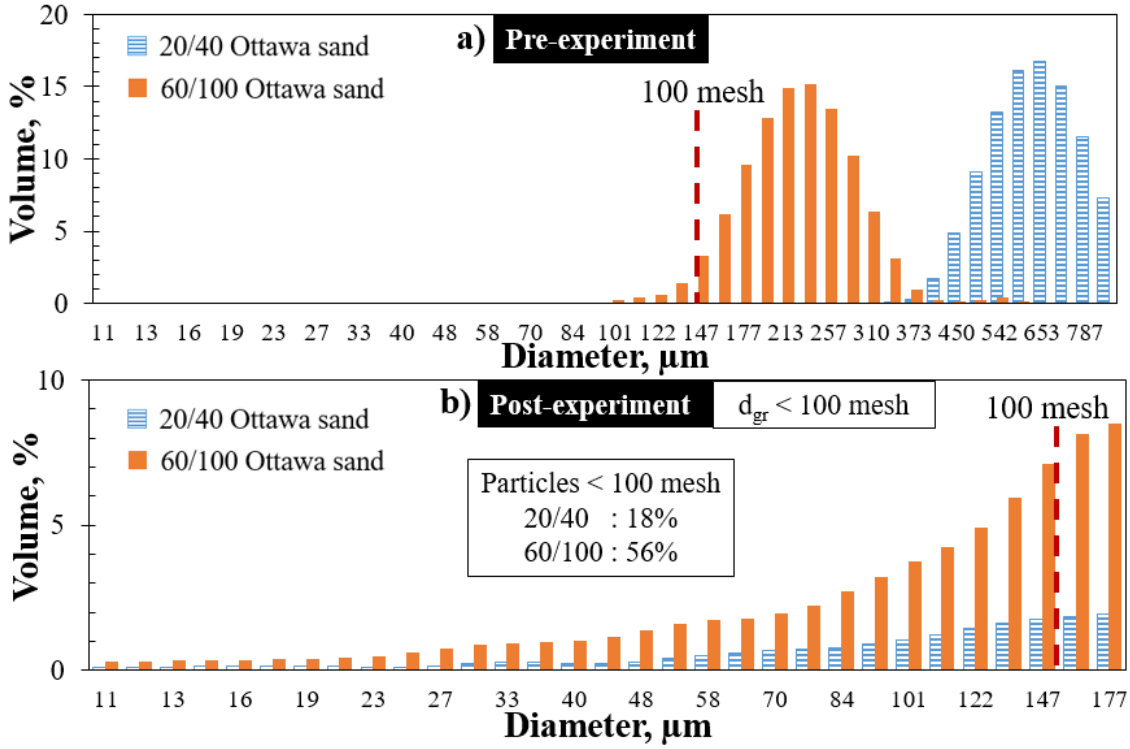

Fig. 56: Laser particle size analysis for 20/40 and 60/100 mesh sand (concentration: 1.5 lb/ft^2) performed a) before and b) after the experiment. The test was conducted between Eagle Ford platens in alkaline (pH:10) environment at 250°F and 5000 psi closure stress. Significant crushing is observed in both 20/40 and 60/100 mesh sands. As compared to 20/40 sand, three times additional grains of 60/100 mesh sand (by volume) fall below 100 mesh.

The surface of the rock was examined to quantify proppant embedment. Prior to starting the experiment, the rock platen was polished to 1200 grit paper. The flat and polished surface of Eagle Ford had a measured RMS roughness of 2 µm. The surface of shale was again scanned under profilometer after flow-through conditions at 250^{0}F and 5000 psi stress. The brine was flowed through proppant-packs consisting of 20/40 and 60/100 Ottawa sands (concentration: 1.5 lb/ft^2).

The embedment on Eagle Ford surface from 20/40 sand is shown in **Fig. 57, left** and that of 60/100 sand is shown in **Fig. 57, right**. With reference to the polished surface (green),

the cooler colors (or negative scale) depict the embedment of proppant, and red colors (or positive scale) represent the height due to either residual proppant or extruded rock around the embedded zone.

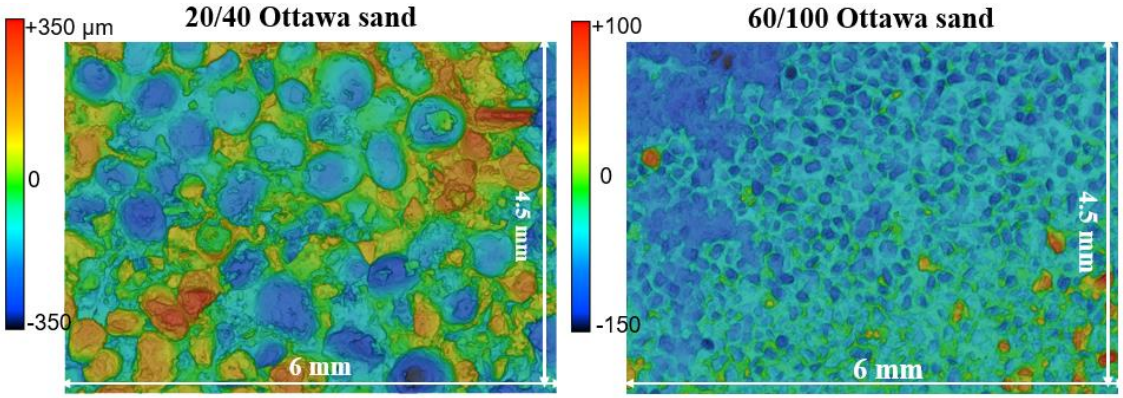

Surface Roughness (RMS), µm	Pre-experiment	Post-experiment	Proportion of grain size (%)
Eagle Ford - 20/40 sand	2	96	40-85
Eagle Ford - 60/100 sand	2	16	60-100

Fig. 57: Laser profilometer scan of Eagle Ford shale platen with 20/40 sand (left) and 60/100 sand (right) after long-term testing. The platen was initially polished using 1200 grit. For Eagle Ford shale platen, an approximate embedment of around 350 µm for 20/40 sand, and 150 µm for 60/100 sand can be observed. The embedment is from Ottawa sand (concentration: 1.5 lb/ft^2), at 5000 psi axial load and 250ºF, when alkaline brine (pH: 10) was flowed.

Comparing the profilometer scans, embedment as deep as approximately 150 µm were observed for 60/100 sand (**Fig. 57, right**). However, for 20/40 sand, embedments as deep as 350 µm were measured (**Fig. 57, left**). Laser profilometer is a direct measure of proppant embedment, and the observed difference seems primarily due to the respective proppant size. For both 20/40 and 60/100 Ottawa sands, embedment of an entire grain diameter (approximately) was observed. Also, the roughness for 20/40 sand changed to 96 µm for 20/40 sand, and 16 µm for 60/100 sand. Higher roughness is due to the deeper embedment.

3.9. Discussion of Results

a) **Standardization of testing protocols:** The conventional procedure involved testing proppant between steel platens with 15 minutes of stress application at ambient temperature (API RP 61). Many improvements to these protocols have been suggested (ISO 13503-5, API 19D), but field observations show that permeabilities measured vary greatly due to pitfalls in the current standards (Penny, 1987; Duenckel et al., 2016). This study suggests and demonstrates that improvements (i.e. testing proppant between shale platens using brine at representative in-situ temperature and pressure conditions over extended testing times, capturing the contribution of different mechanisms) help capture the changes in proppant-pack brine-permeability in a systematic manner. These corroborate the large production declines observed in most shale wells (Baihly et al., 2010). This apparatus allows variation of proppant type, thickness, temperature, closure stress, and composition of pore fluid over long testing times.

b) **Impact of testing-time:** In this study, tests were conducted for extended times (spanning 10-60 days). This study allows the study of effects of mechanical and chemical degradation on fracture conductivity. We have successfully separated the effects of crushing, fines migration, and embedment. The composition of the rock-proppant-brine system and the permeability loss mechanism govern the recommended duration of testing time. Most of the damages associated with mechanical impact like fines generation (due to proppant crushing and formation fines), rearrangement, fines migration, and embedment seem to happen in the short testing times of 7-10 days.

c) **Use of fine mesh sand:** The use of finer mesh sand has increased primarily due to its lower cost. In addition, Thompson (1977) has suggested that placing smaller-sized 60/100 mesh proppant helps reduce leak-off and prevents the loss of expensive chemicals into the formation during the initial stage of the treatment. However, this study demonstrates a considerable difference in brine permeability of different sized proppants (**Fig. 17**). The observed difference in permeability is in accordance with field observations. The operators using primarily fine mesh sand in the Eagle Ford formation had a higher one-month initial production; however, the cumulative production from larger sized proppants had a better performance in the long run (**Fig. 58**) (Al-Tailji et al., 2016). The difference in initial cumulative production between coarse and fine proppant suggests that initial production with the fine mesh proppant is 30% better than with coarser proppant. However, extrapolating the data indicates that the breakeven point occurs after about 8 months, followed by considerable better performance of coarse proppant over the next 16 months.

Field studies and laboratory results suggest use of fine mesh sand leads to lower cumulative production over the life of well. Lower fracture permeability of fine mesh sand can further lead to early remediation, adding to overall cost. With a breakeven time of 8 months, there is reason to re-evaluate completion strategies involving use of greater proportions of finer mesh sand.

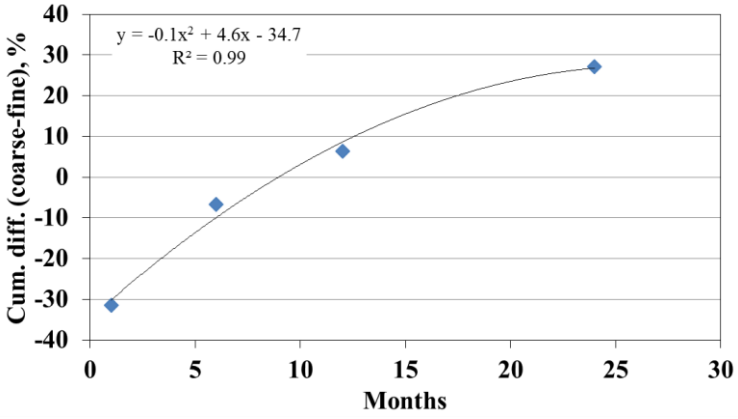

Fig. 58: Cumulative difference in production for coarse mesh completions and other wells employing finer mesh completions for seven Eagle Ford operators producing from 2012 to 2014 (modified from Al-Tailji et al., 2016). A breakeven is achieved after 8 months; with ~30% better performance over 24 months with 20/40 sand.

d) Impact of proppant-pack chemistry on embedment: The measured fracture conductivity is a composite response of the proppant-rock-fluid system. The ability to accurately measure compaction demonstrates a continuous decrease in fracture width over time. The prolonged exposure to fluid at elevated temperature over a long period has a detrimental effect on rock. This work shows that based on the properties of rock, proppant, and brine, the fractures closed by as much as 90% over a duration of 18 days. Also, embedment of approximately an entire grain diameter were observed for 20/40 and 60/100 Ottawa sands, when tested between Eagle Ford platens at a concentration of 1.5 lb/ft^2.

A study by Akrad et al. (2011) showed that exposing Eagle Ford samples to brine reduced Young's modulus by as much as 50% over time. Interestingly, at elevated temperature, the Young's modulus is reduced by as much as 70% in a short time (Akrad et al., 2011). Wick (2015) used nanoindentation technique to measure a late-

time creep exponent of approximately 2 for clay rich Marcellus and Bakken samples. For a hypothetical model assuming cubic relationship between permeability and fracture width, this late-time creep exponent translated into 12% reduction in permeability due to embedment effect (Wick, 2015). Creep can have ramifications in the form of increased proppant embedment over time, reduction of fracture width, and ultimately lower propped fracture permeability. These observations have a strong dependence on rock mineralogy. Deeper embedments are expected in rocks with greater clay content (Terracina et al., 2010; Alramahi and Sundberg, 2012; Zhang et al., 2014; and Ghanizadeh et al., 2016).

e) **Impact of fluid chemistry/diagenesis:** Crosslink fracturing techniques require the use of alkaline/high pH environments to trigger the action of crosslinkers. The results in this study show that the permeability for pH:10 experiments is lower than pH:7 experiments by a factor of 10, even after only 8 days of testing. Imitating sub-surface environment by introduction of basalt (surrogate for volcanic ash, commonly found in shale plays like Eagle Ford and Vaca Muerta), growth of diagenetic smectite and zeolite like crystals were observed. Mineral growths have also been observed in static tests by Weaver et al. (2007), LaFollette and Carman (2010), and Duenckel et al. (2011). In this study, such growths could be observed in dynamic conditions with the aid of electron microscopy. However, it should be noted that the diagenetic growth is driven by the chemical potential difference in the proppant-pack system, and is expected to be observed in the relatively long-term experiments. Note that over a duration of 10-day experiment, approximately 12 gallons of brine flowed through the

proppant-pack. According to Kondash et al. (2017), 10,000-90,000 bbl of fluid is recovered in a typical flowback operation from the well. Observation of diagenetic growth after exposure to a small fraction of actual operation could mean that the diagenetic growth could be affecting performance at a larger scale over the life of well.

f) **Permeability estimation from particle size:** Attempts have been made to estimate the permeability of pore systems based on characteristics of spherical particles. Panda and Lake (1994) extended the Carman-Kozeny model to include statistics of the particle size distribution for permeability prediction. Also, Mirani et al. (2017) modified the Berg model (1970), which uses grain size and sorting to predict permeability in confined stress conditions. However, using the parameters for 20/40 sand that underwent 12 days of testing between Eagle Ford platens, the predicted permeability is more than 4 orders of magnitude higher than the permeability measured though continuous flow-through experiments. The differences are possibly because the model underestimates the parameters needed to accommodate proppant-thickness, proppant shape and sorting, etc. The Berg model (1970) uses proppant-pack porosity based on grain diameter. However, proppant crushing has led to tremendous change in sorting and porosity of the proppant-pack. Also, the over-estimation of predicted permeability through the model is higher for the finer 60/100 mesh sand, probably due to lower than expected porosity of proppant-pack due to crushing of Ottawa sand.

g) Impact of fracture conductivity:

Fracture modeling and simulation are important to understand the impact of implementing different stimulation techniques, proppant types and sizes, etc. According to a simulation study by Mayerhofer et al. (2006), increasing SRV by a factor of 2 almost doubles production. However, the increase in SRV by a factor of 3 does not result into a proportional rise in cumulative gas production. They attributed this behavior to the low fracture conductivities creating large pressure drops within the network, adding complexity to the efforts to drain extended portion of the fracture network. For large fractures in Barnett shale, low fracture conductivity becomes a first-order problem that can lead to substantial loss in production of hydrocarbons in the early life of well (**Fig. 59**). The results show that a 20-fold lower fracture conductivity can lead to 4-fold lower production over 1000 days (Mayerhofer et al., 2006).

The current study demonstrates a large decrease in fracture conductivity measured through experiments at simulated reservoir conditions in a relatively short span of 10-60 days. Over the life of well, the effect on production could be dramatic. Also, this study demonstrates that fractures close by as much as 90% due to mechanisms like rearrangement of grains, proppant crushing, and embedment, greatly affecting performance of propped-fracture network. However, most simulation studies do not take this into account, leading to very optimistic expectations.

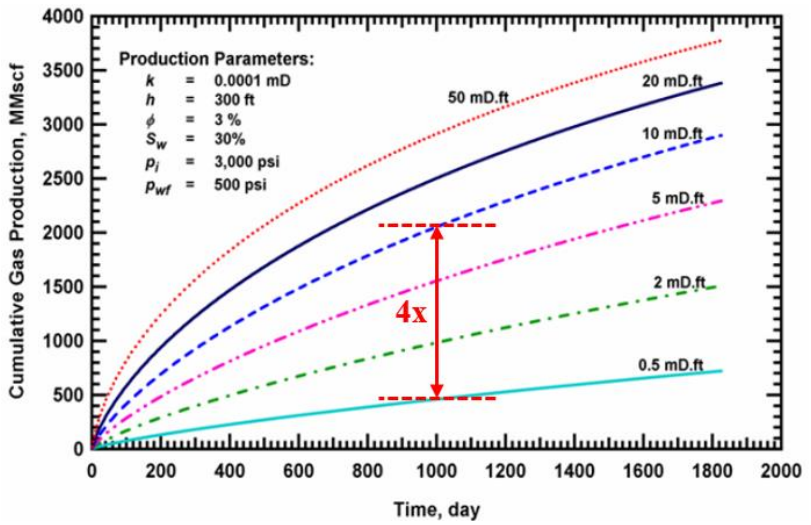

Fig. 59: Cumulative gas production affected by fracture conductivity. Over 1000 days of production, a 20-fold difference in fracture conductivity can lead to 4-fold difference in production (Mayerhofer et al., 2006).

h) Implications: Conventional proppant conductivity test involves testing for short times between sandstone or metal platens; which leads to overestimation of the proppant-pack permeability. **Fig. 60** shows comparison of dimensionless fracture conductivity (F_{CD}) from conventional lab tests versus the long-term tests conducted in this study. F_{CD} (discussed in section 1.6) was calculated using proppant conductivity of 1804 md-ft. for 5000 psi closure stress (20/40 Ottawa sand), and extrapolated on time scale **(dotted lines, Fig. 60)**. This was done to demonstrate that according to API tests, the conductivity is assumed to be remain constant.

The different markers show different fracture half-lengths assumed for comparison. The matrix permeability was adopted from measurements conducted on shale core samples (Mathur et al., 2016).

In contrast, the changing fracture conductivity for 20/40 Ottawa sand measured between Eagle Ford platens was used to calculate F_{CD} **(dashed lines, Fig. 60)**. These long-term measurements capture the dramatic drop of F_{CD} below the optimal F_{CD} **(blue band, Fig. 60)** within a relatively short span of 10 days. Over the life of well, the proppant performance could be drastically reduced and will require restimulation.

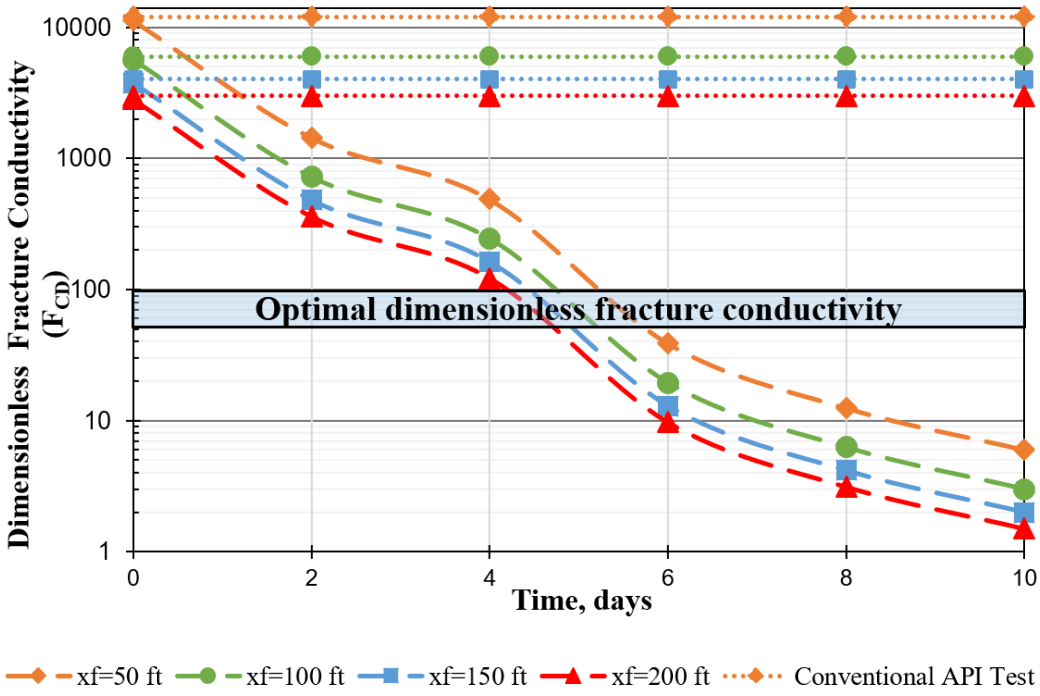

Fig. 60: Comparison of dimensionless fracture conductivity computed from conventional API test (dotted lines) versus continuous flow-through test for 20/40 Ottawa sand between Eagle Ford platens (dashed lines). The API test is a short duration test, and the numbers were extrapolated to demonstrate that the proppant conductivity is assumed to be constant as a function of time. The different markers are representative of fracture half-lengths used for comparison. The current study shows that proppant conductivity measurements at in-situ conditions between shale platens capture the drastic drop in F_{CD} below the optimal F_{CD} (blue band) within a short span of 10 days.

This study deals with tests representing multiple layers of proppant that keep the fracture propped open. It should be noted that in the reservoir, monolayer of proppants

can be achieved, where individual grains can experience substantially higher effective stress. This can translate into higher crushing and embedment, especially at lower proppant concentrations. Also, factors like non-darcy flow, irreparable damage due to mudcake build-up, and uncertainties in mapping of proppant placement can drastically affect proppant performance.

Chapter 4: Conclusion and Recommendations

Conclusions:

Most of the standard proppant test practices (ISO 13503-5, API RP 19D) fail to simulate proppant performance under field conditions and measure optimistic values of permeability due to several shortcomings, i.e. testing between sandstone platens for short durations at ambient conditions, and not taking the changing fracture width into account. In many unconventional plays, clay content dominates the mineralogy and therefore adds a component of proppant embedment which is unaccounted for in standard tests. Additionally, embedment can enhance the production of fines which leads to additional permeability reduction. Dynamic measurements in the current study were conducted for extended periods of time (spanning 10-60 days) using brine. Our procedure allows variation of proppant type, thickness, temperature, closure stress, and composition of pore fluid over long testing times while also recording compaction.

Note all conclusions are based on experiments carried out at 5000 psi closure stress, 250ºF at a proppant concentration 1.5 lb/ft^2 and the brine composed of deionized water mixed with 3% NaCl and 0.5% KCl, by weight, except where noted. The main conclusions drawn from this study are:

1. **Proppant size effect:** We observe proppant performance has a direct dependence on proppant size. The smaller the proppant size, poorer the performance over longer times. In tests between metal platens for 12 days, the 20/40 mesh sand suffers a 32% permeability reduction as compared to 56% drop for 40/70 mesh sand. However,

permeability of the 60/100 mesh sand reduced by a staggering 99% in just 4 days. Tests with coarse (20/40 mesh) and fine (60/100 mesh) proppants suggest long term well productivity is significantly decreased with the use of fine proppants.

2. **Fines migration:** In a 12-day test on 20/40 Ottawa sand between metal platens, we observe 14% additional crushed finer particles at the outlet, as compared to inlet. Fines created between metal platens are only due to crushed proppant. SEM images confirm similar observations in test between Vaca Muerta platens, however, when shale platens are used, additional fines from the formation are generated due to proppant embedment.

3. **Embedment:** Experiments with steel and shale platens allow the separation of crushing and embedment components in assessing proppant performance. The compaction between metal plates is entirely from proppant crushing and rearrangement. However, when using shale platens, an additional component of embedment is introduced due to presence of soft components. Embedment (depending on clay content) has been observed to be critical in reducing fracture conductivity. SEM images suggest such differences are the result of extensive proppant crushing, fines generation and significant proppant embedment on rock surface. This can have enormous implications at lower proppant concentrations, which are expected in case of areas far from injection site.

4. **Effect of rock mineralogy:** Observations from Vaca Muerta and Eagle Ford shale experiments are as follows:
    a) Compaction data from LVDTs capture the effect of both proppant crushing and embedment. Proppant-pack thickness was observed to reduce as a function of time (creep). Over 8 days, the pack thickness for Eagle Ford reduced by 61% as compared to 41% for Vaca Muerta shale. Proppant rearrangement and crushing contributed roughly 32% to fracture closure (based on test between metal platens). Fracture closure due to embedment was observed to be 9% for Vaca Muerta, and 29% for Eagle Ford. Note that the embedment effect was observed to be proportional to the clay content for these two rocks tested.
    b) Proppant embedment, measured using a laser profilometer, as expected, showed strong dependence on mineralogy. Embedment in Eagle Ford was 2.5 times the embedment observed in Vaca Muerta shale.
    c) Eagle Ford shale exhibited embedments of 350 μm or 40-85% of grain diameter of 20/40 proppant size, as compared to 140 μm or 15-30% grain diameter of 20/40 proppant size for Vaca Muerta shale.
    d) After 8 days of flow-through testing, Vaca Muerta platens exhibited 5 times greater permeability and 8 times greater conductivity than Eagle Ford platens.
    e) Compaction data from LVDTs, SEM images and profilometer scans support the claim that proppant embedment has immense impact on reduction in permeability over time at 1.5 lb/ft^2 proppant concentration.

5. **Effect of time:** A long term test consisting of Vaca Muerta platen and 20/40 Ottawa sand (concentration: 2 lb/ft^2) was conducted. Over 60 days, permeability dropped from 80 darcy to 35 md. The metal platen permeability stabilized at 5 darcy, but the Vaca Muerta brine-permeability dropped by over three orders of magnitudes. SEM images suggest such differences are the result of extensive proppant crushing, fines generation and significant proppant embedment on the rock surface. However, no diagenetic/secondary mineral growth was observed. It is expected that crushing and rearrangement of proppant grains is prevalent in the initial stage of the experiment, followed by embedment and fines migration at a later stage. Observed breaks in slope are possibly representative of these mechanisms, and need further evaluation.

6. **Impact of fluid chemistry/diagenesis:** Observations from experiments comparing the effect of alkaline (pH:10) and complex fluid chemistry on Eagle Ford shale – 20/40 sand proppant-packs are as follows:
    a) The permeability for both pH:7 and pH:10 dropped precipitously over time. However, the brine-permeability for pH:10 experiment was 10 times lower than pH:7 experiment, after 8 days of testing.
    b) LVDTs showed similar compaction for both brines. The fracture width was observed to reduce continuously as a function of time (creep). Over 18 days, the fracture width reduced by 90%.
    c) Eagle Ford shale exhibited embedments of 350 µm or approximately one grain diameter of 20/40 proppant size.

d) The addition of basalt in the presence of pH: 10 brine at elevated pressure and temperature led to growth of diagenetic minerals (smectite and zeolite like crystals). Over the life of well, such diagenetic mineral growth could possibly exacerbate the deteriorating proppant performance.

7. **Proppant size effect in alkaline environment:** The performance of 20/40 and 60/100 sand were compared in pH:10 environment between Eagle Ford platens.
   a) Smaller proppants (60/100 sand) had a poorer performance as compared to 20/40 sand by a factor of 2, with a steeper decline in permeability within initial few hours.
   b) The permeability for both proppants dropped by more than three orders of magnitude within 12 days of testing.
   c) Based on LVDT data, the fracture closed by 61% over 8 days. Proppant rearrangement and crushing contributed 32%, while the remaining 29% was due to embedment.
   d) 60/100 sand produced 3 times greater amount of finer particles as compared to 20/40 sand. The combination of smaller pore space and presence of additional finer particles led to faster plugging of pore space in 60/100 sand.

Recommendations:

- These results of fracture conductivity loss should be examined for other proppant types used in the industry.
- This study involves testing at a proppant concentration of 1.5 lb/ft^2. However, the performance at higher proppant concentration needs to be evaluated.
- Vary the composition of the fluid to study the additives used in the field, such as friction reducer, cross-linker, etc.
- Production decline curve analysis software should incorporate explicitly the effect of fracture conductivity reduction over time.

References

1. Akrad, O. M., Miskimins, J. L., and Prasad, M. 2011. The Effects of Fracturing Fluids on Shale Rock Mechanical Properties and Proppant Embedment. Presented at the SPE Annual Technical Conference and Exhibition, 30 October-2 November, Denver, Colorado. SPE-146658-MS. http://dx.doi.org/10.2118/146658-MS.

2. Al-Tailji, W.H., Shah, K., and Davidson, B.M. 2016. The Application and Misapplication of 100-Mesh Sand in Multi-Fractured Horizontal Wells in Low-Permeability Reservoirs. Society of Petroleum Engineers. https://dx.doi.org/10.2118/179163-MS

3. Alramahi, B., and Sundberg, M.I. 2012. Proppant Embedment and Conductivity of Hydraulic Fractures In Shales. Presented at the 46th U.S. Rock Mechanics/Geomechanics Symposium, 24-27 June, Chicago, Illinois. ARMA-2012-291.

4. API 19D. 2008. Measuring the Long-Term Conductivity of Proppants. Washington, DC: API

5. API RP 61. 1989. Recommended Practices for Evaluating Short-Term Proppant Pack Conductivity. Washington, DC: API

6. Baihly, J.D., Altman, R.M., Malpani, R., and Luo, F. 2010. Shale Gas Production Decline Trend Comparison over Time and Basins. Presented at the SPE Annual Technical Conference and Exhibition, Florence, Italy, 19-22 September. SPE-135555-MS. https://dx.doi.org/10.2118/135555-MS

7. Ballard, B.D. 2007. Quantitative Mineralogy of Reservoir Rocks Using Fourier Transform Infrared Spectroscopy. Presented at the SPE Annual Technical Conference and Exhibition, 11-14 November, Anaheim, California, 11-14 November. SPE-113023-STU. https://dx.doi.org/10.2118/113023-STU.

8. Bandis, S.C., Lumsden, A.C., and Barton, N.R. 1983. Fundamentals of Rock Joint Deformation. *International Journal of Rock Mechanics and Mining Sciences* **20** (6): 249–268. http://dx.doi.org/10.1016/0148-9062(83)90595-8.

9. Beckman Coulter User Manual. 2011. Instructions for use: LS 13 320 Laser Diffraction Particle Size Analyzer.

10. Bohacs, K.M. 1998. Contrasting Expressions of Depositional Sequences in Mudstones from Marine to Non-marine Environs, in Schieber, J., Zimmerle, W., and Sethi, P., Mudstones and Shales, Characteristics at the Basin Scale: Stuttgart, Schweizerbart'sche Verlagsbuchhandlung, **1**: 32-77.

11. Bohacs, K.M., Grabowski Jr, G.J., Carroll, A.R., Mankiewicz, P.J., Miskell-Gerhardt, K.J., Schwalbach, J.R., Wegner, M.B. and Simo, J.T. 2005. Production, Destruction, and Dilution - The Many Paths to Source-Rock Development. SEPM Special Publication **82**: 61-101.

12. BP Energy Outlook. 2017. Accessed November 2017. https://www.bp.com/content/dam/bp/pdf/energy-economics/energy-outlook-2017/bp-energy-outlook-2017.pdf

13. Brown, T.L., LeMay, H.E., Bursten, B.E., Murphy, C.J., and Woodward, P.M. 2012. Chemistry: The Central Science, twelfth edition. Upper Saddle, N.J: Pearson Prentice Hall.

14. Calvin, C., Diaz, H.G., Mosse, L., Miller, C., and Fisher, K. 2015. Evaluating the Diagenetic Alteration and Structural Integrity of Volcanic Ash Beds within the Eagle Ford Shale. Presented at the SPE/CSUR Unconventional Resources Conference, Calgary, Alberta, 20-22 October. SPE-175961-MS. http://dx.doi.org/10.2118/175961-MS.

15. Calvin, J., Grieser, B., and Bachman, T. 2017. Enhancement of Well Production in the SCOOP Woodford Shale through the Application of Microproppant. Presented at the SPE Hydraulic Fracturing Technology Conference and Exhibition, The Woodlands, Texas, January 24-26. SPE-184863-MS. https://dx.doi.org/10.2118/184863-MS.

16. Chapman, M. 2017. Proppant Selection in Unconventional Reservoirs – Carbo Ceramics. Accessed November 10, 2017. http://www.carboceramics.com/news-and-resources/resources/technical-presentations?page=2.

17. Clark, J.B. 1949. A Hydraulic process for increasing the productivity of wells, Petrol. Trans. AIME., **186**: 1-8.

18. Cooke, C. E. Jr. 1973. Conductivity of fracture Proppants in Multiple Layers. J Pet Technol. 25 (09): 1101-1107. SPE-4117-PA. http://dx.doi.org/10.2118/4117-PA.

19. Cutler, R.A., Enniss, D.O., Jones, A.H., and Swanson, S.R. 1985. Fracture Conductivity Comparison of Ceramic Proppants. Society of Petroleum Engineers. SPE J. 25 (02): 157-170. SPE-11634-PA. http://dx.doi.org/10.2118/11634-PA.

20. Dahl, J., Nguyen, P., Dusterhoft, R., Calvin, J., and Siddiqui, S. 2015. Application of Micro-Proppant to Enhance Well Production in Unconventional Reservoirs: Laboratory and Field Results. Presented at the SPE Western Regional Meeting, Garden Grove, California, April 27-30. SPE-174060-MS. https://dx.doi.org/10.2118/174060-MS.

21. Dang, S.T., Sondergeld, C.H., and Rai, C.S. 2018. Interpretation of NMR Response to Hydrocarbons: Application to Miscible EOR Experiments in Shales. *SPE Res Eval & Eng.* SPE-191144-PA. https://dx.doi.org/10.2118/191144-PA.

22. Duenckel, R.J., Conway, M.W., Eldred, B., and Vincent, M.C. 2011. Proppant Diagenesis - Integrated Analyses Provide New Insights Into Origin, Occurrence, And Implications For Proppant Performance. Presented at the SPE Hydraulic Fracturing Technology Conference, The Woodlands, Texas, 24-26 January. SPE-139875-MS. https://dx.doi.org/10.2118/139875-MS.

23. Duenckel, R., Moore, N., O'Connell, L., Abney, K., Drylie, S., and Chen, F. 2016. The Science of Proppant Conductivity Testing- Lessons Learned and Best Practices. Presented at the SPE Hydraulic Fracturing Technology Conference, 9-11 February, The Woodlands, Texas, USA. SPE-179125-MS. http://dx.doi.org/10.2118/179125-MS.

24. EIA. 2016a. Hydraulically Fractured Wells provide Two-Thirds of U.S. Natural Gas Production. http://www.eia.gov/todayinenergy/detailphp?id=26112

25. EIA. 2016b. Trends in U.S. Oil and Natural Gas Upstream Costs. https://www.eia.gov/analysis/studies/drilling/pdf/upstream.pdf

26. EIA. 2017. Annual Energy Outlook 2017. Accessed November 2017. https://www.eia.gov/outlooks/aeo/

27. EIA. 2018. Annual Energy Outlook 2018. Accessed February 2018. https://www.eia.gov/outlooks/aeo/

28. Epmag. 2014. More Drilling Pushes Demand For Sand Higher. Epmag.com, October 9, 2014. Accessed March 2017. http://www.epmag.com/more-drilling-pushes-demand-sand-higher-756321.

29. Friedman, G. 2003. Classification of Sedimentary Rocks. In G. V. Middleton (Ed.), Encyclopedia of sediments and sedimentary rocks Kluwer Academic encyclopedia of earth sciences series. Dordrecht, The Netherlands, Boston: Kluwer Academic Publishers.

30. Ghanizadeh, A., Clarkson, C.R., Deglint, H., Vahedian, A., Aquino, S., and Wood, J.M. 2016. Unpropped/Propped Fracture Permeability and Proppant Embedment Evaluation: A Rigorous Core-Analysis/Imaging Methodology. Presented at the Unconventional Resources Technology Conference, 1-3 August, San Antonio, Texas, USA. URTEC-2459818-MS. http://dx.doi.org/10.15530/URTEC-2016-2459818.

31. Ghosh, S., Rai, C.S., Sondergeld, C.H., and Larese, R.E. 2014. Experimental Investigation of Proppant Diagenesis. Presented at the SPE/CSUR Unconventional Resources Conference - Canada, Calgary, Alberta, Canada, 30 September - 2 October. SPE-171604-MS. http://dx.doi.org/10.2118/171604-MS.

32. Gidley, J.L., Penny, G.S., and McDaniel, R.R. 1995. Effect of Proppant Failure and Fines Migration on Conductivity of Propped Fractures. *SPE Prod & Fac* **10**(01): 20-25. SPE-24008-PA. http://dx.doi.org/10.2118/24008-PA.

33. Halliburton. 2013. Fracturing Fluid Systems. Accessed January 27, 2018. http://www.halliburton.com/public/pe/contents/Data_Sheets/web/H/H05667.pdf

34. Hawkins, D.B. 1981. Kinetics of Glass Dissolution and Zeolite Formation Under Hydrothermal Conditions. Clays and Clay Minerals 29 (5): 331-340. http://dx.doi.org/10.1346/CCMN.1981.0290503.

35. Haynes. 2016. Hastelloy C-276 Principal Features. http://haynesintl.com/docs/default-source/pdfs/new-alloy-brochures/corrosion-resistant-alloys/c-276.pdf?sfvrsn=6

36. Heald, M.T. 1956. Cementation of Simpson and St. Peter sandstone in parts of Oklahoma, Arkansas, and Missouri. J. Geology **64**: 16-30.

37. Howard, G.C. and Fast, C.R. 1970. Hydraulic Fracturing, SPE Monograph Series, Society of Petroleum Engineers, Richardson, Texas.

38. Jarvie, D. M. 1991. Total Organic Carbon (TOC) Analysis in Treatise of Petroleum Geology: Handbook of Petroleum Geology: Source and Migration Processes and Evaluation Techniques. AAPG Press, Tulsa.

39. Kale, S. 2009. Petrophysical Characterization of Barnett Shale Play. MS thesis, University of Oklahoma, Norman, Oklahoma.

40. Kassis, S.M., and Sondergeld, C.H. 2010. Gas Shale Permeability: Effects of Roughness, Proppant, Fracture Offset, and Confining Pressure. Presented at the SPE International Oil & Gas Conference, Beijing, June 8-10. SPE-131376-MS. https://dx.doi.org/10.2118/131376-MS.

41. Karastathis, A. 2007. Petrophysical Measurements on Tight Gas Shale. MS thesis, University of Oklahoma, Norman, Oklahoma.

42. Keyence User Manual. 2014. Profile-analyzing Laser Microscope VK-X250K/X150K/X120K Series.

43. Knauss, K.G. and Wolery, T. 1988. The Dissolution Kinetics of Quartz as a Function of pH and Time at 70°C. Geochimica et Cosmochimica Acta. 52:43-53. https://dx.doi.org/10.1016/0016-7037(88)90055-5.

44. Kondash, A.J., Albright, E., and Vengosh, A. 2017. Quantity of flowback and produced waters from unconventional oil and gas exploration. Science of the Total Environment **574**: 314-321.

45. Krauskopf, K.P. 1959. The geochemistry of silica in sedimentary environments. Society of Economic Paleontologists and Mineralogists, Silica in Sediments - Special Publication-7:4-19.

46. Krumbein, W.C. and Sloss, L.L. 1963. Stratigraphy and Sedimentation, Second Ed., W. H. Freeman and Company, San Francisco. p. 660.

47. Kumar, V., Sondergeld, C.H., and Rai, C.S. 2012. Nano to Macro Mechanical Characterization of Shale. Presented at the SPE Annual Technical Conference and Exhibition, 8-10 October, San Antonio, Texas, USA. SPE-159804-MS. http://dx.doi.org/10.2118/159804-MS.

48. LaFollette, R.F., and Carman, P.S. 2010. Proppant Diagenesis: Results So Far. Presented at the SPE Unconventional Gas Conference, Pittsburgh, Pennsylvania, 23-25 February. SPE-131782-MS. https://dx.doi.org/10.2118/131782-MS.

49. Lejay, A., Larmier, S., Rutman, P., and Gelin, F. 2017. The Role of Porosity in the Development of Parallel Bedded Calcite Filled Fractures (or Beef) in the Vaca Muerta: An Integrated Analysis From High Resolution Core Data. Presented at the SPE/AAPG/SEG Unconventional Resources Technology Conference, Austin, Texas, 24-26 July. URTEC-2668071-MS. http://dx.doi.org/10.15530/URTEC-2017-2668071.

50. Mathur, A., Sondergeld, C.H., and Rai, C.S. 2016. Comparison of Steady-State and Transient Methods for Measuring Shale Permeability. Presented at the SPE Low Perm Symposium, Denver, Colorado, 5-6 May. SPE-180259-MS. http://dx.doi.org/10.2118/180259-MS.

51. Mayerhofer, M.J., Lolon, E., Warpinski, N.R., Cipolla, C.L., Walser, D.W., and Rightmire, C.M. 2010. What Is Stimulated Reservoir Volume? *SPE Prod & Oper* **25** (01):89-98. SPE-119890-PA. https://dx.doi.org/10.2118/119890-PA.

52. Mayerhofer, M.J., Lolon, E.P., Youngblood, J.E., and Heinze, J.R. 2006. Integration of Microseismic-Fracture-Mapping Results With Numerical Fracture Network Production Modeling in the Barnett Shale. Presented at the SPE Annual Technical Conference and Exhibition, 24-27 September, San Antonio, Texas. SPE-102103-MS. http://dx.doi.org/10.2118/102103-MS

53. McDaniel, B.W. 1986. Conductivity Testing of Proppants at High Temperature and Stress. Presented at the SPE California Regional Meeting, Oakland, California, 1 January. SPE-15067-MS. http://dx.doi.org/10.2118/15067-MS.

54. Mirani, A., Marongiu-Porcu, M., Wang, H., and Enkababian, P. 2017. Production-Pressure-Drawdown Management for Fractured Horizontal Wells in Shale-Gas Formations. SPE Res Eval & Eng. SPE-181365-PA. (in press; posted 8 November 2017). https://dx.doi.org/10.2118/181365-PA

55. Mottl, M.J. and Holland, H.D. 1978. Chemical exchange during hydrothermal alteration of basalt by seawater-I. Experimental results for major and minor components of seawater. Geochimica et Cosmochimica Acta. 42 (8): 1103-1115, ISSN 0016-7037, https://dx.doi.org/10.1016/0016-7037(78)90107-2.

56. PacWest. 2014. Proppant Market Analysis- First Quarter 2014 Release. PacWest Consulting Partners, Houston, Texas. p. 105

57. Palisch, T. 2016. Introduction to Hydraulic Fracturing and Proppant. University of Oklahoma – SPE Tech Talk.

58. Palisch, T., Duenckel, R., Chapman, M.A., Woolfolk, S., and Vincent, M. 2010. How to Use and Misuse Proppant Crush Tests: Exposing the Top 10 Myths. *SPE Prod & Oper* **25** (03): 345-354. SPE-119242-PA. https://dx.doi.org/10.2118/119242-PA.

59. Palisch, T., Vincent, M., and Handren, P.J. 2010. Slickwater Fracturing: Food for Thought. *SPE Prod & Oper* **25** (03):327-344. https://dx.doi.org/10.2118/115766-PA

60. Panda, M.N. and Lake, L. 1994. Estimation of Single-Phase Permeability from Parameters of Particle-Size Distribution. AAPG Bulletin. **78** (7):1028-1039.

61. Penny, G.S. 1987. An Evaluation of the Effects of Environmental Conditions and Fracturing Fluids Upon the Long-Term Conductivity of Proppants. Presented at the SPE Annual Technical Conference and Exhibition, Dallas, Texas, 27-30 September. SPE-16900-MS. http://dx.doi.org/10.2118/16900-MS.

62. Pioneer Investor Presentation-November. 2017. http://investors.pxd.com/phonix.zhtml?c=90959&p=irolpresentations. p. 12-17

63. PLG Consulting. 2014. Frac Sand – New Volume Impact. 2nd Frac Sands Conference, Minneapolis, MN, September 23. https://plgconsulting.com/wp-content/uploads/2014/09/Indu strial-Minerals-Frac-SandConference-Sept-2014.pdf

64. Schubarth, S., and Milton-Tayler, D. 2004. Investigating How Proppant Packs Change Under Stress. Presented at the SPE Annual Technical Conference and Exhibition, Houston, Texas, September 26–29. SPE-90562-MS. https://dx.doi.org/10.2118/90562-MS.

65. Shukla, P., Kumar, V., Curtis, M., Sondergeld, C.H., and Rai, C.S. 2013. Nanoindentation Studies on Shales. Presented at the 47th U.S. Rock Mechanics/Geomechanics Symposium, 23-26 June, San Francisco, California. ARMA-2013-578.

66. Sinha, S., Devegowda, D., and Deka, B. 2016. Multivariate Statistical Analysis for Resource Estimation in Unconventional Plays Application to Eagle Ford Shales. Presented at the SPE Eastern Regional Meeting, Canton, Ohio, 13-15 September. SPE-184050-MS. https://dx.doi.org/10.2118/184050-MS.

67. Sinha, S., Devegowda, D., and Deka, B. 2017. Quantification of Recovery Factors in Downspaced Shale Wells: Application of a Fully Coupled Geomechanical EOS Compositional Simulator. Presented at the SPE/AAPG/SEG Unconventional Resources Technology Conference, Austin, Texas, 24-26 July. SPE-2697500. https://dx.doi.org/10.15530/URTEC-2017-2697500-MS.

68. Sondergeld, C.H., and Rai, C.S. 1993. A New Concept in Quantitative Core Characterization. The Leading Edge. **12** (7): 774-779.

69. Sondergeld, C.H., Newsham, K., Comisky, J., Rice, M., and Rai, C.S. 2010. Petrophysical considerations in evaluating and producing shale gas resources. Presented at the SPE Unconventional Gas Conference, Pittsburgh, Pennsylvania, USA, 23-25 February. SPE 131768-MS. https://dx.doi.org/10.2118/131768-MS

70. Terracina, J.M., Turner, J.M., Collins, D.H., and Spillars, S. 2010. Proppant Selection and Its Effect on the Results of Fracturing Treatments Performed in Shale Formations. Presented at the SPE Annual Technical Conference and Exhibition, 19-22 September, Florence, Italy. SPE-135502-MS. https://dx.doi.org/10.2118/135502-MS

71. Thompson, J.C. 1977. The Theory, Methods of Application and Results of the Use of 100 Mesh Sand in Stimulating Permian Basin Formations. Presented at the SPE Permian Basin Oil and Gas Recovery Conference, Midland, Texas, March 10-11. SPE-6374-MS. https://dx.doi.org/10.2118/6374-MS.

72. Thomson, A. 1959. Pressure solution and porosity: in Ireland, H.A., (ed.), Silica in Sediments, SEPM Special Publication 7: 92-111.

73. Walsh, J.B., 1981. Effect of pore pressure and confining pressure on fracture permeability. International Journal of Rock Mechanics and Mining Sciences **18**: 429-435.

74. Warpinski, N.R., Wolhart, S.L, and Wright, C.A. 2004. Analysis and Prediction of Microseismicity Induced by Hydraulic Fracturing. *SPE J.* **9** (1): 24-33. SPE-87673-PA. https://dx.doi.org/10.2118/87673-PA.

75. Weaver, J.D., and Knox, J.A. 1992. Evaluation of Steam Resistance of Gravel-Packing Materials. SPE Prod Eng 7 (02): 155-159. SPE-20025-PA. https://dx.doi.org/10.2118/20025-PA.

76. Weaver, J.D., Nguyen, P.D., Parker, M.A., and van Batenburg, D.W. 2005. Sustaining Fracture Conductivity. Presented at the SPE European Formation Damage Conference, Sheveningen, The Netherlands, 25-27 May. SPE-94666-MS. https://dx.doi.org/10.2118/94666-MS.

77. Weaver, J.D., Parker, M., van Batenburg, D.W., and Nguyen, P.D. 2007. Fracture-Related Diagenesis May Impact Conductivity. SPE J 12 (03): 272-281. SPE-98236-PA. https://dx.doi.org/10.2118/98236-PA.

78. Weaver, J.D., Rickman, R.D., and Luo, H. 2008. Fracture-Conductivity Loss Due to Geochemical Interactions Between Manmade Proppants and Formations. Presented at the SPE Eastern Regional/AAPG Eastern Section Joint Meeting, Pittsburgh, Pennsylvania, 11-15 October. SPE-118174-MS. https://dx.doi.org/10.2118/118174-MS.

79. Wick, W. 2015. Application of nanoindentation for creep properties and saturation, Master's Thesis, The University of Oklahoma.

80. Yasuhara, H., Elsworth, D., and Polak, A. 2003. A Mechanistic Model for Compaction of Granular Aggregates Moderated by Pressure Solution. Journal of Geophysical Research 108 (B11): 1-13. 2530. http://dx.doi.org/10.1029/2003JB002536.

81. Zhang, J., Ouyang, L., Hill, A.D., and Zhu, D. 2014. Experimental and Numerical Studies of Reduced Fracture Conductivity due to Proppant Embedment in Shale Reservoirs. Presented at the SPE Annual Technical Conference and Exhibition, 27-29 October, Amsterdam, The Netherlands. SPE-170775-MS. http://dx.doi.org/10.2118/170775-MS.

Appendix A: Details of Experimental Setup

Individual details for each of the components are as follows:

1. **Metering pump and controller**: Two ISCO 100DX syringe pumps are connected in parallel, to maintain a continuous supply of brine for an experiment ranging from 10-60 days. Brine flow is regulated using an integral pump controller with a flow accuracy of 0.01 ml/min at a constant flow rate of 3 ml/min. Each pump has a capacity of 103 ml. The controller is used to communicate pressure and volume data with the computer.

2. **Inlet reservoir**: Sealed inlet brine reservoir hosts the brine for the experiment. The brine was prepared using distilled water mixed with 3% NaCl and 0.5% KCl (by weight).

3. All the connections are made using $1/8^{th}$ inch Hastelloy **tubing** to prevent rusting due to flow of saline fluid at elevated temperature. The tubing going to the conductivity cell is wrapped with a heating element, attached to a variac voltage regulator, to elevate the fluid temperature before it enters the conductivity cell. This is done for easier temperature maintenance. The tubing is also wrapped with a glass-wool insulation.

4. **Transfer vessel**: A transfer vessel made of Peek is used to reduce the pulsations from the switching between two pumps while maintaining continuous flow.

5. **Conductivity cell**: The Hastelloy conductivity cell is used for measuring the proppant-pack performance. The cell has silicon covered heating tape attached to a variac voltage transformer, and glass-wool insulation. Temperature is regulated using a thermocouple attached to a heating system. The features of conductivity cell are discussed in detail in section 2.2.

6. **Differential pressure gauge**: A differential pressure gauge is connected across the conductivity cell to measure pressure changes. The gauge is calibrated over a range of 0-25 psi with an accuracy of ±0.01 psi.

7. **Hydraulic Press**: A servo hydraulic press is used to apply axial load, simulating closure stress on the conductivity cell. The press can apply as much as 10,000 psi closure stress on the proppant-pack, providing a dynamic pressure range to simulate sub-surface environments. An ISCO 100DX metering pump and controller are connected to the hydraulic press to accurately maintain axial load. The controller communicates the data to the computer.

8. **Back-pressure gauge**: The brine will flow after it overcomes a 300 psi back-pressure set by the back-pressure regulator. The back pressure keeps the fluid in single phase, and is used to simulate pore pressure in the propped-fracture system.

9. **Outlet brine reservoir**: After flowing through the proppant-pack, the brine is collected in a sealed reservoir. The brine can be retrieved for water chemistry testing.

10. **Computer**: The software allows recording data from hydraulic press, continuous flow pump system, differential pressure gauge, compaction using LVDTs, and temperature in the conductivity cell using a thermocouple. For this study, the data has been recorded at a frequency of 60 seconds**.**

Appendix B: Petrophysical Characterization of Rocks

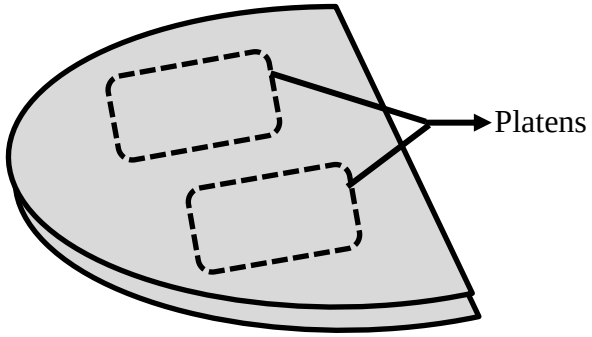

Fig. 61: Schematic of core used to retrieve platens for conductivity testing. The surrounding rock material was used for petrophysical characterization of the platens.

The platens were cut from core. The platens were then polished with a sequence of grits (300, 600, 900, and 1200 grit sizes) for 15 minutes each. This was done to provide a reproducible flat surface before testing, and to emulate planar fractures. The remaining rock adjacent to retrieved platens was used to measure the following properties:

1. **Mineralogy:**

   Mineralogy was estimated using transmission Fourier Transform Infrared Spectroscopy (FTIR) technique (Sondergeld and Rai, 1993; Ballard, 2007). Sixteen commonly found minerals are quantified using this technique. These minerals are quartz, calcite, dolomite, siderite, aragonite, illite, smectite, kaolinite, chlorite, mixed clay, oligoclase feldspar, orthoclase feldspar, albite, pyrite, apatite and anhydrite. The organic matter was removed using a low temperature plasma asher, prior to the determination of mineralogy (Kale, 2009).

2. Porosity

The total porosity is measured with the technique of crushed helium porosity on 10-14 g of rock sample. The bulk volume is measured by applying Archimedes principle to mercury immersion technique. Boyle's Law is applied to determine grain volume, which is used to determine porosity. Katastathis (2007) proposed to shorten the long equilibration times that are required for shales by crushing the samples. Samples are handled with extreme care during the process of crushing so that the weight loss is minimized (<0.1% wt) (Kale, 2009). The grain volume is corrected for the mass of sample lost.

3. TOC

'Total Organic Carbon' or TOC gives the weight percent of organic matter (OM) in a rock sample. TOC is composed of three components: extractable organic matter (EOM), convertible carbon and residual carbon fraction (Jarvie, 1991). The rock is crushed up to 35 mesh (500 μm) particle size experiment, and treated with HCl to remove any inorganic carbonate. The sample is then placed in the Leco Carbon Analyzer, where the carbon in the sample is oxidized to carbon dioxide (by the combustion of organic carbon in a pure stream of oxygen). The gas stream passes through an infrared (IR) detector or thermal conductivity detector (TCD), which determines the amount of CO_2 produced. TOC adds to the soft component of the rock.

4. Young's modulus

The Young's modulus was determined through nanoindentation. This technique involves indenting the rock with a Berkovich indenter while measuring the displacement and force. This is used to calculate the Young's modulus and hardness. The static/indentation Young's modulus has been established to be in good agreement with dynamic modulus on shale samples from various unconventional plays (Kumar et al., 2012). The effect of mineralogy, TOC and porosity on mechanical properties have also been discussed in detail (Shukla et al., 2013). Acquiring core samples is difficult and costly; this technique produces calibrated results in agreement with conventional measurement techniques from readily available drill cuttings.

Appendix C: Profilometer Measurement Procedure and Processing

Procedure: The rock platen (after polishing, as described in **section 2.3.2.1**) is placed on the observation stage, and the sample elevation is adjusted until a focused image of the sample surface is obtained in the laser observation window. The 'fine focus knob' is used to adjust sample elevation to a position between the deepest and highest point. A scan of the surrounding area is acquired. The deepest and the highest point must be within the limit of the lens selected. Under *settings*: 'measurement profile,' 'resolution: super fine (2048*1536),' 'high accuracy,' and 'z-pitch: 0.5' are selected. A 10x10 matrix is then specified for measurement. After the data are acquired, 'adjust' option is used to stitch individual blocks, and the data file is saved in VK4 format (proprietary format of Keyence).

The image is trimmed to a perfect rectangle to ignore the irregular edges due to stitching. The trimmed image is checked for any noise correction, if needed. The surface of the rock might not be exactly horizontal, and needs to be corrected for tilt. The 'tilt correction' is performed in both the X and Y directions. The tilt of the sample can be chosen from different options: plane profile, 3-point, secondary curved surface, sphere, etc., as per requirements. Post tilt corrections, the sample can be viewed in the 3D window to view the elevation profile. Under 'set intensity/height display' option, a histogram of the elevation and density of the data can be obtained. The extremes of the color palette are assigned to the highest and deepest points of interest on the rock surface.